Carbon-chain Free Radicals Studied by Laser and Microwave Spectroscopy

（レーザーおよびマイクロ波分光による炭素鎖フリーラジカルの研究）

Hiroshi Kobayashi

Thesis

Carbon-chain Free Radicals Studied by Laser and Microwave Spectroscopy

by

Hiroshi Kohguchi

Graduate School of Arts and Sciences,
The University of Tokyo
(1996 March)

Contents

Chapter I

General introduction

1. Spectroscopic study on carbon-chain free radicals
2. Vibronic interactions
   - (a) The Renner-Teller effect
   - (b) Vibronic transition
   - (c) Isoenergetic vibronic interaction; Intersystem crossing (ISC) and internal conversion (IC)
3. Zero-field quantum beat induced by intramolecular processes
4. Overview of the present studies

References

1. Spectroscopic study on carbon-chain free radicals

In this thesis, I have treated three types of linear free radicals containing a carbon-chain, HC_4O, CCN, HCCS, as molecular systems. So far, many kinds of the carbon-chain free radicals have been detected in the spectroscopic studies. The following classification is of great help for a systematic understanding of variety of carbon-chain free radicals. Carbon-chain free radicals are characterized or classified by the length of the carbon framework, n, and the terminal atom, X, when denoted as HC_n[1-13], HC_nX[14-25], or C_nX.[26-37] The terminal atom, X, other than a hydrogen varies as X = N[19,20,36,37], O[21-35,31-33], S[14-18,26-30], Si[34,35], *etc.* Even/odd of n helps us in a systematic understanding of the carbon-chain free radicals with the same terminal atom.

One of the most important topics in spectroscopic studies of carbon-chain free radicals is its structural linearity in the electronic ground state. As in the Walsh diagram, a molecular structure is closely related to the molecular orbitals. Linear carbon-chain free radicals in the doublet state can be classified into two groups by the singly occupied molecular orbital (SOMO), which is the molecular orbital of the unpaired electron. Members in the first group have the $\tilde{X}\,^2\Pi$ state, in which the unpaired electron occupies the π–orbital mainly composed of the 2p atomic orbitals of carbons. While carbon-chain free radicals in the second group have the $\tilde{X}\,^2\Sigma$ state, in which the SOMO is the σ–orbital mainly composed of the lone-pair atomic orbital of the terminal atom. A bent structure of a carbon-chain free radical is often explained as a deviation from the hypothetical linear structure. If a linear carbon-chain free radical of the first group is deformed to a bent molecule, the degeneracy of Π is removed. Deformation is caused by the vibronic interaction. Even though the equilibrium configuration is still linear, the nuclear bending motion can couple with the electronic motion around the molecular axis, and as a result the vibronic interaction produces

a complex vibronic structure. This is a general explanation for the linearity of the carbon-chain free radicals with the $\tilde{X}\,^2\Pi$ state from a view point of the molecular orbital.

In the above picture assuming the linear structure to be zero-order approximation, the vibronic interaction is a keyword in understanding of the structure of the carbon-chain free radicals. The vibronic interaction in general is deeply related to the nature of the electronic state itself and energetic relation to other electronic states. The valence atomic orbital of the terminal atom (X) gives us information on the nature of the molecular orbital of HC_nX and C_nX. The length of carbon-chain (n) and even/odd of n enable us to discuss on the energy and symmetry of the SOMO within the Hückel model.

In order to demonstrate systematic understanding based on the classification by X and n, HC_nO and HC_nS are compared as examples. In the case of the linear structure, the members of the both groups have $2n+3$ π-electrons. Assuming that the energy of the σ-orbital which is mainly composed of the lone pair atomic orbitals of X (=O, S) is lower than that of the $2p\pi$-orbital contributed from a heavy atom framework ($-C_nX$), the molecules with even n and odd n have the $\tilde{X}\,^2\Pi_i$ and $\tilde{X}\,^2\Pi_r$ state, respectively. The ground state of the HCCS radical (n =2), which will be described in Chapter V, is actually $\tilde{X}\,^2\Pi_i$ and the spin-orbit interaction constant is reported to be negative.[16] On the other hand, the HCCO radical (n=2), which is isovalent to HCCS, has the bent structure in the ground state, which is the lower counterpart of the $^2\Pi_i$ state perturbed by the vibronic interaction.[21,22] As for the members with larger n, HC_3S and HC_4S have linear structure and their ground states are $\tilde{X}\,^2\Pi_r$ and $\tilde{X}\,^2\Pi_i$, respectively,[18] corresponding to odd and even n. While, the members of the HC_nO group have non-linear structures up to HC_4O,[21-25] which has been studied in the present study and will be described in Chapter III. The different terminal atom X (S or O) characterizes the strength of the vibronic interaction and the molecular

structure of HC_nX. The CCN radical, whose electronic state will be described in Chapter IV, has $\tilde{X}\,^2\Pi_r$.[36] The next longer species, C_3N, was reported to have $\tilde{X}\,^2\Sigma$.[8] It is necessary to consider the energy reverse of the σ-orbital and the 2pπ-orbital as the length of the carbon-chain, *n*. Observation of the electronic transition of the longer members of the C_nN group will enable us to discuss on the relation between the orbital energy and the molecular skeletal length. While, the symmetry of the vibronic ground states of the C_nH group ($C_2H(^2\Sigma)$, $C_3H(^2\Pi)$, $C_4H(^2\Sigma)$, $C_5H(^2\Pi)$, $C_6H(^2\Pi)$) has been discussed from the view point of *n*. This discussion is based on both the molecular orbital and the vibronic interaction for each member of HC_nO group.

Many kinds of the carbon-chain free radicals have been observed by using infrared (IR) and microwave (MW) spectroscopy in the electronic ground state. From the observed high resolution data, the molecular structures have been determined. Compared with the variety of spectroscopic data in the ground state, a systematic study of the electronic structure of carbon-chain radicals have been limited. Even for small carbon-chain free radicals whose electronic transitions were observed, intensive spectroscopic studies have not been as many as those for closed shell molecules. In order to elucidate the vibronic interaction affecting the electronic structure of carbon-chain radicals, a survey of complex vibronic structure in wide energy region by electronic spectroscopy is indispensable.

Theories of the vibronic interaction, especially those of the Renner-Teller effect, have been well established[38-41] and applied to the analyses of the observed spectroscopic data. The theory of the Renner-Teller effect based on the effective Hamiltonian method has been applied successfully to the complex vibronic structures. Influence of the Renner-Teller effect on the spin-orbit interaction constant and the rotational constants in each vibronic states have been also explained very well. On the other hand, methods of *ab initio* MO calculations have been developed,[42] and the vibronic

interaction were treated in an appropriate manner. For triatomic radicals[42,44] and ions[45,46], calculated potential energy surfaces and rovibronic wavefunctions have been used to interpret the observed electronic spectra.

In this thesis, spectroscopic studies have been made for three carbon-chain free radicals, HC_4O, CCN, and HCCS. Main interests are the molecular structures, the vibronic structures, and molecular dynamics in the electronic ground and the excited states. As for the experimental aspects of the thesis, laser and microwave spectroscopy have been applied. Pure rotational spectra containing the hyperfine splitting observed by microwave spectroscopy of HC_4O have given us valuable information on the Renner-Teller effect. The vibronic structures of CCN and HCCS in a wide energy region have been obtained by laser spectroscopy. Dynamics in the electronic excited state has also been observed by laser spectroscopy for HCCS. A pulsed-discharge nozzle (PDN) has been developed and employed throughout the series of the works in this thesis as an efficient device to produce the carbon-chain free radicals. The experimental setup will be shown in Chapter II. In the remaining parts of this Chapter, a simple explanation for the vibronic interactions (2), and a zero-field quantum beat induced by intramolecular processes (3) are described as the background of the theoretical aspects of the thesis. In the last part of this chapter (4), the vibronic interactions observed in the thesis are summarized.

2. Vibronic interactions

(a) The Renner-Teller effect

Many of the linear polyatomic free radicals have a nonzero electronic angular momentum ($\Lambda \neq 0$). A linear molecule with *n* nuclei has *n-2* degenerate bending modes and a nonzero vibrational angular momentum

($\ell \neq 0$) arises in the vibrationally excited states of the bending mode. Under the Born-Oppenheimer approximation, the electronic motion and the bending motion around the molecular axis are completely decoupled and the vibronic wavefunction is represented as a direct product of the vibrational part and the electronic part, $\{ | v^{\ell} > | \Lambda > \}$. Breakdown of the Born-Oppenheimer approximation, or invalidity of the separation of the variables of the two motions, can be included as a vibronic interaction. Since the molecular vibronic wavefunction is well described based on the Born-Oppenheimer approximation, the vibronic interaction can be treated as a perturbation. In degenerate electronic states (Π, Δ, ...), the evidence of the vibronic interaction is observed not as a implicit energy shift from an unperturbed level but as a explicit splitting of the energy level which would be degenerate without vibronic interactions. Therefore, the vibronic interaction is found in these degenerate electronic states more clearly than in a Σ electronic state. Hereafter, a linear polyatomic radical in the degenerate electronic states (Π, Δ,...) is considered.

Adiabatic potential energy surfaces can be depicted based on the Born-Oppenheimer approximation. A degenerate electronic state corresponds to a pair of potential energy surfaces and they are split into two parts by the vibronic interactions. The Renner-Teller effect is a vibronic interaction along the molecular axis in a liner radical, the potential energy surface along the bending coordinates are changed most significantly. The features of the potential energy splitting along the bending coordinate vary with the strength of the vibronic interaction.

If the vibronic interaction is strong enough to shift the equilibrium structure or the potential minimum from the linear structure, it is called as the "static" Renner-Teller effect. In other words, the molecule has a bent structure as a result of the static Renner-Teller effect. If a molecule keeps its planarity, two split electronic states represented as A' and A" symmetries in C_s group behave as independent electronic states. The electronic ground

and the first excited states of NH_2[47], BH_2[48] , and HCO[49] are such examples of the Renner-Teller pairs. In Chapter III of this thesis, non-linear structure of the HC_4O radical will be ascribed to the static Renner-Teller effect. The static Renner-Teller effect change the molecular structure, for which microwave spectroscopy yielded the conclusive determination. From an analysis of the hyperfine structure accompanied with the pure rotational spectra of HC_4O, the ground electronic state of this radical having A" symmetry is a lower member of the Renner-Teller pair correlated with the degenerate Π state at linear structure.

If the vibronic interaction is not so strong as to change an equilibrium geometry, it is called as the "dynamic" Renner-Teller effect. Although the potential energy surface is also split into two parts (W^+ and W^- in this case), the molecular symmetry group ($C_{\infty v}$ or $D_{\infty h}$) remains unchanged by this dynamic Renner-Teller effect. Symmetry of the resultant vibronic states, Γ_{ev}, is simply described by the group theory as a direct product, $\Gamma_{ev} = \Gamma_{ele} \otimes \Gamma_{vib}$, where Γ_{ele}, $\Gamma_{vib} = \Sigma_{(g,u)}, \Pi_{(g,u)}$, etc. For example, the complex vibronic structures observed for $BO_2(\tilde{X}\,^2\Pi)$[50], $CCN(\tilde{X}\,^2\Pi)$[36], $C_3(\tilde{A}\,^1\Pi_u)$[51], and $NCO(\tilde{X}\,^2\Pi)$[52] were ascribed to the dynamic Renner-Teller effect. In Chapter III, the vibronic energy levels of the CCN radical in $\tilde{X}\,^2\Pi$ will be experimentally determined for the first time by using laser spectroscopy. In Chapter V, the vibronic structure of the HCCS radical in $\tilde{A}\,^2\Pi$ will be observed in a wide energy region (~3,000 cm^{-1}). The complex vibronic structure in the $\tilde{A}\,^2\Pi$ state showed an evidence of the dynamic Renner-Teller effect.

In the case of an intermediate strength of the vibronic interaction, where the potential energy surface along the bending coordinate becomes flatter with its equilibrium minimum remaining unchanged at the linear configuration, a relatively low bending frequency would be observed. This is the case of a "quasi linear" molecule. This type of the quasi linear

molecule, that is, the π radical perturbed by the intermediate Renner-Teller effect, has not been reported.

As a σ radical, the HCCN radical in the $^3\Sigma^-$ ground state was referred to a quasi linear molecule. Studies on its linearity and non-rigidity of HCCN have been attempted.[19,20]

The Hamiltonian representing the vibronic interaction is,

$$H = \sum_k \frac{Z_k e^2}{|r_e - \delta R_k|} - \sum_k \frac{Z_k e^2}{|r_e - R_k|}, \qquad (1)$$

where $Z_k e$ is an effective charge of the k-th nucleus, R_k is a position vector of the k-th nucleus, r_e is the position vector of the (unpaired) electron, δR_k is a deviation of the k-th nucleus from its equilibrium position. The Hamiltonian (1) corresponds to the difference between the Coulomb energy at an equilibrium structure and that at the structure deviated by δR_k. Note that the Hamiltonian (1) does not include non-adiabatic terms such as $P_k = \partial/\partial R_k$. The vibronic interaction is originally ascribed to breaking down the Born-Oppenheimer approximation which neglects the non-adiabatic terms of the nuclear motion, $P_k = \partial/\partial R_k$. It would be straightforward to include non-adiabatic terms as perturbations, so called vibronic interactions, in the Born-Oppenheimer description. However it is a conventional treatment to consider δR_k in eq. (1) as a perturbation in a well-defined basis functions representing a molecule in its linear structure. Therefore, the basis function used for the electronic part, $\{|\Lambda>\}$, does not include the nuclear coordinates. The Hamiltonian (1) can be modified into,

$$H = V_1(Q_+\exp(-i\theta) + Q_-\exp(i\theta)) + V_2(Q_+^2\exp(-2i\theta) + Q_-^2\exp(2i\theta)) + (\text{higher orders}), \qquad (2)$$

which is adequate for basis functions $\{|\Lambda>|v^l>\}$ of vibronic states (the Born-Oppenheimer states), in which only one bending mode is considered for simplicity. In eq. (2), V_1 and V_2 are functions of the electronic radial coordinates, $Q_\pm = R\exp(\pm i\phi)$ is the normal polar coordinate of the bending motion of the nucleus, and θ is the electronic polar angle. Vibrational modes other than the bending mode are omitted in eq. (2) for simplicity. The selection rule for the first term in eq. (2) is $\Delta\Lambda = \pm 1$ and $\Delta\ell = \mp 1$ in the basis function of the $\{|\Lambda, n, \ell>\} = \{ R_{|\Lambda|}(r)\exp(i\Lambda\theta)\rho_{n,|\ell|}(R)\exp(i\ell\phi) \}$. The V_1 term in eq.(2) is called as the Herzberg-Teller interaction. The matrix elements for this term are not diagonal within the Π electronic state. Within the first-order perturbation approach, the Herzberg-Teller interaction does not change the vibronic energy of the Π state, but changes the wavefunction, and consequently, selection rules for the electric transition. The second term in eq. (2) provides non-zero matrix elements with $\Delta\Lambda = \pm 2$ and $\Delta\ell = \mp 2$, that is, the diagonal matrix elements within the Π electronic state, which remove the degeneracy. This is the Renner-Teller effect in the Π electronic state. For the Δ electronic state, the higher order term in eq. (2), $Q_\pm^4\exp(\mp 4i\theta)$, whose selection rule is $\Delta\Lambda = \pm 4$ and $\Delta\ell = \mp 4$, gives non-zero diagonal matrix elements and removes the degeneracy. All the terms in the Hamiltonian (1) do not mix the states with different $K = \Lambda + \ell$, that is, $\Delta K = 0$ is the rigorous selection rule for the vibronic interaction represented by eq. (1). It is true that quantum numbers Λ and ℓ are not good quantum numbers, but a quantum number for the vibronic angular momentum, K, is always a good quantum number. The Renner-Teller effect in various kinds of linear triatomic radicals in the Π electronic state have been observed, and the Hamiltonian explained above interpreted their vibronic structures successfully.[36,50-52] The evidences of the Renner-Teller effect in the Δ electronic state were observed in only a few molecules.[36,53] The $\tilde{A}\,^2\Delta$ state of CCN is one of the such examples. In Chapter IV, the vibronic structure of

the $\tilde{A}\,^2\Delta$ state of CCN will be discussed.

(b) The vibronic transition

In many studies of electronic transitions of the polyatomic molecules, vibronic transitions or vibronically induced transitions have been observed. In a similar manner as in the explanation of the Renner-Teller effect, a vibronically induced transition is explained in terms of breaking down of the Born-Oppenheimer approximation. As typical examples, one may refer to the $\tilde{A}\,^1A_2$-$\tilde{X}\,^1A_1$ transition of formaldehyde (H_2CO) and the $\tilde{A}\,^1B_{1u}$-$\tilde{X}\,^1A_{1g}$ transition of benzene (C_6H_6). Both of them are symmetrically forbidden electronic transitions under the Born-Oppenheimer approximation. As a result of the vibronic interaction, the selection rule for the *electronic* states is relaxed to that for the *vibronic* states. In the case of linear molecules, the first term in the perturbing Hamiltonian (2) can cause the vibronically induced transition. Without vibronic interactions, the vibronic states with even and odd ℓ are not mixed with each other. On the other hand, as the Herzberg-Teller interaction has the matrix elements with $\Delta\ell = \pm 1$, it mixes vibronic states with even and odd ℓ. As a result, the selection rule for ℓ in the Born-Oppenheimer state (even $\ell \leftarrow|\rightarrow$ odd ℓ) can be violated.

(c) The isoenergetic vibronic interaction; internal conversion (IC) and intersystem crossing (ISC)

Vibronic interactions described in (a) and (b) are explained in terms of the interaction between well-defined Born-Oppenheimer states $\{|\Lambda>|v^{\ell}>\}$. Their matrix elements are typically in the order of a few hundred cm^{-1}. Besides these vibronic interactions, internal conversion (IC) and

intersystem crossing (ISC) are also known as interactions breaking the Born-Oppenheimer approximation. Though the interaction energy of IC or ISC is less than 1 cm^{-1} in general, small energy differences (isoenergetic relation) of the interacting states make IC and ISC observable. An isoenergetic relation can be produced by high density of states, and sometimes by an accidental degeneracy, which is actually very rare. In most cases, the energy region of the vibrationally highly excited states in an electronic state has high density of states. In IC and ISC processes, such high-v states can form the background states interacting with a Born-Oppenheimer state, which is assigned vibronically in most cases.

IC couples a Born-Oppenheimer state and a set of background states with the same spin multiplicity. The matrix element of IC is represented as[54,55]

$$\left\langle \phi^s(q,Q)\chi_k^s(Q)\middle|T(Q)\middle|\phi^l(q,Q)\chi_{k'}^l(Q)\right\rangle \propto \sum_k \left\langle \phi^s\middle|\frac{\partial}{\partial Q_k}\middle|\phi^l\right\rangle \left\langle \chi_k^s\middle|\frac{\partial}{\partial Q_k}\middle|\chi_k^l\right\rangle \prod_{i\neq k}\left\langle \chi_i^s\middle|\chi_i^l\right\rangle \tag{3}$$

where $\phi^s(q,Q)\chi_k^s(Q)$ is a Born-Oppenheimer state for the k-th vibrational mode of the "s" electronic state, and q and Q are an electronic coordinate and a nuclear normal coordinate, respectively. The expression (3) is the matrix element for the non-adiabatic term,

$$T(Q) = \sum_k \left(-\frac{\hbar^2}{2\mu_k}\frac{\partial^2}{\partial Q_k^2}\right), \tag{4}$$

which is neglected in the molecular Hamiltonian under the Born-Oppenheimer approximation. In most cases, "s" is an excited electronic

state and "*1*" is the electronic ground state, where $\chi_k^l(Q)$ is a vibrationally highly excited state. In eq. (3), *k*-th mode is called as a "promoting mode" for IC. For example, the υ_4 mode (out-of-plane bending) of formaldehyde (H_2CO) has been often referred to a promoting mode in the studies of the non-radiative process in the $\tilde{A}$ state.[56] In general, since the normal mode Q_k is not a good representation for a vibrational coordinate in a vibrationally highly excited state, mode-specificity of IC in high v_k states is not obvious, at least when the vibrational states are described based on the normal coordinates, but it is known that the rate of IC is proportional to the density of states to be coupled as background states, $\rho(\varepsilon)$, at the term energy of ε.

In the case of ISC, spin multiplicities of interacting states are different from each other. The interaction term is $T(Q) + Hso$, where Hso is the spin-orbit interaction which connects vibronic states with different spin multiplicities. In most cases, ISC mixes the S_1 vibronic state with highly excited vibrational states in T_1, the origin of which lies at sufficiently low energy to have a large $\rho(\varepsilon)$ in the isoenergetic region of the S_1 vibronic state. As in the case of IC, the rate of ISC largely depends on $\rho(\varepsilon)$ of background states. Estimation of $\rho(\varepsilon)$ of the background states is of great help for measuring the ISC rate. For example, ISC have been observed in the S_1 states of biacetyl ($(CH_3CO)_2$)[57], pyrazine ($C_4N_2H_4$)[58], and propynal (HCC-CHO)[59] as quantum beats in the fluorescence decay, which are caused by the high $\rho(\varepsilon)$. In these studies, $\rho(\varepsilon)$ of T_1, which locates ~thousands cm^{-1} lower than S_1 (~2,500 cm^{-1} for biacetyl, 4,056 cm^{-1} for pyrazine, and 2,036 cm^{-1} for propynal), is estimated from both observed quantum beats and direct counting calculation using vibrational frequencies in T_1. Based on this comparison of observation with calculation for $\rho(\varepsilon)$, more detailed intramolecular processes such as competition of ISC and IC (of biacetyle[57]) and mixing of S_1 and T_1 via hyperfine interaction (of propynal[59]) have been discussed.

For the isoenergetic interactions such as IC and ISC, estimation of $\rho(\varepsilon)$ is important. If we know all the vibrational parameters in an electronic state, evaluation of $\rho(\varepsilon)$ is possible by the direct counting method or by the analytical formula derived by Haahoof.[60], Whitten et. al[61], and D. C. Tardy et. al[62]. Both methods were originally developed for demonstration of the RRKM theory, in which the reaction rate constant is inversely proportional to the densities of states at the initial stage of reaction. However, it is usually difficult to obtain a complete set of vibrational parameters even for small molecules, because anharmonic constants have a great influence on $\rho(\varepsilon)$ at a high term energy. In the case of linear molecules, the degeneracy of ℓ (v+1 states for a given v) for a bending excited state gives an additional complexity. Roughly, $\rho(\varepsilon)$ has the functional dependence of ε^{n-1}, where n is the number of the vibrational modes. A rapid increase of $\rho(\varepsilon)$ against ε is expected in larger molecules. In laser spectroscopy of HCCS described in Chapter V of this thesis reveals IC of the $\tilde{A}\,^2\Pi$ state with high-v states in the $\tilde{X}\,^2\Pi$ of this radical. The observed quantum beat in the fluorescence decay curve and the Douglas effect in the fluorescence lifetime of the $\tilde{A}$-$\tilde{X}$ transition will be explained in terms of intramolecular processes. In the following part of this chapter, theoretical backgrounds for the relation between the intramolecular relaxation processes and the temporal behaviors of fluorescence are described in a manner described by Bixon and Jortner[54,55], Lahmani et. al.[63], and Freed and Nitzen.[64]

3. Zero-field quantum beat induced by intramolecular processes

A quantum beat appearing in the fluorescence decay is a phenomenon caused by a quantum mechanical interference. A coherent excitation of a set of molecular eigenstates by a short pulse produces a single superposition state. The superposition state is composed of molecular

eigenstates within a coherent width of excitation at t =0. A contribution from each of the time-independent molecular eigenstates ({| j >}) to a superposition state ($\Psi(t = 0)$) is proportional to the electrical transition moment, < g | μ | j >, with an initial state | g >. A zero-order state | s > is introduced as a "bright" component in the transition, which corresponds to $\Psi(t = 0)$,

$$|s\rangle = \sum_{j}^{N} \langle g|\mu|j\rangle |j\rangle = \Psi(t = 0), \qquad (5)$$

where N is the number of molecular eigenstates excited coherently. A temporal behavior of fluorescence (I(t)) is represented as,

$$I(t) = |\langle s \,|\, \Psi(t)\rangle|^2. \qquad (6)$$

In the coherent excitation, at t = 0, N states of | j > have constant relative phases with each other. At t > 0, each molecular eigenstate evolves in time with its characteristic eigenfrequency, ω_j, and radiative lifetime, $1/\gamma_j$, that is, $|j\rangle \exp(-i\omega_j t)\exp(-\gamma_j t)$. This temporal behavior of the fluorescence decay, I(t), can be classified by a magnitude of N as follows.

(a) For N = 1

In this case, the fluorescence decay is represented as,

$$I(t) = A\exp(-\frac{t}{\tau_{rad}}), \qquad (7)$$

where τ_{rad} is the ensemble average of the radiative lifetime of the excited states ({| j >}). When N = 1, there is no intramolecular relaxation process and this type of a single exponential decay is observed.

(b) For N < –10

In this case, eq. (6) is simplified to eq. (8).

$$I(t) = \sum_{i,j}^{N} A_{ij} \exp(-\frac{t}{\tau_{rad}})\cos(\omega_i - \omega_j)t \quad , \qquad (8)$$

where $\hbar\omega_j$ is the term energy of the molecular eigenstate j.

(c) For N > –10

If many of the molecular eigenstates are excited coherently, the oscillating parts, $\cos(\omega_i-\omega_j)t$, in eq. (8) are averaged out and disappear. Considering the actual experimental conditions using a nanosecond laser pulse, a coherence width is on the order of 100 MHz, which is much smaller than a rotational constant of relatively small molecules. In order to excite several eigenstates coherently by a nanosecond laser pulse, energy intervals of eigenstates should be become small, i.e. ρ(ε) should become large. It is true that a molecule can have fine and hyperfine splittings within –100 MHz, but the number of eigenstates accompanied with a single rotational state can be predicted by treating the coupling of angular momenta (L, S, I, ...) correctly. Therefore, we can discriminate the coherent excitation of the fine or hyperfine split levels in a single rovibronic level from that of a number of vibrational levels. Intramolecular coupling with background states, such as IC, ISC, and IVR, can produce much larger ρ(ε) than –10 states per 100 MHz. We can classify this many-N case further into two cases by the intramolecular processes.

In the first case, I(t) is obtained simply by increasing N in eq. (8). After N eigenstates {| j > } are coherently excited at t = 0, the superimposed ${}_NC_2$ beat components interfere destructively since all of them evolve differently in time. As a result, a fast decay is observed together with the

exponential decay of eq. (7).

$$I(t) = C' \exp(-\Gamma t) + C'' \exp(-\frac{t}{\tau_{rad}}), \quad (9)$$

which was derived in reference 63. Γ in eq. (9) could be related to the rate constant of the intramolecular process. This situation corresponds to the case in which τ_{rad} in eq. (8) is not influenced by the intramolecular processes. Since τ_{rad} is related to the electronic character of the upper and lower states of the transition, if τ_{rad} is not changed even by a intramolecular process, the interaction is found to occur within a single electronic state. The intramolecular vibrational energy redistribution (IVR) is one of such cases, because main contribution to IVR is anharmonic coupling within the same electronic state. For example, fluorescence decay of anthracene ($C_{14}H_{10}$) induced by a short pulse was reported to exhibit a temporal behavior expressed as eq. (9).[65-67] The fast decay was related to the rate of IVR of anthracene in S_1, while the time constant of the slow decay did not depend on the rate of IVR.

In the second case, we consider the intramolecular process which changes the radiative lifetime τ_{rad}. We assume that the $| s >$ state in the excited state mixes with N states of $\{| l >\}$ (rigorously N-1) in another electronic state to produce N eigenstates of $\{| j >\}$, where $| s >$ and $\{| l >\}$ are zero-order basis functions, i.e., Born-Oppenheimer states, and the mixing is caused by the intramolecular process, which is represented as W in the molecular Hamiltonian. If $| l >$ has no transition moment with the ground state, $| g >$ (a "dark" zero-order state), the transition moment contributed from $| s >$ is distributed to N eigenstates of $\{| j >\}$. These diluted transition moments result in a longer radiative lifetime. A coherent excitation of N states of $\{| j >\}$ prepares a "bright" zero-order state $| s >$ via the electrical transition moment of $< g | \mu | s >$ at $t = 0$ (eq. (5)), and each eigenstate $| j >$

emits fluorescence proportional to $< g | \mu | j >$ at $t > 0$. In a simplest case, in which the matrix elements $< s | W | l >$s are equal for all $\{| l >\}$, emitting $< g | \mu | j >$ is equal to $< g | \mu | s > / N^{1/2}$. This means that the radiative lifetime is elongated by N times by the intramolecular process mixing the "bright" and "dark" zero-order states. In this case, apparently two exponential decays with different decay constants are observed as in eq. (9). However, notations are changed so that the difference in the situation is clarified.

$$I(t) = A^{+} \exp(-\frac{t}{\tau^{+}}) + A^{-} \exp(-\frac{t}{\tau^{-}}), \quad (10)$$

where τ^{+} is a faster decay constant related to the dephasing of the superposition state ("bright" zero-order state $| s >$ at $t = 0$) by the intramolecular non-radiative process (W), and τ^{-} is an averaged radiative lifetime of resultant molecular eigenstates $\{| j >\}$. In terms of ρ, which is an inverse of the averaged energy differences of the molecular eigenstates $\{| j >\}$, τ^{+} and τ^{-} are expressed as,

$$\tau^{+} = (2\pi w^2 \rho)^{-1} \quad = \Gamma^{-1}, \quad (11)$$

$$\tau^{-} = \tau_s / N, \quad (12)$$

where $w = < s | W | l >$ and τ_s is an inverse of Einstein's A coefficient calculated from $< s | \mu | g >$, which has been represented as τ_{rad} in eqs. (7)-(9). The internal conversion (IC) with other non-radiative (dark) Born-Oppenheimer states and the intersystem crossing (ISC) can change the radiative lifetime. In both cases, a long tail in the fluorescence decay is observed according to eq. (12). An anomalously longer radiative lifetime than that expected from the electronic properties is known as the Douglas effect.[68]

In understanding of the intramolecular relaxation process, following two pictures are essentially equivalent: (1) The zero-order state evolves *temporarily* in such manner as reflects the intramolecular process. (2) A number of molecular eigenstates which are *energetically* separated each other are produced as a result of the intramolecular process. The former corresponds to the observation of fluorescence decay in the time domain with a pulse laser, while the latter corresponds to resolve each molecular eigenstate within a coherence width of the pulsed laser by ultra high resolution spectroscopy with a cw laser. For example, in the study of non-radiative processes of pyrazine ($C_4H_4N_2$)[58], observation of quantum beats in the time domain and ultra high resolution spectroscopy in the frequency domain yielded equivalent information on ISC in S_1.

A temporal behavior of fluorescence contains information on intramolecular coupling with dark background states in excited electronic states. A non-exponential decay including quantum beats or a biexponential decay shows the evidence for intramolecuar process such as IVR, ISC, and IC in the excited electronic states. Fluorescence decay of HCCS described in Chapter V will show a gradual transition of the temporal behavior from a single exponential to a quantum beat, and finally to a biexponential with the Douglas effect. The non-radiative process in the $\tilde{A}$ state of HCCS is discussed from the measurements of fluorescence decay curve in the time domain.

4. Overview of the present studies

In this thesis, three carbon-chain free radicals, HC_4O, CCN, and HCCS have been studied. In the studies of the three radicals, various types of vibronic interactions discussed above are found. The vibronic

interactions studied in the present thesis are listed in Table I.

In Chapter II, spectroscopic methods applied in the present study will be described. Throughout this study, a pulsed-discharge nozzle (PDN) has been used to generate free radicals efficiently in a supersonic jet. FTMW spectroscopy combined with the PDN has been successfully applied to various unstable species including carbon-chain free radicals. Taking advantage of the PDN in the effective generation of free radicals demonstrated in FTMW spectroscopy, I have developed the PDN in order to apply it to optical spectroscopy. The optimized condition and design of the PDN in laser spectroscopy were somewhat different from these in FTMW spectroscopy. However, variety of produced free radical species and efficiency of their production will be demonstrated in laser spectroscopy as described in Chapters IV and V.

In Chapter III, Fourier-transform microwave (FTMW) spectroscopy of the HC_4O radical will be described. FTMW spectroscopy is a powerful spectroscopic method to obtain accurate data on the geometrical structure of molecules. In addition, it is able to resolve the hyperfine structure of free radical species, because low J transitions in centimeter-wave region is observed with high sensitivity by FTMW spectroscopy combined with supersonic jet technique. Obtained rotational constants for isotropically substituted species (DC_4O and $HC_4{}^{18}O$) will reveal the non-linear structure of the HC_4O radical, which is caused by the static Renner-Teller effect. In addition, it will be concluded from an analysis of the observed hyperfine structure that the unpaired electron of this radical is distributed out of the molecular plane, that is, the symmetry of the electronic ground state is A". The electronic ground state is found to be the lower member of the Renner-Teller pair. Similar discussion on distribution of the unpaired electron in HCO, HCCO, and HC_3O will give clear explanation for correspondence of even/odd of n with A"/A' symmetry of the electronic ground state of HC_nO group.

Table I. Vibronic interactions observed in the present study.

Carbon-chain radicals	Observed vibronic interaction	Spectroscopic method
(Chapter III)		
HC_4O	static Renner-Teller effect	FTMW
(Chapter IV)		
CCN	dynamic Renner-Teller effect in Π and Δ states	LIF
	vibronically induced band	
(Chapter V)		
HCCS	internal conversion	LIF in the time domain

In Chapter IV, laser induced fluorescence (LIF) spectroscopy of the $\tilde{C}\,^2\Sigma^+$- $\tilde{X}\,^2\Pi$ band system of the CCN radical will be described. A main part of this chapter will be devoted to the analyses of the $\tilde{C}\,^2\Sigma^+$- $\tilde{X}\,^2\Pi$ band system. Rotational analyses for the vibronic bands in the energy region from the origin to ~6,000 cm^{-1} higher than the origin will be made. Based on the determined band origins, an almost complete set of vibrational frequencies (ω_i, i=1,2,3) and anharmonic constants (x_{ij}, i,j=1,2,3, and g_{22}) of the $\tilde{C}\,^2\Sigma^+$ state will be obtained. Although these vibronically induced bands are very weak, we are able to observe vibronically induced bands with $\Delta\ell \neq 0$ with a good signal-to-noise ratio because of the high sensitivity of LIF spectroscopy and of the high production efficiency of the PDN. Combining these data with previously reported data on $\Delta\ell = 0$ sequence bands, vibronic parameters containing the Renner-Teller parameters for the $\tilde{X}\,^2\Pi$ and $\tilde{A}\,^2\Delta$ states will be determined. Both of these two degenerate electronic states will be found to be affected by the Renner-Teller effect. The mechanism of the occurrence of the vibronically induced bands observed in the $\tilde{C}$ - $\tilde{X}$ transition will be also discussed.

In Chapter V, LIF spectra of the $\tilde{A}\,^2\Pi$- $\tilde{X}\,^2\Pi$ band system of the HCCS radical will be studied. From rotational analyses of the observed jet-cooled spectra, the upper and lower Ω ($=\ell+\Sigma+\Lambda$) in respective vibronic transitions will be assigned. Previous assignments for some vibronic bands will be found to be incorrect. Furthermore, quantum beat phenomena observed in the time domain will provide information on the intramolecular non-radiative process in the excited electronic state of this radical. It will be clearly shown that the number of beat components increases as the vibronic term energy. This gradual change of the quantum beat patterns as a function of the vibronic term energy suggests that the intramolecular process is directly governed by $\rho(\varepsilon)$. Internal conversion, which is one of the isoenergetic vibronic interactions mentioned in 2 of this Chapter, will be

found to be the main origin of the observed quantum beats. An estimation of $\rho(\varepsilon)$ of the electronic ground state at the isoenergetic region of the $\tilde{A}$ state using direct counting method will support this conclusion.

References

[1]R. J. Saykally, L. Veseth, and K. Evenson, J. Chem. Phys. 80, 2247 (1984).

[2]K. V. L. N. Sastry, P. Helminger, A. Charo, E. Herbst, and F. C. de Lucia, Astrophys. J. 251, L119 (1981).

[3]C. A. Gottlieb, E. W. Gottlieb, and P. Thaddeus, Astrophys. J. 264, 740 (1983).

[4]Y. C. Hsu, J. J. Lin, D. Papousek, and J. J. Tsai, J. Chem. Phys. 98, 6690 (1993).

[5] Y. C. Hsu, Y. J. Shiu, and C. M. Lin, J. Chem. Phys. 103, 5919 (1995).

[6]S. Yamamoto, S. Saito, H. Suzuki, S. Deguchi, N. Kaifu, S. Ishikawa, and M. Ohishi, Astrophys. J. 348, 363 (1990).

[7]C. A. Gottlieb, E. W. Gottlieb, P. Thaddeus, and J. M. Vrtilek, Astrophys. J. 303, 446 (1986).

[8]C. A. Gottlieb, E. W. Gottlieb, and P. Thaddeus, and H. Kawamura, Astrophys. J. 275, 916 (1983).

[9]W. Chen, S. E. Novick, M. C. McCarthy, C. A. Gottlieb, and P. Thaddeus, J. Chem. Phys. 103, 7828 (1995).

[10]L. N. Shen, T. J. Doyle, and W. R. M. Graham, J. Chem. Phys. 93, 1597 (1990).

[11]K. Hoshina, H. Kohguchi, Y. Ohshima, and Y. Endo, in preparation.

[12]C. A. Gottlieb, E. W. Gottlieb, and P. Thaddeus, Astrn. Astrophys. 164, L5 (1986).

[13]J. C. Pearson, C. A. Gottlieb, D. R. Woodward, and P. Thaddeus, Astrn. Astrophys. 189, L13 (1988).

[14]S. L. N. G. Krishnamachari and D. A. Ramsay, Faraday Discuss. Chem. Soc. 71, 205 (1981).

[15]B. Coquart, Can. J. Phys. 63, 1362 (1985).

[16]J. M. Vrtilek, C. A. Gottlieb, E. W. Gottlieb, W. Wang, and P. Thaddeus, Astrophys. J. 398, L73 (1992).

[17]M. C. McCarthy, J. M. Vrtilek, E. W. Gottlieb, F. M. Tao, C. A. Gottlieb,and P. Thaddeus, Astrophys. J. 431, L127 (1994).
[18]Y. Hirahara, Y. Ohshima, and Y. Endo, J. Chem. Phys. 101, 7342 (1994).
[19]Y. Endo and Y. Ohshima, J. Chem. Phys. 98, 6618 (1993).
[20]M. C. McCarthy, C. A. Gottlieb, A. L. Cooksy, and P. Thaddeus, J. Chem. Phys. 103, 7779 (1995).
[21]Y. Endo and E. Hirota, J. Chem. Phys. 86, 4319 (1987).
[22]Y. Ohshima and Y. Endo, J. Mol. Spectrosco.159, 458 (1993).
[23]A. L. Cooksy, J. K. G. Watson, C. A. Gottlieb, and P. Thaddeus, J. Mol. Spectrosco.153, 610 (1992).
[24]A. L. Cooksy, J. K. G. Watson, C. A. Gottlieb, and P. Thaddeus, Astrophys. J. 386, L27 (1992).
[25]H. Kohguchi, Y. Ohshima and Y. Endo, J. Chem. Phys. 101, 6463 (1994).
[26]S. Yamamoto, S. Saito, K. Kawaguchi, Y. Chikada, H. Suzuki, and N. Kaifu, Astrophys. J. 318, 361 (1990).
[27]S. Saito, K. Kawaguchi, S. Yamamoto, M. Ohishi, H. Suzuki, and N. Kaifu, Astrophys. J. 317, L115 (1987).
[28]Y. Ohshima and Y. Endo, J. Mol. Spectrosco. 153, 627 (1992).
[29]Y. Hirahara, Y. Ohshima, and Y. Endo, Astrophys. J. 408, L113 (1993).
[30]Y. Kasai, K. Obi, Y. Ohshima, Y. Hirahara, Y, Endo, K. Kawaguchi, and A. Murakami, Astrophys. J. 420, L45 (1993).
[31]M. Fujitake, R. Kiryu, and N. Ohashi, J. Mol. Spectrosco. 154, 169 (1992).
[32]Y. Ohshima, Y. Endo, and T. Ogata, J. Chem. Phys. 102, 1493 (1995).
[33]T. Ogata, Y. Ohshima, and Y. Endo, J. Am. Chem. Soc. 117, 3593 (1995).
[34]M. Ohishi, N. Kaifu, K. Kawaguchi, A. Murakami, S. Saito, S. Yamamoto, S. Ishikawa, Y. Yoshida, Y. Shiratori, and W. M. Irvine, Astrophys. J. 345, L83 (1989).
[35]W. Weltner Jr. and D. McLeod Jr., J. Chem. Phys. 41, 235 (1964).
[36]A. J. Merer and D. N. Travis, Can. J. Phys. 43, 1795 (1965).
[37]Y. Ohshima and Y. Endo, J. Mol. Spectrosco. 172, 225 (1995).

[38]J. T. Hougen J. Chem. Phys. 36, 519 (1962).
[39]J. F. M. Aarts, Mol. Phys. 35, 1785 (1978).
[40]J. M. Brown, J. Mol. Spectrosco. 68, 412 (1977).
[41]J. M. Brown and F. Jørgensen, Adv. Chem. Phys. 52, 117 (1983).
[42]S. Carter, N. C. Handy, P. Rosmus, and G. Chamband, Mol. Phys. 71, 605 (1990).
[43]M. Bommer, P. Rosmus, S. Carter, and N. C. Handy, Mol. Phys. 77, 549 (1992).
[44]W. H. Green, N. C. Handy, P. J. Knowles, and S. Carter, J. Chem. Phys. 94, 118 (1991).
[45]C. Bauer, D. M. Hirst, D. I. Hall, P. J. Sarre, and P. Rosmus, J. Chem. Soc. Faraday Trans. 90, 517 (1994).
[46]B. Weis and K. Yamashita, J. Chem. Phys. 99, 0512 (1993).
[47]K. Dressler and D. A. Ramsay, J. Chem. Phys. 27, 971 (1967).
[48]J. W. C. Johns and G. Herzberg, Proc. Roy. Soc. 298A, 142 (1967).
[49]G. Herzberg and D. A. Ramsay, Proc. Roy. Soc. 233A, 34 (1955).
[50] J. W. C. Johns, Can. J. Phys. 39, 1738 (1961).
[51]L. Gausset, G. Herzberg, A. Lagerqvist, and B. Rosen, Astrophys. J. 142, 45 (1965).
[52]R. N. Dixon, Philos. Trans. R. Soc. London Ser. A, 252, 165 (1980).
[53]A. J. Merer and D. N. Travis, Can. J. Phys. 44, 353 (1966).
[54]M. Bixon and J. Jortner, J. Chem. Phys. 48, 715 (1968).
[55]M. Bixon and J. Jortner, J. Chem. Phys. 50, 4061 (1969).
[56]R. G. Miller and E. K. C. Lee, J. Chem. Phys. 68, 4448 (1978).
[57]J. Chaiken, M. Gurnick, and J. D. McDonald, J. Chem. Phys. 74, 106 (1981).
[58]J. Kommandeur, W. A. Majewski, W. L. Meerts, and D. W. Pratt, Ann. Rev. Phys. Chem. 38, 433 (1987).
[59]H. Bitto, P. R. Willmott, and J. R. Huber, J. Chem. Phys. 95, 4765 (1991).
[60]P. C. Haarhoff, Mol. Phys. 6, 337 (1963) , Mol. Phys. 7, 101 (1963).

[61]G. Z. Whitten and B. S. Rabinovitch, J. Chem. Phys. 38, 2466 (1963).
[62]WD. C. Tardy, B.S. Rabinobitch, and G. Z. Whitten, J. Chem. Phys. 48, 1427 (1963).
[63]F. Lahmani, A. Tramer, and C. Tric, J. Chem. Phys. 60, 4431 (1974).
[64]K. F. Freed and A. Nitzen, J. Chem. Phys. 73, 4765 (1980).
[65]P. M. Felker and A. H. Zewail, J. Chem. Phys. 82, 2961 (1985).
[66]P. M. Felker and A. H. Zewail, J. Chem. Phys. 82, 2975 (1985).
[67]P. M. Felker and A. H. Zewail, J. Chem. Phys. 82, 2994 (1985).
[68] A. E. Douglas, J. Chem. Phys. 45, 1007 (1966).

Chapter II

Experimental setups

1. Fourier-transform microwave spectroscopy of carbon-chain free radicals
2. Laser induced fluorescence spectroscopy of carbon-chain free radicals
3. Pulsed-discharge nozzle
4. Application of a PDN to the study of electronic transitions of free radicals

1. Fourier-transform microwave (FTMW) spectroscopy of carbon-chain free radicals

Microwave spectroscopy is a very powerful method for accurate determination of the molecular structure. This is because we can use microwave source with high resolution and the Doppler width in the microwave region is less important. The molecular structure is the most important property of the molecule. Millimeter- (30-300 GHz) and submillimeter- (300 GHz-) wave spectroscopy have revealed the molecular structures of the polyatomic free radicals by observing the pure rotational absorption spectra of relatively high J transitions. Pure rotational transitions can be observed for the most of polyatomic free radicals, except for molecules with high symmetry and no permanent dipole moment. Most of polyatomic radicals provide the pure rotation spectra.

In the present study, the spectroscopic data of the polyatomic free radical (HC_4O radical in Chapter III) by FTMW spectroscopy, which has a great potential to observe pure rotational transitions in centimeter-wave region (3-30 GHz), was obtained. Pure rotational spectra of low J transitions (including the lowest rotational transition in many cases) of polyatomic molecules are observed in the centimeter wave region. As well as an accurate rotational constant gives us important information on the molecular structure, the hyperfine structure of the free radicals observed by microwave spectroscopy provides much information on the distribution of the unpaired electron in a free radicals. This means that microwave spectroscopy observing the hyperfine structure of a free radical gives us data on the electronic wavefunction. Since hyperfine splittings are in general rapidly decreased in proportion to $1/J(J+1)$, observation of the low J transitions is indispensable to obtain the resolved hyperfine structure.

High sensitivity of FTMW spectroscopy is due to the principal of the

method, which is different from that of the microwave absorption spectroscopy. A schematic diagram of FTMW spectrometer is shown in Fig. 1. Pulsed microwave produces the superposition state of molecules, which is coherent with the incident pulsed microwave, and the macroscopic electric dipole moment is induced. After the incident microwave passes away from the cavity, the macroscopic dipole moment oscillating with the molecular transition frequency is observed as a free induction decay (FID), whose decay constant is determined by the dephasing processes of intermolecular coherency. Divergence of a jet stream from a PDN contributes dominantly to the dephasing. FTMW spectroscopy observes the FID signal as a function of time. The FID signal is converted to the signal of DC ~ 3 MHz by two-step superheterodyne scheme. Power spectra in the frequency-domain are obtained by the Fourier-transform procedure. Since FTMW spectroscopy observes the FID signal in zero background, it can obtain the high sensitivity free from noise of the microwave source.

Since FTMW spectroscopy is operating in pulsed scheme, it matches well with a supersonic jet technique with a pulse valve. A supersonic jet technique compresses molecular population into low J states, and increases the effective sensitivity of detection. As well as effectively increasing molecular population to be detected, the collisionless condition in a supersonic jet is significant for observing free radicals.

2. Laser induced fluorescence spectroscopy of carbon-chain free radicals

Laser induced fluorescence (LIF) spectroscopy itself is a highly sensitive method of observing electronic transitions and widely used in many studies on electronic excited states. LIF spectroscopy yields information on wider range of vibrational energy structures of molecules. Analyses of LIF spectra enable us to reproduce the potential energy surface

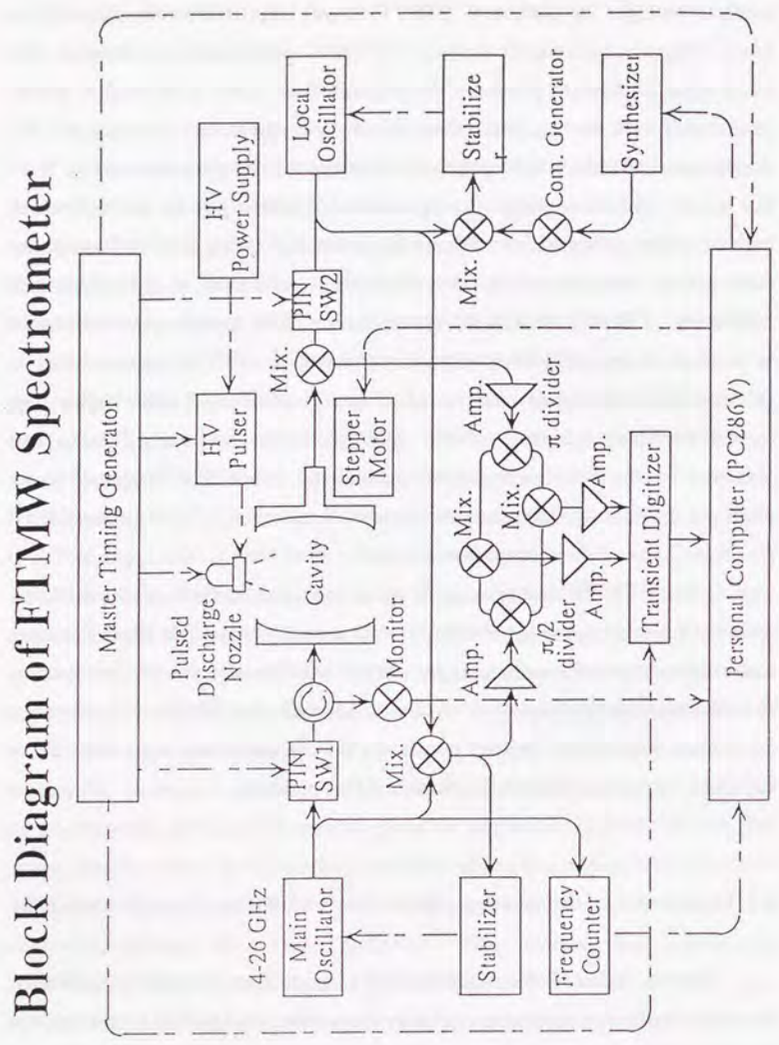

Figure 1 Block diagram of the Fourier-transform microwave spectrometer.

of the excited state, if observed LIF spectra covered widely enough with the excited electronic states. LIF spectra of polyatomic free radicals shows, in many cases, a complex band structures, which are ascribed to the vibronic interaction or the spin-orbit interaction. The rotational structures of an open-shell species contain more lines than that of a closed-shell small molecules even in a jet cooled spectra. The vibronic parameters can be obtained by analyses of the complex vibronic and rotational structures based on the theories of the vibronic interaction descried in Chapter I to the observed LIF spectra. Though the rotational constant derived from the LIF spectra is not as accurate as to determine the molecular structure as by MW spectroscopy, the rotational structure in LIF spectra gives us conclusive evidence for identifying the carrier of spectra.

LIF spectroscopy is restricted by a Franck-Condon factor and non-radiative processes such as predissociation in an excited electronic state. A small Franck-Condon factor limits excitation of molecules and fast intramolecular processes limits fluorescence from the excited electronic state. In LIF spectroscopy, radiative lifetime τ, which is determined by fitting fluorescence decay to $\exp(-t/\tau)$, contains information on excited state. Much smaller decay constant than expected suggests dissociation or internal conversion in the excited electronic state. A temporal behavior of fluorescence other than a single exponential decay, such as a quantum beat and biexponential decay, provides quantitative data on intramolecular relaxation processes in the excited state. Observation of fluorescence in the time-domain is one of applications of LIF spectroscopy.

Recently, many of new kinds of carbon-chain free radicals have been detected by IR and MW spectroscopy in the electronic ground state due to development of effective method for producing free radicals and sensitivity of detection. Not a many of the electronic transitions of such recently detected radicals have been known. LIF spectroscopy of moderately long carbon-chain radicals ($n \geq 3$) has not been made. In the spectroscopic study of free

radicals, the efficiency of producing unstable species is one of the most crucial techniques. Laser photolysis has been combined with laser spectroscopy of free radicals, while, IR and MW spectroscopy have been successfully applied to various kinds of carbon-chain radicals by using discharging method. In the present study, I have applied a discharging method (PDN) to laser spectroscopy, and detail on generating method will be described in the following section.

A schematic diagram of the setup for LIF spectroscopy is shown in Fig. 2. A 14 inch diffusion pump with a flow rate of 3,000 ℓ/sec was attached to a vacuum chamber. A water cooled baffle was used for preventing backstreaming of the oil, which sticks to the PDN and makes pulsed electric discharge unstable. The vacuum chamber was kept at 1×10^{-4} Torr during the observation by the diffusion pump backed by a roots blower pump (600 ℓ/sec) and a rotary pump (950 ℓ/min). A pair of 220 mm long arms with Brewster angle are attached to the chamber to allow the laser light to pass through. The arm contained 5 slotted disks to allow passage of laser light. These disk have 15mmØ slot and their outside diameter were matched to the internal diameter of the arm tube. Spacing between disks inside the arm tube was maintained by 50 mm long length of aluminum tube.

A tunable dye laser (Spectra Physics PDL-3) pumped by a Q-switched Nd^+ YAG laser (Spectra Physics GCR-3) was used. The frequency range can be extended up to near UV region by using KDP or BBO crystal. Linewidth (FWHM) of the visible and frequency-doubled radiation are 0.08 cm^{-1} and 0.12 cm^{-1}, respectively. A pulsed light was incident at 40 mm downstream from the PDN. A pair of convex lenses (60 mmØ, f = 90 mm and 60 mmØ, f = 120 mm) was used to focus and collect fluorescence signal. A photomultiplier tube (Hamamatsu photonics R928) was used, and output from the photomultiplier was amplified by a pre-amplifier. The amplified signal was integrated by a boxcar gated integrator (SRS SR250). Integrated signal for every laser shot was digitized by an A/D converter and

Block diagram of the PDN-LIF setup

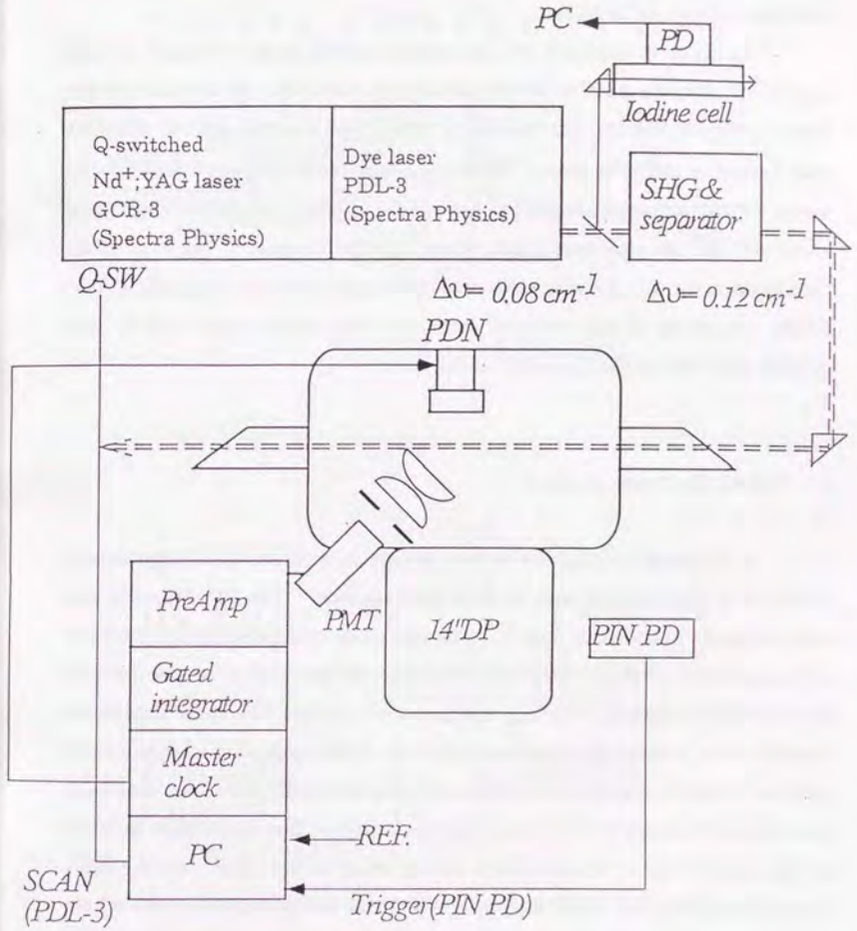

Figure 2 Schematic diagram of the setup for LIF spectroscopy.

stored into a computer. The data acquisition was triggered by a PIN photo diode detector monitoring the laser pulse. Q-switch of the laser, pulsed discharge, and opening of a pulse valve were synchronized by a master oscillator operating at 10 Hz.

In order to calibrate the wavelength of the laser, recorded an LIF spectra of iodine in a cell were recorded simultaneously. In scanning of the range under 13,000 cm^{-1} (or 26,000 cm^{-1} with SHG crystal) the cell of iodine was heated to 200°C or more. This is because the LIF spectra of I_2 ($\tilde{B}$-$\tilde{X}$) under 13,000cm^{-1} were ascribed to hot bands. Calibration of the abscissa of observed LIF spectra was made based on the frequency table of I_2 (S. Gerstenkorn *et al.*, *Atlas du Spectre d'Absorption de la Molecule d'Iode*, 1982). Accuracy of the observed transition frequencies calibrated by this procedure is within the linewidth of the laser.

3. Pulsed-discharge nozzle

A characteristic device in our setups is a pulsed-discharge nozzle (PDN) as a generator of carbon-chain free radicals. The PDN used in the present study is shown in Fig. 3. The efficiency of producing free radicals in a supersonic jet stream has been demonstrated in microwave spectroscopy for unstable molecules. In any spectroscopic regions, the most important experimental point in the spectroscopic study of the radical species is how to produce as much unstable molecules as to be detected. It is true that total amount of molecules is small in a supersonic jet, but that population in low J levels is recovered by the adiabatic cooling effect of the PDN. As the laser can excite a relatively small molecule in a single rovibronic state, as a whole effective sensitivity of detection is fairly good in spite of small total amount. The rotational temperature of free radicals produced by a PDN is as cold as 1-5K. In addition to simplifying spectra and raising effective sensitivity,

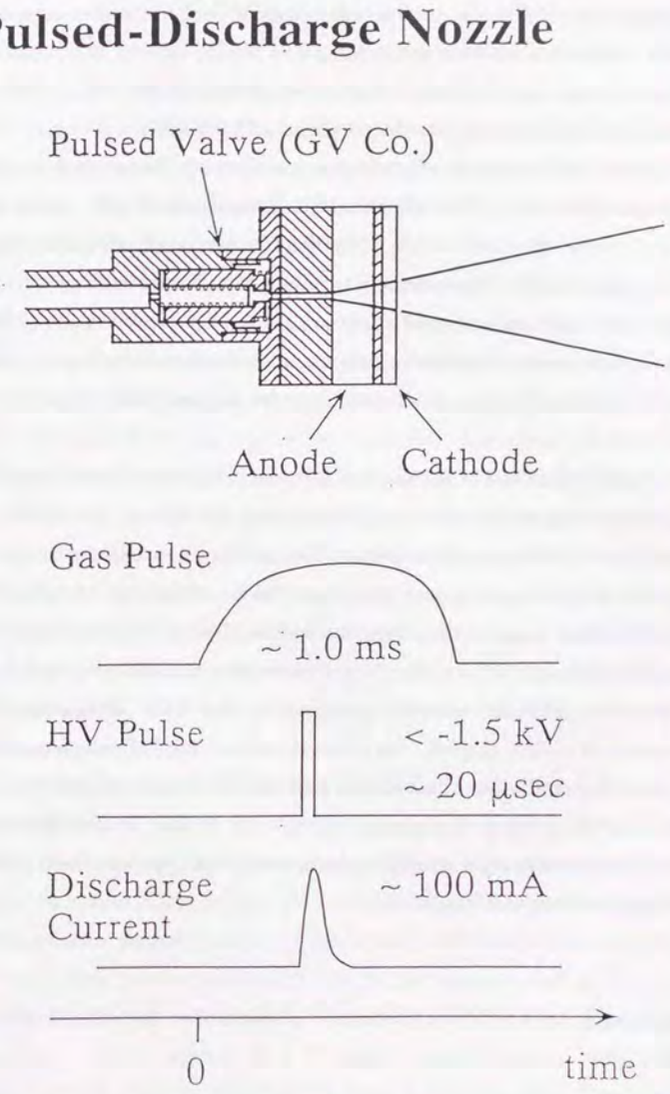

Figure 3 Schematic diagram of the pulsed-discharge nozzle (PDN).

the collisionless condition is another advantage of the PDN in observing free radicals. After free radicals are produced in the PDN, they do not collide with other atoms or molecules. This limits decomposition process of free radicals, which is physically stable but chemically unstable.

While both processes of production and decomposition are competing in a discharging cell. The simultaneous decomposition rate limits the amount of radical species in a cell. The PDN freezes population of unstable molecules immediately after production. Both FTMW spectroscopy and LIF spectroscopy used in the present study are made in pulse operation. They need enough amount of molecules only during their detection time (~ micro second). This small duty ratio of detection provides good matching with the PDN.

Photolysis is one of the most widely used methods of producing free radicals in a supersonic jet. Especially laser photolysis, in which an excimer laser is used in many experiments, has been successfully combined with laser spectroscopy. Laser photolysis takes advantage of particular chemical reaction process, in which the chemical bond of precursor to be cleaved is specified. While, the PDN cleaves plural chemical bonds in a precursor. In addition, complex reactions in the PDN elongation and enlargement of radical species. As a result, various kind of polyatomic free radicals can be produced. This means that the PDN has less selectivity of species and identifying the carrier of spectra is not straightforward. However, jet cooled spectra simplifies the rotational structures, which enable us to identify the carrier conclusively.

4. Application of a PDN to the study of electronic transitions of free radicals

In Chapters IV and V, a PDN has been applied to the studies on the

electronic transition of the carbon-chain free radicals. Since a photomultiplier tube (PMT) was used for detecting fluorescence in these studies, scattered light from the PDN was detected as a very strong noise. The output from the PMT in a single pulse operation is shown in Fig. 4. Observed emitted light from discharge can be distinguished temporally as two parts; The first light is strong and the second one is relatively weak but temporarily broadened as in Fig. 4.

The first part is strong emitted light during the high voltage pulse for discharging. The duration is 20 μsec. Direct incidence of this scattered light to the PMT was avoided by using a pair of convex lenses and irises. In spite that the PDN was placed out of the acceptance angle of the PMT, stray light reflected from the wall of the chamber was observed because the scattered light during discharging was strong. However, this scattered light can be distinguished temporally from the fluorescence signal as seen in Fig. 4. Typical velocity of jet stream is 500 m/sec when Ar is used as carrier gas. Since laser light was incident 40 mm downstream from the PDN, the produced radicals arrived at the observed area 80 μsec after the pulsed discharging. Therefore simultaneous scattered light with the pulsed discharging did not cause a significant noise in observing laser induced fluorescence actually.

The second emitted light is a prominent noise for the detection. The second scattered light is emission from metastable Ar*. Metastable Ar*, which were produced by discharging with quite high efficiency, had much longer radiative lifetime than 100 μsec. Produced free radicals passed the observed area together with the metastable Ar* which survive radiating. Emission from the metastable Ar* had the broad spectral range from visible to near-ultraviolet and complete removal by a sharp-cut filter was not attained. Both spatial and temporal discrimination was difficult. Fluctuation of emission from Ar* in every pulse operation determined the noise level of LIF spectra. The first gate of a boxcar integrator was set a

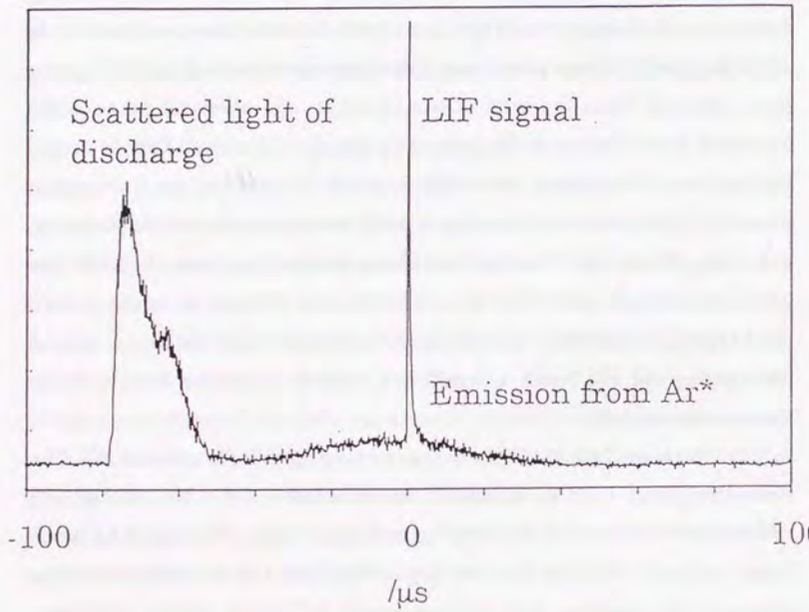

Figure 4 Time profile of the output from the photomultiplier monitoring the laser induced fluorescence signal with the pulsed-discharge-nozzle.

few nano seconds before incident of laser light and the second gate was set just after laser light. Subtraction of emission in the second gate from the output of the first gate was efficient for making the baseline of LIF spectra flat.

The dual gates and subtraction procedure were used during scanning in order to flatten the baseline. Fluctuation of fluorescence itself was more significant than that of the baseline. Fluctuation of the laser power and that of production of radicals in every pulse operation were considered to be 10 % and 100%, respectively. Stable discharging in every pulse is indispensable to obtain the rotational structures which can be compared with the simulation in analyses.

Important factors for stable pulsed discharging are ingredient of the sample gas, concentration of precursors in carrier gas, voltage for pulsed discharging, duration of the high voltage pulse, stagnation pressure, amount of gas to be injected and so on. The best condition depends on the species to be produced. Ar was usually used as a carrier gas, because He and Ne needed the higher voltage to be discharged than Ar, and stable discharge was difficult for He and Ne even by a higher voltage. This corresponds to the number of electrons and the ionization potentials of atoms (24.6 eV for He, 21.6 eV for Ne and 15.8 eV for Ar).

Chapter III

Pulsed-discharge nozzle Fourier-transform microwave spectroscopy of the HC_4O radical

ABSTRACT

A new carbon-chain free radical, HC_4O, has been identified in the gas phase through its rotational spectrum. The molecule has been generated in a supersonic free jet by electric discharge of an acetylene/oxygen mixture diluted in Ar, and detected by a Fabry-Perot type Fourier-transform microwave spectrometer. Four harmonically related rotational transitions have been observed in the 9-23 GHz region. They all showed fine structure splittings accompanied with well resolved hyperfine structures due to the hydrogen nucleus. Observation of other isotopomers, DC_4O and $HC_4{}^{18}O$, has yielded confirmation for the molecular species. The observed spectra have been well characterized as $K_a = 0$ transitions of a slightly asymmetric top molecule in a doublet vibronic state. The effective centrifugal distortion constant has been found to be fairly large, implying that the molecule has a bent carbon-chain framework. The present observation indicates that the radical is subjected to a strong (*i.e.*, static) Renner-Teller interaction, resulting in a complete quenching of the orbital angular momentum in a nonlinear molecular structure as is the case of shorter members of the HC_nO series. The isotropic hyperfine coupling constant shows that almost half of the unpaired electron lies on the carbon atom adjacent to the hydrogen.

1. INTRODUCTION

Rotational spectroscopy in the millimeter-wave (MMW) and submillimeter-wave (SMMW) regions has been extensively applied to the studies of unstable molecular species, where molecules to be studied are usually generated by glow discharge in a flow cell. For transient molecules with smaller rotational constants, however, MMW spectroscopy in a cell tends to reduce its potentiality, since molecules are distributed to more states at room temperature and individual transitions become relatively weaker. Recently, we have developed an alternative approach for the study of short-lived molecules, where transient species are generated by pulsed discharge in a supersonic expansion, and subsequently detected by a Fourier-transform microwave spectrometer with a Fabry-Perot cavity. This pulsed-discharge nozzle Fourier-transform microwave (PDN-FTMW) spectrometer is especially suitable for molecules with small rotational constants because it has high sensitivity in a relatively low frequency region and the state distribution is restricted to low energy levels by adiabatic cooling of the internal degrees of freedom. In addition, high resolving power of the FTMW spectrometer enables us to observe almost fully resolved hyperfine structures in low-J rotational transitions, which give us valuable information on the electronic structure of radicals. Potentiality of this method has been demonstrated by previous studies of short-lived radical species, such as HCCN,[1] HCCO,[2] and C_nS (n=3-5).[3-5]

Among various kinds of free radicals so far investigated, a series of species, which are expressed as HC_nO, has substantial importance in combustion processes[6,7] and interstellar chemistry.[8,9] The first member of this series, HCO, is one of the most thoroughly studied polyatomic radicals. Since the first identification of the radical by electronic absorption spectra,[10] it has been repeatedly investigated by spectroscopists in various wavelength regions from MW[11] to UV.[12] It has been established that this radical is subjected to a strong vibronic interaction, i.e., the Renner-Teller interaction. The two lowest electronic states correlate to a doubly degenerated state in a linear configuration, even though the potential curves of the two states are distinctly separated through the

interaction as the H-C-O angle decreases. In the ^{2}A' electronic ground state, this radical is reported to have the H-C-O angle of −120° at its equilibrium configuration.[13]

The geometrical structure of HCCO, which is the second member of the HC_nO series, has been studied by its rotational spectrum observed in the SMMW region.[14] The radical has been reported to have a bent planar structure with the H-C-C angle of −140°, having the ^{2}A" electronic ground state. Unusually large K_a dependence of the spin-rotation coupling constant has been ascribed to the second-order spin-orbit interaction between the electronic ground state and the low-lying counterpart of the Renner-Teller pair. The energy difference between the two states has been estimated to be only 540-3200 cm^{-1} from the coupling constant. More recently, the hyperfine structure in the lowest rotational transition has been studied by PDN-FTMW spectroscopy in this laboratory, and the electronic structure of the radical has been discussed on the basis of the precisely determined hyperfine coupling constants.[2]

The third member, HC_3O, has recently been identified by rotational spectroscopy in the MMW and SMMW regions.[15,16] It has been concluded that this species also has a bent planar structure with the ^{2}A' electronic ground state. The molecule is reported to be bent at the carbon atom adjacent to the oxygen atom, which resembles the structure of the propinal aldehyde, H-C≡C-CHO, with one hydrogen in the aldehyde group removed.[17]

In this chapter, the first spectroscopic identification of the next longer member of the HC_nO series, namely, HC_4O, by PDN-FTMW spectroscopy is reported. Low-N rotational transitions have been observed for the normal, deuterated, and ^{18}O-substituted isotopomers. An analysis for the experimental data has yielded the rotational, centrifugal distortion, and magnetic hyperfine coupling constants, which have been used to derive the geometrical and electronic structure of this radical.

2. EXPERIMENTAL

The experimental apparatus used in the present study is a Balle-Flygare type FTMW spectrometer,[18] equipped with a pulsed-discharge nozzle (PDN) to generate unstable molecular species in a supersonic free jet. Details of the setup have been described in Chapter II. HC_4O was produced by electrically discharging a mixture of 0.5 % C_2H_2 and 0.5 % O_2 diluted in Ar inside the PDN, and immediately expanded into a Fabry-Perot cavity. The stagnation pressure was kept at about 5 atm. High voltage of about 1 kV was applied to ignite the discharge between two electrodes of the PDN. The typical discharge current was 100 mA with a duration of 0.1 msec.

For a study of open shell species such as HC_4O, the terrestrial magnetic field, which would cause observable splittings or broadenings of lines by the Zeeman effect in the rotational spectrum, must be canceled. Three Helmholtz coils were located perpendicular to each other around the vacuum chamber, and adjusted the currents fed to the coils to cancel the terrestrial field. Compensation of the magnetic field was carried out by monitoring the Λ-type doubling transitions in $J = 5/2$ of the OH radical ($^2\Pi_{3/2}$) around 6035 MHz. The observed line widths (FWHM) for radical species were 50-80 kHz, which were slightly broader than those for singlet molecules, 20-50 kHz, indicating an influence of the residual magnetic field.

Two isotopomers, DC_4O and $HC_4{}^{18}O$, were also observed by using mixtures, C_2D_2/O_2 and $C_2H_2/{}^{18}O_2$, respectively, as sample gases. Both the normal and deuterated acetylenes were synthesized by the reaction of calcium carbide with H_2O or D_2O. ${}^{18}O_2$ (99.0% isotope purity) and normal O_2 were purchased from ISOTECH Inc. and Jonan Kyodo Sanso Inc., respectively, and used without further purification. It is noted that the discharge of the C_2H_2/O_2 system in the supersonic expansion has a large preference for the formation of HC_nO with even n, compared to that of odd n; signals of HC_3O were found to be weaker by one order of magnitude than those of HCCO and HC_4O. When a mixture of C_2H_2 and CO was tested as a sample gas, signals of HC_4O were 20 times weaker than those in the case of the C_2H_2/O_2 system. The C_2H_2/CO system gave the signals of HC_3O

with comparable intensity as the C_2H_2/O_2 system.

Transitions of HC_4O were first identified in the 13 GHz region as a paramagnetic doublet with a 30 MHz separation, each of which showed further splitting of about 0.5 MHz. In Fig. 1 is shown a typical spectrum, in which two hyperfine components are clearly resolved. Extension of the search to other frequency regions revealed that the doublet made a harmonically related series with an interval of 4.4 GHz. The observed spectral pattern was well characterized as rotational transitions of a linear molecule in a $^2\Sigma$ vibronic state, or alternatively those with $K_a = 0$ levels of a slightly prolate asymmetric top molecule in a doublet vibronic state. The observed hyperfine structure was characteristic of a radical with an $I = 1/2$ nuclear spin, indicating that the carrier of the spectrum contains a hydrogen atom. It was confirmed that this species contains an oxygen atom by using a sample gas without O_2. Judging from the size of the rotational constant, the species was tentatively identified as HC_4O. This identification was finally confirmed by observing spectra of other isotopomers; transitions for DC_4O and $HC_4{}^{18}O$ were observed in the expected frequency regions. The hyperfine structure of DC_4O was characteristic of that of $I = 1$, in contrast to those of HC_4O and $HC_4{}^{18}O$.

Further search was conducted covering 750 MHz around the $N_{KaKc} = 4_{04} - 3_{03}$ transition which was observed with the best signal-to-noise ratio under the present experimental condition, but could not observe other paramagnetic lines which could be attributed to HC_4O. This fact has ensured that the observed transitions are associated to the ground vibronic state of the HC_4O radical, and that either the transition with $K_a = 1$ is too weak to be detected or the molecule is linear.

Rotational transitions of HC_4O from $N = 2 - 1$ at 9.1 GHz to $N = 5 - 4$ at 22.8 GHz were observed. All of the observed transition frequencies are listed in Table I in Appendix. The transition frequencies for DC_4O and $HC_4{}^{18}O$ are also listed in Tables II and III in Appendix, respectively. The $N = 5 - 4$ transition for DC_4O was observed at 21.5 GHz, but the transition frequencies were not included in the following least-squares analysis because the hyperfine structure was not

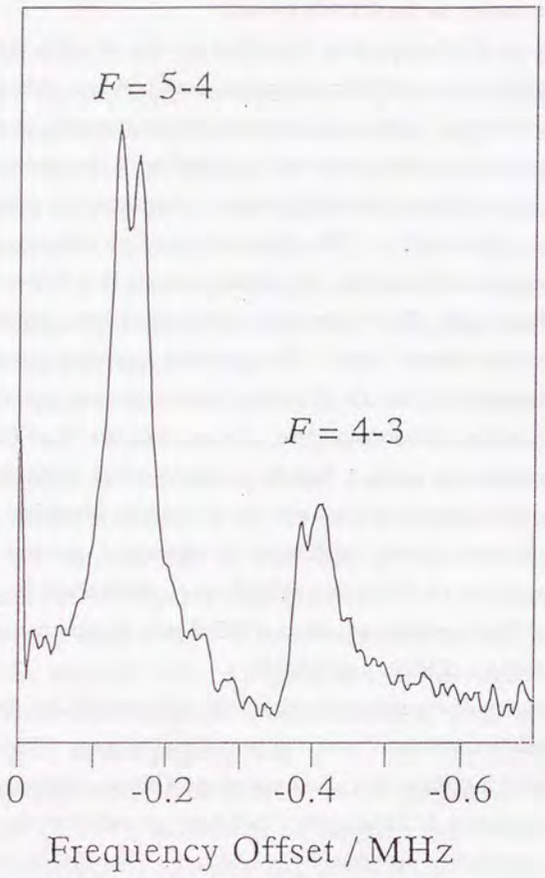

Figure 1 The observed spectrum of HC_4O for the two hyperfine components of the $J = 9/2 - 7/2$ transition in $N_{KaKc} = 5_{05} - 4_{04}$. The abscissa corresponds to the offset from the center frequency at 22 782.391 MHz. The lines were observed in the lower sideband (the center frequencies of the lines were 22 782.212, and 22 781.903 MHz). The spectrum was obtained after 100 shots of accumulation with a repetition rate at 5 Hz.

resolved for the transition.

3. ANALYSIS

Since the HC_4O radical has a nonlinear molecular structure in the $^2A''$ electronic ground state, as will be discussed in a following section, the Hamiltonian appropriate to HC_4O is given as

$$H = H_{rot} + H_{sr} + H_{hfs}, \tag{1}$$

where the first, the second, and the third terms correspond to the rotation of the molecular frame, the spin-rotation interaction, and the hyperfine interaction due to the hydrogen or deuterium nucleus, respectively. In the present study, all the observed transitions are of the $K_a = 0$ levels, and the asymmetry of the molecule is small enough that the $K_a = 0$ ladder is well isolated from other $K_a = 1$ ladders in energy. Therefore, a reduced form of the Hamiltonian, which has the same form as that for a linear molecule in a $^2\Sigma$ state,[19] was used instead of using a complete form for a doublet asymmetric top radical. The rotational and spin-rotation interaction terms are then expressed as

$$H_{rot} = B_{eff}N^4 - D_{eff}N^4, \tag{2}$$

and

$$H_{sr} = \gamma_{eff}S\cdot N - D_{eff}[(S\cdot N)N^2 + N^2(S\cdot N)]/2, \tag{3}$$

where N and S are the rotational and the electron spin angular momentum operators, respectively. For the hyperfine interaction due to the hydrogen nucleus, the Fermi contact term and the dipole-dipole interaction term were considered, while for DC_4O, where the deuterium nucleus has a nuclear spin angular momentum of 1, the electric quadrupole interaction term has also been included. Therefore,

$$H_{hfs} = b_F \mathbf{I}\cdot\mathbf{S} + (6^{1/2}/3)c\, T^{(2)}_0(\mathrm{I}, \mathrm{S}) - eQq/[4\mathrm{I}(2\mathrm{I}-1)]\, T^{(2)}_0(\mathrm{I}), \quad (4)$$

where I is the nuclear spin angular momentum operator and $T^{(2)}$ represents the spherical tensor operator of the second rank. The coupling constants, b_F and c, are defined as follows,

$$b_F = (8\pi/3) g_s g_I \beta\beta_N |\Phi(0)|^2, \quad (5)$$

and

$$c = (3/2) g_s g_I \beta\beta_N \langle(3\cos\theta - 1)/r^3\rangle, \quad (6)$$

where $|\Phi(0)|^2$ is the unpaired electron density at the position of the hydrogen nucleus, and r and θ are the polar coordinates of the unpaired electron in a coordinate system with the origin at the hydrogen nucleus and the internal axes parallel to the principal axes.

Since the spin-rotation interaction is much smaller than the rotational energy, Hund's case (b) coupling scheme is appropriate to the present case. The Hund's case $(b)_{pJ}$ basis functions, $|NSJIFM_F\rangle$, were used to calculate the matrix elements.[19] Energy levels were evaluated by diagonalizing each F-block matrix. The molecular constants of the three isotopomers were determined by least-squares fitting procedures, as listed in Table IV. Standard deviations of the fittings are 5, 9, and 5 kHz for HC_4O, DC_4O, and $HC_4{}^{18}O$, respectively, all of which are well within the experimental accuracy of the measurements. It should be noted that the constants thus determined are effective ones since HC_4O is treated as a linear molecule in the present analysis. The ratios of the hyperfine coupling constants for DC_4O and HC_4O determined in this study are consistent with the ratio of the nuclear magnetic moment of hydrogen and deuterium. It is also reasonable that the hyperfine coupling constants of $HC_4{}^{18}O$ agree with those of HC_4O within their uncertainties.

Table IV. Molecular constants for HC_4O, DC_4O, and $HC_4{}^{18}O$ (in MHz).[a]

	HC_4O	DC_4O	$HC_4{}^{18}O$
B_{eff}	2279.914 5(4)	2153.354 6(10)	2174.4455(5)
$D_{eff}\times10^3$	0.655(10)	0.52(4)	0.532(12)
γ_{eff}	33.795(4)	32.044(9)	32.749(9)
$\gamma_{Deff}\times10^3$	5.10(9)	4.3(3)	3.64(14)
b_F	-32.116(7)	-4.94(3)	-32.12(5)
c	24.219(14)	3.83(2)	24.31(4)
eQq			0.21(2)

[a]Numbers in parentheses represents one standard deviation of the least-squares fitting in unit of the last significant digits.

At an early stage of the study, where a weak hyperfine component with $\Delta F \neq \Delta J$ was not included in the analysis, there remained ambiguity concerning the sign of the Fermi contact coupling constant, b_F. An extensive search was made for observing the component, $F'' = 1$, $J'' = 1/2 \leftarrow F' = 1$, $J' = 3/2$ for the $N = 2 - 1$ rotational transition. Inclusion of this component to the analysis removed the ambiguity: the sign of b_F was determined to be negative.

4. DISCUSSION

All the observed transitions are of the $K_a = 0$ levels and have been fitted to the effective Hamiltonian for a linear molecule as has been given in eqs. (2)-(4). The rotational constant B_{eff} and the centrifugal distortion constant D_{eff} should be regarded as effective parameters, of which we have to take care for interpretation. The determined D_{eff} constant for HC_4O is too large for a linear molecule, when it is compared with those of molecules known to have linear structures, as shown in Table V. The value normalized to the rotational constant, D/B^3, of HC_4O is more than 3 times larger than those of other linear molecules listed in Table V. The large D_{eff} constant for HC_4O indicates that this molecule is nonlinear or quasilinear. Contribution of the nonlinearity to D_{eff} can be estimated as follows.

The rotational energy of a near prolate asymmetric top molecule can be expanded in a power series using Wang's asymmetry parameter, b_p, as [20]

$$E_{rot} = BN(N+1) + [A - (B+C)/2]\, W(b_p) , \tag{7}$$

where

$$W(b_p) = C_n(N,K)\, b_p^n , \tag{8}$$

and

$$b_p = (B - C)/(2A - B - C) . \tag{9}$$

Table V. Rotational and centrifugal distortion constants of HC_4O and other linear molecules.

	HC_4O[a]	C_3S[b]	C_4Si[c]	HC_5N[d]
B/MHz	2280	2890	1534	1331
D/kHz	0.66	0.22	0.058	0.026
$D/B^3/10^{-15}$ MHz^{-2}	55.7	9.1	16.1	11.0

[a]This work.

[b]S. Yamamoto, S. Saito, K. Kawaguchi, N. Kaifu, H. Suzuki, and M. Ohishi, Astrophys. J. 317, L119 (1987).

[c]M. Ohishi, N. Kaifu, K. Kawaguchi, A. Murakami, S. Saito, S. Yamamoto, S. Ishikawa, Y. Fujita, Y. Shiratori, and W. M. Irvine, Astrophys. J. 345, L83 (1989).

[d]A. J. Alexander, H. W. Kroto, and D. R. M. Walton, J. Mol. Spectrosc. 62, 175 (1976).

The explicit form for the $C_n(N,K)$ coefficients is given in Ref. 20. The second term in eq. (7) has a term proportional to $N^2(N+1)^2$, arising from the finite asymmetry of the molecule, *i.e.*, non-zero B-C. The term, here denoted as D_{asym}, is thus given as,

$$D_{asym} = (B - C)b_p/16 , \tag{10}$$

where terms higher than the second power of b_p are neglected. Considering the fact that $A >> B \approx C$, and using the planarity condition, $1/C = 1/A + 1/B$, the contribution of the asymmetry to the effective centrifugal distortion constant can be evaluated as,

$$D_{asym} \approx B^4/32A^3 . \tag{11}$$

D_{eff} determined from the experimental data contains a contribution of the true centrifugal distortion, D_N. Therefore,

$$D_{eff} = D_{asym} + D_N . \tag{12}$$

The latter term arises from the nonrigidity of the molecule and is primarily related to the harmonic force field and the molecular structure.

Since we have no data on the value of D_N for HC_4O, the centrifugal distortion constant of butatrienone, H_2C_4O, ($D_J = 0.241 \pm 0.010$ kHz)[21] was used as a reference value for D_N. This value could differ from the true value at most 50%, judging from a comparison of the centrifugal distortion constants for the shorter HC_nO radicals and those for the related H_2C_nO molecules, as listed in Table VI. Therefore, D_{asym} is estimated to be 0.42 ± 0.12 kHz from the observed D_{eff} constant considering the possible error for D_N. If it is assumed that the CCCCO framework of HC_4O is linear and only the hydrogen atom is out of linearity, the H-C-C angle of 90° gives the minimum rotational constant A of 440 GHz. This A constant leads to D_{asym} of 0.009 kHz from eq. (11), which is too

Table VI. Centrifugal distortion constants of HC_nO and H_2C_nO (in kHz).

n	1	2	3	4
$D_N(HC_nO)$	118.15(17)[a]	3.861(21)[b]	1.090 32(74)[c]	
$D_J(H_2C_nO)$	75.30(7)[d]	3.94(33)[e]	1.507(26)[f]	0.241(10)[g]
Ratio	1.57	0.98	0.74	

[a]Reference 11.

[b]Reference 14.

[c]Reference 16.

[d]R. Cornet and G. Winneswiser, J. Mol. Spectrosc. 80, 438 (1980).

[e]J. W. C. Johns, J. M. R. Stone, and G. Winneswiser, J. Mol. Spectrosc. 42, 523 (1972).

[f]R. D. Brown, R. Champion, P. S. Elmes, and P. D. Godfrey, J. Am. Chem. Soc. 107, 4109 (1985).

[g] Reference 21.

small compared with the value derived from the observed D_{eff}. Therefore, it is concluded that the HC_4O radical has a nonlinear CCCCO framework. If D_{asym} estimated above is used, the A constant is calculated to be 126±15 GHz from eq. (11). This value could be compared with that of HC_3O, 261 GHz, which has been reported to have a bent carbon-chain framework.[16] If the rotational constant A is ~120 GHz, the population of the $K_a = 1$ levels should be 1/20 of that for the $K_a = 0$ levels under the present experimental condition, where the rotational temperature is estimated to be 2 K. Such a small fraction is consistent with the fact that transitions attributable to $K_a \geq 1$ levels could not be observed.

The molecular constants for the two isotopomers, DC_4O and $HC_4{}^{18}O$, have also been determined in the present study, which give additional data on the molecular structure of this radical. The substitution coordinates, z_s, of the terminal hydrogen and oxygen atoms can be deduced using Kraitchman's equation.22 The determined values are: $z_s(H) = 3.626$ and $z_s(O) = 2.352$. The sum, $z_s(H) + z_s(O) = 5.978$, corresponds to the projection of the total length of the molecule onto the a-inertial axis. This value is 95-100 % of the estimated total length of the molecule in the linear configuration, whose bond lengths are taken from those of the related molecules as HC_nO (n=1-3) and H_2C_nO (n=1-4):[14,23-25] 1.06 ≤ r(CH) ≤ 1.12, 1.27 ≤ r(CC) ≤ 1.32, and 1.14 ≤ r(CO) ≤ 1.21, in .

All the shorter members of the HC_nO series (n = 1-3) are subjected to a strong Renner-Teller interaction, which causes the nonlinear and planar geometry for the most stable configuration in the electronic ground state. Symmetry of the ground state for species with n = 1, 2, 3, have been determined to be $^2A'$, $^2A''$, $^2A'$, respectively.[2,6,14,23] This symmetry alternation for odd/even n can be explained by simple consideration of the highest occupied molecular orbital (HOMO) of the radicals, as follows.

In linear configuration, HOMO's of the HC_nO series are π -orbitals, which consist primarily of $2p$ atomic orbitals of carbon and oxygen. Since the total number of the π-electrons is $2n+3$, the HOMO is occupied by one electron for molecules with odd n, resulting in a $^2\Pi_r$ electronic state, while $^2\Pi_i$ results from

the HOMO occupied by three electrons for those with even n. As the molecule becomes bent keeping its planarity through the vibronic interaction, the degeneracy of the π-orbital is removed, yielding two nondegenerate orbitals with a' and a" symmetries. The former is lower in energy because it can be stabilized by mixing with π-orbitals, which lies in the molecular plane. For the species with odd n, only the lower a' orbital is occupied by one electron, leading to the $^2A'$ ground electronic state. The a' orbital is filled with two electrons and the higher a" orbital comes to be occupied by one electron for those with even n, whose ground state belongs to $^2A''$ in turn.

The present study has shown that the rotational transitions of HC_4O in the ground vibronic state have been satisfactorily fitted with the Hamiltonian without the spin-orbit interaction. This fact clearly indicates that the orbital angular momentum in the radical is completely quenched by the Renner-Teller interaction, resulting in a bent molecular structure in the electronic ground state. According to the argument mentioned above, the ground state of HC_4O belongs to $^2A''$, if the molecule has a planar structure as are the cases of the shorter members of the HC_nO series (n=1-3). The planarity for n = 4, however, is less certain, since lack of the observation of $K_a \geq 1$ levels prevents determination of the complete set of the rotational constants.

The energy gap between the ground state and its counterpart of the Renner-Teller pair has been derived to be 9300 cm^{-1} for HCO by the measurement of the visible transition between the two electronic states.[26] For HCCO and HC_3O, even though no direct experimental data on the excited electronic states has been reported, the energy gaps between the Renner-Teller pair have been estimated from the spin-rotation coupling constant, ε_{aa}, which is dominated by the second-order effect of the spin-orbit interaction between the two electronic states. Values thus estimated are substantially smaller than that of HCO: 540 cm^{-1} for HCCO[14] and 2560 cm^{-1} for HC_3O,[16] where the spin-orbit coupling constants are estimated from that of the carbon atom. In Ref. 14, a wider range has been given for the energy gap for HCCO, considering a possible contribution of the spin-orbit coupling constant of the oxygen atom. However,

recent study proved that most of the unpaired-electron density is on the carbon atom adjacent to the hydrogen[2] and the lower limit, 540 cm^{-1}, is more probable. To examine the tendency of the vibronic interaction of the HC_nO series and compare them with other carbon-chain radicals, data on the energy gap in HC_4O is highly desired. Unfortunately, no such information can be derived in the present study due to the lack of the data on $K_a \geq 1$ levels.

Concerning the electron configuration of HC_4O, we have to address a small but non-negligible possibility that a non-bonding σ-orbital lies above the π-orbital and is the unpaired electron orbital in HC_4O. This electron configuration would cause completely quenched orbital angular momentum without any vibronic interaction, which yields a spectral pattern similar to that observed in the present study. If this is the case, the unpaired electron in the σ-orbital could contact directly to the hydrogen nucleus, making the Fermi contact constant, b_F, to have a substantially large positive value. This is in contradiction to the present experimental observation that $b_F < 0$ and thus the possibility is definitely ruled out.

The negative Fermi contact constant originates from the spin-polarization effect of the unpaired electron in the π-orbital of the carbon atom adjacent to the hydrogen atom (here, denoted as C_1).[27] The value of b_F is proportional to the spin density ρ on the C_1 atom. Using the McConnell's factor of -63 MHz,[28] the spin density on C_1 is estimated to be 51 %. In Table VII, the values of b_F and ρ are compared with those of HCCO, which is also a π-radical in the $^2A''$ electronic ground state. Although the spin density of HC_4O is somewhat smaller than that of HCCO (86%), indicating larger delocalization of the unpaired electron among the heavy-atom framework, about one half of the spin density still remains on C_1.

Unlike the isotropic Fermi contact term, the dipolar interaction constant has the angular dependence on the spatial distribution of the unpaired electron viewed from the hydrogen nucleus, as defined in eq. (6). Since the unpaired electron located on the C_1 atom mainly contributes to the constant, the value of c becomes larger when the C-H bond lies closer to the *a*-principal axis. As seen in Table VII, the dipolar coupling constant for HC_4O is much larger than that of

Table VII. Hyperfine coupling constants of HCCO and HC_4O.

	b_F /MHz	ρ[a]/%	c /MHz	c/ρ /MHz
HCCO[b]	-54.030(5)	86 %	16.03(2)	18.6
HC_4O	-32.116(7)	51 %	24.219(14)	47.5

[a]Spin density on the carbon atom adjacent to the hydrogen calculated by using McConnell's relation.[28]

[b]Reference 2.

HCCO when normalized by the spin densities. This fact implies that the angle between the C-H bond and the *a*-principal axis in HC_4O is much smaller than that in HCCO, 40°.[14] By adopting the same procedure applied to the previous study of HCCO,[2] the angle for HC_4O was estimated to be about 20° . As has been shown above, several data on the molecular structure of the HC_4O radical have been obtained from the present FTMW measurement. One of the most interesting questions remained is the bond angles in the heavy-atom framework, which may be sensitive parameters for describing the vibronic interactions in the HC_nO series. For the HCCO radical, the results of SMMW spectroscopy have determined a planar and bent HCC structure, but no experimental evidence has been observed for a nonlinear CCO framework.[14] In contrast, the heavy-atom framework of HC_3O has been reported to be nonlinear.[17] The molecule is bent at the carbon atom adjacent to the oxygen with the almost linear H-C-C structure. This fact implies that the molecular structure can be represented essentially as H-C≡C-˙C=O rather than H-˙C=C=C=O in a simple valence bond picture for HC_3O. If HC_4O has such structure that the molecule is bent only at the center of its carbon chain by analogy with that of HC_3O, the estimated A constant of −120 GHz gives the C_2-C_3-C_4 angle of 150° . This structure gives the value of z_s(H) + z_s(O) 3 % shorter than the total molecular length, which is within the range of the experimentally determined value. The angle between the C-H bond and the *a*-axis is −15° , when HCC is assumed to be linear, which is close to the value estimated from the dipolar hyperfine constant. Thus, this bent carbon-chain framework can be considered as one of the plausible geometries for HC_4O. Of course the present experimental data is insufficient for the conclusive determination of the molecular structure, and further investigations, especially concerning the ^{13}C-substituted species, are required. If data on $K_a \geq 1$ transitions are available in experimental conditions with higher rotational temperature and/or with higher detection sensitivity, they would be also crucial for structural determination.

5. CONCLUSION

The first spectroscopic characterization of a new carbon-chain radical, HC_4O, has been made by FTMW spectroscopy. The molecule is a slightly bent doublet free radical, in which the CCCCO framework should be nonlinear judging from the observed effective centrifugal distortion constant. The spin density and the geometry around the H-C bond have been discussed on the basis of the determined hyperfine coupling constants for the hydrogen nucleus. Similarities to the shorter members of the HC_nO series have been confirmed for the ground state electron configuration, which corresponds to the lower component of the degenerated pair split by the Renner-Teller interaction.

References

[1]Y. Endo and Y. Ohshima, J. Chem. Phys. 98, 6618 (1993).

[2]Y. Ohshima and Y. Endo, J. Mol. Spectrosc. 159, 458 (1993).

[3]Y. Ohshima and Y. Endo, J. Mol. Spectrosc. 153, 627 (1992).

[4]Y. Hirahara, Y. Ohshima, and Y. Endo, Astrophys. J. 408, L113 (1993).

[5]Y. Kasai, K. Obi, Y. Ohshima, Y. Hirahara, Y. Endo, K. Kawaguchi, and A. Murakami, Astrophys. J. 410, L45 (1993).

[6]A. G. Gaydon, "The Spectroscopy of Flames" (Chapman & Hall, 1957).

[7]J. V. Michael and A. F. Wagner, J. Phys. Chem. 94, 2453 (1990).

[8]L. E. Snyder, M. S. Schenewerk, and J. M. Hollis, Astrophys. J. 298, 360 (1985).

[9]B. E. Turner and T. J. Sears, Astrophys. J. 340, 900 (1989).

[10]D. A. Ramsay, J. Chem. Phys. 21, 960 (1953).

[11]G. A. Blake, K. V. L. N. Sastry, and F. C. De Lucia, J. Chem. Phys. 80, 95 (1984).

[12]G. W. Adamson, X. Zhao, and R. W. Field, J. Mol. Spectrosc. 160, 11 (1993).

[13]I. C. Bowater, J. M. Brown, and A. Carrington, Proc. R. Soc. Lond. A333, 265 (1973).

[14]Y. Endo and E. Hirota, J. Chem. Phys. 86, 4319 (1987).

[15]A. L. Cooksy, J. K. G. Watson, C. A.Gottlieb, and P. Thaddeus, Astrophys. J. 386, L27 (1992).

[16]A. L. Cooksy, J. K. G. Watson, C. A. Gottlieb, and P. Thaddeus, J. Mol. Spectrosc. 153, 610 (1992).

[17]A. L. Cooksy, J. K. G. Watson, C. A. Gottlieb, and P. Thaddeus, J. Chem. Phys. 101, 178 (1994).

[18]T. J. Balle and W. H. Flygare, Rev. Sci. Instrum 52, 33 (1981).

[19]A. Carrington, D. H. Levy, and T. A. Miller, Adv. Chem. Phys. 18, 149 (1970).

[20]W. Gordy and R. L. Cook, "Microwave Molecular Spectra" (John Wiley & Sons, 1956).

[21]R. D. Brown, R. F. C. Brown, F. W. Eastwood, P. D. Godfrey, and D. McNaughton, J. Am. Chem. Soc. 101, 4705 (1979).

[22]J. Kraitchman, J. Am. Phys. 21, 17 (1953).

[23]T. Oka, J. Phys. Soc. Jpn. 15, 2274 (1960).

[24]Z. A. Tomasic and G. E. Scuseria, J. Phys. Chem. 95, 6905 (1991).

[25]H. R. Johnson and M. W. P. Strandberg, J. Phys. Chem. 20, 687 (1952).

[26]J. W. C. Johns, S. H. Priddle, and D. A. Ramsay, Discuss. Fara. Soc. 35, 90 (1963).

[27]H. M. McConnell, J. Chem. Phys. 24, 754 (1956).

[28]H. M. McConnell and D. B. Chesnut, J. Chem. Phys. 28, 107 (1958).

Appendix

Table I. Observed transition frequencies of HC_4O (in MHz).

N'	J'	F'	N"	J"	F"	obs.	obs.-calc.
2	3/2	2	1	1/2	1	9105.304	-.008
2	3/2	1	1	1/2	0	9106.741	-.002
2	3/2	1	1	1/2	1	9088.062	.001
2	5/2	3	1	3/2	2	9136.211	-.003
2	5/2	2	1	3/2	1	9133.958	.006
2	5/2	2	1	3/2	2	9160.307	.002
3	5/2	3	2	3/2	2	13663.741	.001
3	5/2	2	2	3/2	1	13663.252	.004
3	7/2	4	2	5/2	3	13696.177	-.006
3	7/2	3	2	5/2	2	13695.076	-.001
4	7/2	4	3	5/2	3	18222.881	.002
4	7/2	3	3	5/2	2	18222.470	.007
4	9/2	5	3	7/2	4	18256.034	-.002
4	9/2	4	3	7/2	3	18255.395	-.001
5	9/2	5	4	7/2	4	22782.212	-.001
5	9/2	4	4	7/2	3	22781.903	-.004
5	11/2	6	4	9/2	5	22815.812	.004
5	11/2	5	4	9/2	4	22815.395	-.001

Table II. Observed transition frequencies of DC_4O (in MHz).

N'	J'	F'	N"	J"	F"	obs.	obs.-calc.
2	3/2	1/2	1	1/2	1/2	8596.980	.001
2	3/2	3/2	1	1/2	1/2	8599.243	.001
2	3/2	3/2	1	1/2	3/2	8594.345	.001
2	3/2	5/2	1	1/2	3/2	8597.989	-.004
2	5/2	5/2	1	3/2	3/2	8628.686	-.002
2	5/2	7/2	1	3/2	5/2	8629.334	.002
3	5/2	3/2	2	3/2	1/2	12904.266[a]	.015
3	5/2	5/2	2	3/2	3/2	12904.507	.000
3	5/2	7/2	2	3/2	5/2	12904.266[a]	.001
3	7/2	5/2	2	5/2	3/2	12935.883	-.006
3	7/2	7/2	2	5/2	5/2	12935.806	.004
3	7/2	9/2	2	5/2	7/2	12936.082	.001
4	7/2	5/2	3	5/2	3/2	17210.676	-.009
4	7/2	7/2	3	5/2	5/2	17210.825	-.005
4	7/2	9/2	3	5/2	7/2	17210.740	.013
4	9/2	7/2	3	7/2	5/2	17242.691	.016
4	9/2	9/2	3	7/2	7/2	17242.615	-.010
4	9/2	11/2	3	7/2	9/2	17242.774	-.006

[a]Blended.

Table III. Observed transition frequencies of $HC_4{}^{18}O$ (in MHz).

N'	J'	F'	N"	J"	F"	obs.	obs.-calc.
2	3/2	2	1	1/2	1	8683.975	-.006
2	3/2	1	1	1/2	0	8685.420	-.000
2	5/2	3	1	3/2	2	8713.815	.004
2	5/2	2	1	3/2	1	8711.543	.002
3	5/2	3	2	3/2	2	13031.498	.003
3	5/2	2	2	3/2	1	13030.999	.003
3	7/2	4	2	5/2	3	13062.842	.000
3	7/2	3	2	5/2	2	13061.723	-.003
4	7/2	4	3	5/2	3	17379.731	.003
4	7/2	3	3	5/2	2	17379.308	.002
4	9/2	5	3	7/2	4	17411.763	.003
4	9/2	4	3	7/2	3	17411.103	-.011
5	9/2	5	4	7/2	4	21728.170	-.002
5	9/2	4	4	7/2	3	21727.860	-.002
5	11/2	6	4	9/2	5	21760.610	.004
5	11/2	5	4	9/2	4	21760.190	.002

Chapter IV

Laser induced fluorescence spectroscopy of the $\tilde{C}\,^2\Sigma^+$-$\tilde{X}\,^2\Pi_{1/2}$ band system of the CCN radical in a supersonic jet

Abstract

Laser induced fluorescence (LIF) spectra of vibronic bands in the $\tilde{C}\,^2\Sigma^+ - \tilde{X}\,^2\Pi_r$ system of the CCN radical have been observed in a supersonic jet. A pulsed-discharge nozzle (PDN) has been developed for an efficient method to produce short-lived species in the jet. The observed vibronic bands are $\tilde{C}\,^2\Sigma^+(v_1, v_2^{\ell}, v_3) - \tilde{X}\,^2\Pi_{\Omega=1/2}(0, 0, 0)$, in which $v_1 = 0, 1, 2, 3$, $v_2 = 0, 1, 2$ (ℓ=0, 2), and $v_3 = 0, 1, 2$. Vibrationally excited states of all the three normal modes in the $\tilde{C}\,^2\Sigma^+$ state were assigned including their combination bands. For all the sixteen vibronic bands observed in this study, their rotational structures have been analyzed. Thus the band origin and the rotational constants have been precisely determined for each vibronic state in the $\tilde{C}\,^2\Sigma^+$ state. Based on the determined band origins, the vibronic parameters in the $\tilde{C}\,^2\Sigma^+$ state were derived: $\omega_1 = 1903.1(11)$ cm^{-1}, $\omega_2 = 469.88(38)$ cm^{-1}, $\omega_3 = 1256.6(40)$ cm^{-1}, $T_e = 24627.01(20)$ cm^{-1}, $g_{22} = 0.86(11)$ cm^{-1}. Very weak bands observed were assigned to vibronically induced bands. Combined with the data on hot bands reported by Merer and Travis, the vibronic structure of the $\tilde{X}\,^2\Pi_r$ ($0v_20$) and $\tilde{A}\,^2\Delta(0v_20)$ were derived.

1. Introduction

The first spectroscopic study of the CCN radical was UV absorption spectroscopy with flash photolysis by Merer and Travis.[1] They observed absorption spectra of the $\tilde{A}\,^2\Delta$-$\tilde{X}\,^2\Pi_r$, $\tilde{B}\,^2\Sigma^-$-$\tilde{X}\,^2\Pi_r$, and $\tilde{C}\,^2\Sigma^+$-$\tilde{X}\,^2\Pi_r$ electronic transitions including hot bands. Analyses of the rotational structures yielded the molecular parameters of these electronic states. Kakimoto and Kasuya[2] observed laser induced fluorescence spectra of the $\tilde{A}\,^2\Delta(000)$-$\tilde{X}\,^2\Pi_r(000)$ band by a cw dye laser. They determined molecular constants such as the rotational constant, the spin-orbit interaction constant, the spin-rotation coupling constant, Λ-type doubling constants, and their higher order terms for the $\tilde{X}\,^2\Pi_r(000)$ with high accuracy. Quite recently, Ohshima and Endo[3] refined these molecular constants for the vibronic ground state by Fourier-transform microwave (FTMW) spectroscopy.

One of the most interesting aspects on spectroscopic study of the CCN radical is the Renner-Teller effect. It was observed in degenerate electronic states, the $\tilde{A}\,^2\Delta$ and $\tilde{X}\,^2\Pi_r$ states. Since the first spectroscopic data by Merer and Travis in 1965, many observations had been performed in order to elucidate the Renner-Teller effect in the $\tilde{A}\,^2\Delta$ and $\tilde{X}\,^2\Pi_r$ states.[2, 4-6] For the vibronic structure of the $\tilde{X}\,^2\Pi_r$ state, Hakuta and Uehara[4] excited the R(23.5) and $^sR_{21}(12.5)$ transitions in the $\tilde{A}\,^2\Delta(010)\Phi \leftarrow \tilde{X}\,^2\Pi_r$ $(010)\Delta$ vibronic band, which are resonant with one of the oscillating lines of an Ar^+ laser, and observed the emission spectra of the $\tilde{A}\,^2\Delta(010)\Phi \rightarrow \tilde{X}\,^2\Pi_r$ ($v_1v_2v_3$) with $v_2 = 1$ and 3. By using the same two rovibronic transitions as pumping processes, Braizer *et al.* [5] observed high resolution emission spectra of $\tilde{A}\,^2\Delta(010)\Phi \rightarrow \tilde{X}\,^2\Pi_r(0v_21)$ by a Fourier-transform (FT) spectrometer and determined the Renner-Teller parameters in the $\tilde{X}\,^2\Pi_r$ state. Since their observation was limited to that for v_3 excited states in the $\tilde{X}\,^2\Pi_r$ state because of a small Franck-Condon factor of the emission, their vibronic

parameters were effective assuming that the influence of the Renner-Teller effect on the υ_3 stretching mode is small. Kawaguchi *et al.*[6] observed laser induced fluorescence spectra of the $\tilde{A}\,^2\Delta(010)\Phi,\Delta$-$\tilde{X}\,^2\Pi_r(010)\Pi,_\mu\Sigma$ and the $\tilde{A}\,^2\Delta(020)\Phi$-$\tilde{X}\,^2\Pi_r$ (020)Γ sequence bands ($\Delta v=0$) with Doppler-limited resolution (0.04 cm^{-1}). They discussed the influence of the Renner-Teller effect on the rotational constants and the spin-orbit constant (*Aso*) by analyzing their highly accurate data.

The theory of the Renner-Teller effect has been established for the influence on the vibronic structures, the *Aso* constants, and the rotational constants.[7-14] The theory has been applied to spectroscopic data of mainly triatomic free radicals in $^2\Pi$ electronic states.

In the present study, the observed excited electronic state was the $\tilde{C}\,^2\Sigma^+$ state. Because the $\tilde{C}\,^2\Sigma^+$ state is not degenerate, it is not subjected by the Renner-Teller effect mentioned above. Concerning to the spectroscopic study on the $\tilde{C}\,^2\Sigma^+$ state, Merer and Travis[1] observed the (000)Σ-(000)Π, (100)Σ-(000)Π, (010)Π-(010)$\Delta,_\mu\Sigma$, (020)Δ-(020)Φ, and (110)Π-(010)$\Delta,_\mu\Sigma$ vibronic transitions in the $\tilde{C}\,^2\Sigma^+$-$\tilde{X}\,^2\Pi_r$ band. They determined the υ_1 fundamental to be 1,859.2 cm^{-1} and T_0 = 26,661.7 cm^{-1}. The ω_2 bending frequency was derived to be 465 cm^{-1} from ℓ-type doublings observed in the $\tilde{C}$ (010) state by using a simple formula derived by Nielsen,[15] in which Coriolis interaction was treated as a perturbation to the bending excited states of linear molecules. The ω_2 for the $\tilde{X}$ state was evaluated to be 325 cm^{-1} by using their tentative value for ω_2 for the $\tilde{C}$ state. Before high resolution FT spectroscopy by Brazier *et al.* in 1987, ω_2 = 325 cm^{-1} had been frequently used for analysis of the Renner Teller effect in the $\tilde{X}\,^2\Pi_r$ state. There have been no observation of the υ_3 excited state in the $\tilde{C}$ state and we have no data on the υ_3 fundamental.

The $\tilde{C}\,^2\Sigma^+$ state is the highest excited electronic state among the known electronic states of the CCN radical. Dissociation process of this

radical had been suggested in excited electronic states. In Ar matrix,[16,17] UV irradiation decreased the absorption spectra of CCN. In the gas phase, disappearance of the absorption in the $\tilde{C}$ (010)Π state has been ascribed to dissociation.[1]

In this study, an apparatus to observe LIF spectra of free radicals combined with a pulsed-discharge nozzle (PDN) has been developed. Originally the PDN has been developed in FTMW spectroscopy[18,19] as an efficient method for production of various kinds of free radicals in a supersonic jet. With the PDN, advantages not only of cooling of the rotational temperature of the species to be observed but also of producing collisionless conditions after production of unstable molecules can be taken. The former advantage enables us to observe weak vibronic bands without congestion of large number of rotational lines belonging to other strong bands. Weak transitions, especially those due to breaking down of any loose selection rules, sometimes give us new data.

In this chapter, LIF spectra of the $\tilde{C}\,^2\Sigma^+$-$\tilde{X}\,^2\Pi_r$ system of CCN observed in a supersonic jet is reported. The vibrational and rotational structures of $\tilde{C}\,^2\Sigma^+$ are analyzed for the observed sixteen vibronic states. Weak but important vibronic bands with $\Delta\ell$=1, which become observable due to vibronic interactions, could be observed. Combined with the previous spectroscopic data, the vibronic structures perturbed by the Renner-Teller interaction in the $\tilde{A}\,^2\Delta$ and $\tilde{X}\,^2\Pi_r$ are discussed based on the present experimental results.

2. Experimental

A. Setups

For exciting the CCN radical, a frequency-doubled dye laser (Spectra

Physics PDL-3) pumped by a Q-switched Nd^+ YAG laser (Spectra Physics GCR-3) with a KDP crystal was used. In scan of a range of the near-ultraviolet region from 26,000 cm^{-1} to 33,000 cm^{-1}, the DCM (EXCITON) dye has been used mainly. Linewidth (FWHM) of the near-UV radiation was ~0.12 cm^{-1}. A pulsed UV light was incident at 40 mm downstream from the PDN. A pair of convex lenses (60 mm∅, f = 90 mm and 60 mm∅, f = 120 mm) was used to focus and collect fluorescence signals. A photomultiplier tube (HAMAMATSU PHOTONICS R928) was used, and output from the photomultiplier was amplified by a pre-amplifier. The amplified signal was integrated by a boxcar gated integrator (SRS SR250), whose gate width was set to 300 nsec.

In order to calibrate the wavelength of the laser, an LIF spectrum of iodine in a hot cell heated to 200°C were simultaneously recorded. Heating was necessary because the LIF spectrum of I_2 ($\tilde{B}$ - $\tilde{X}$) around 13,000cm^{-1} were ascribed to hot bands. The LIF spectrum of I_2 were observed as wide as 20 cm^{-1} around each vibronic band of the CCN radical, while jet cooled LIF spectra of a single vibronic band of the CCN radical typically extended in a region of 10 cm^{-1}. Based on the frequencies of I_2 in reference 20, the abscissa of the LIF spectra of the CCN radical was calibrated. It was confirmed that the standard deviation of the calibration, in which about 10 resolved lines of I_2 were used as data, was within 0.03 cm^{-1} for each vibronic band. Transition frequencies of the CCN radical were determined based on thus calibrated laser frequencies.

B. Pulsed-discharge nozzle (PDN)

A pulsed-discharge nozzle (PDN), which was used as a production method of the CCN radical, is shown in Fig.1. A discharging unit with two electrodes was attached under a commercially available pulsed valve (General Valve). Pulsed high voltage of 1.5 kV with a duration of 20 μsec

Pulsed Discharge Nozzle

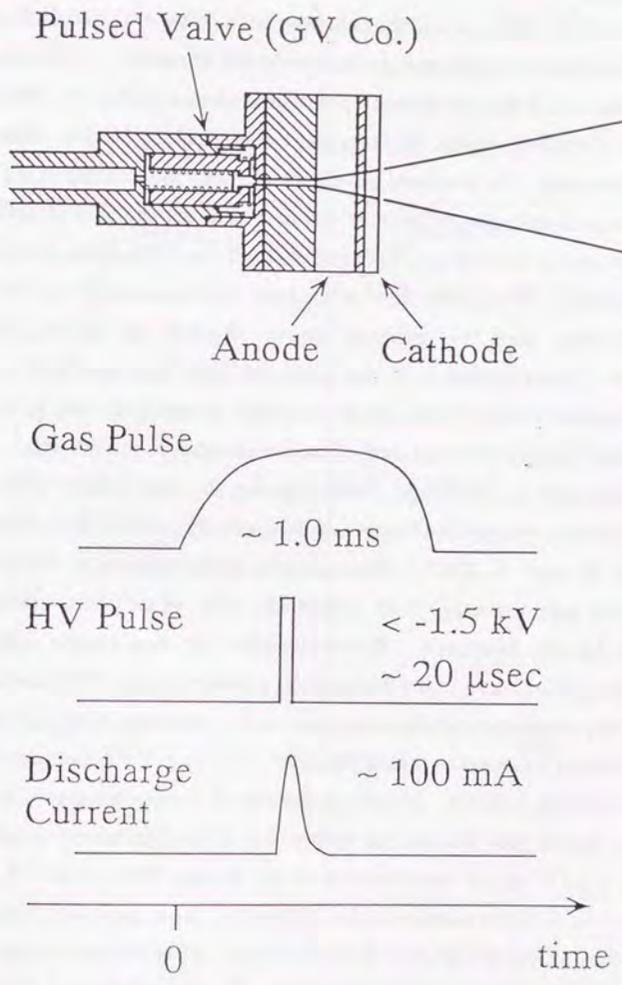

Figure 1 Pulsed-discharge nozzle. Details on this apparatus is described in Chapter II.

was applied between the two electrodes. It was preferable for efficient production of the CCN radical that negative high voltage was applied to the outer side of the electrodes and the inner side was grounded. A time profile of observed signal for one pulsed operation is shown in Fig. 2. The best signal was obtained when the laser light was incident 80 μsec after the pulsed discharge. Ar was used as carrier gas and the velocity of Ar in a supersonic jet was known to be about 500 m/sec. Since the field of vision for a photomultiplier was 40 mm downstream from the PDN, delay of 80 μsec was reasonable. If the delay time of the laser shot was changed by 10 μsec earlier or later than the optimized timing, the LIF signal was rapidly decreased. Direct incidence of this scattered light from the PDN to the photomultiplier was avoided as much as possible by using the pair of convex lenses and irises placed in the path of the fluorescence to the detector.

Although scattered light emitted during the high voltage of 20 μsec was very strong, the scattered light were temporarily distinguished from LIF signal as is seen in Fig.2. More serious noise disturbing the actual observation was emission from metastable Ar*, which were efficiently produced by the discharge. The metastable Ar* has longer radiative lifetime than 100 μsec, and the free radicals produced in the PDN flew to the field of vision together with the metastable Ar*. Although adequate sharp-cut glass filters was used to reduce the emission from Ar*, the emission could not be completely reduced. In order to subtract this noise, the second boxcar integrator whose gate was set just before that of the first boxcar integrator detecting the LIF signal was used to subtract the base fluctuation. A long-term fluctuation of the baseline in the LIF spectra due to a gradual change of the discharging conditions, was fairly flattened. This subtraction was not effective for obtaining reliable intensities of rotational lines in the LIF spectra. Fluctuation of the fluorescence was due to that of the laser pulse and that of the production efficiency by the PDN, which were 10 % and 100% for each pulse, respectively. To keep stable discharge for each pulse

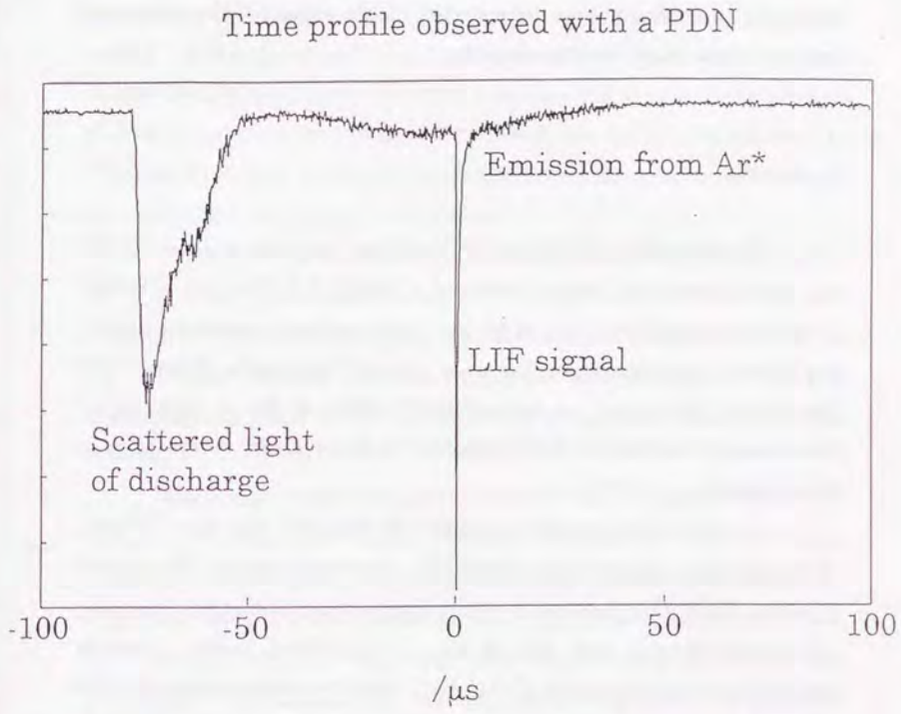

Figure 2 Output from the photomultiplier observing laser induced fluorescence signal of the CCN radical produced by the pulsed-discharge nozzle. LIF signal of the CCN radical was detected together with emission from the metastable Ar*.

was a crucial condition to obtain reliable rotational lineshape and line strength in the LIF spectra.

The sample to be discharged was 0.1 % methylecyanide (CH_3CN) diluted in Ar. When He or Ne was used as a carrier gas, to keep stable discharge was difficult even by applying higher voltage. The stagnation pressure to the PDN was kept at 4 atm.

3. Results

The range from 26,600 cm^{-1} to 33,000 cm^{-1} was scanned. At 26,660 cm^{-1} and 28,540 cm^{-1}, strong bands of $\tilde{C}\,(000)\Sigma$-$\tilde{X}\,(000)\Pi$ and $\tilde{C}\,(100)\Sigma$-$\tilde{X}\,(000)\Pi$ of the CCN radical, which had been previously reported by Merer and Travis[1], were observed. Two more vibronic bands were observed with intervals of 1,900 cm^{-1} as succeeding members of the υ_1 progression. Intensities of the bands of the progression bands gradually decreased as v_1 was increased.

At 27,140 cm^{-1}, which was higher by 460 cm^{-1} than the $\tilde{C}\,(000)\Sigma$-$\tilde{X}\,(000)\Pi$ band, a vibronic band which was ~1/100 times weaker than that of $\tilde{C}\,(000)\Sigma$-$\tilde{X}\,(000)\Pi$ was observed. The rotational structure of this band was apparently different from that of the υ_1 progression bands. Another vibronic band was observed at 27,610 cm^{-1}, which was further higher by 460 cm^{-1} than 27,140 cm^{-1}. This band was 1/20 times as weak as the $\tilde{C}\,(000)\Sigma$-$\tilde{X}\,(000)\Pi$ band. The rotational structure was somewhat broader and it had more rotational lines than the $\tilde{C}\,(000)\Sigma$-$\tilde{X}\,(000)\Pi$ band and the 27,140 cm^{-1} band. They were assigned to the υ_2 bending progression, that is, the 27,140 cm^{-1} band and the 27,610 cm^{-1} band were assigned to $\tilde{C}\,(010)\Pi$-$\tilde{X}\,(000)\Pi$ and $\tilde{C}\,(020)\Sigma,\Delta$-$\tilde{X}\,(000)\Pi$, respectively. In Fig. 3(a)-(c), three different types of rotational structures observed in the present study are shown. Apparent

differences of the rotational structures are seen there. Three different rotational structures will be analyzed and discussed in the following section. At 27,900 cm^{-1}, which was higher by ~1,200 cm^{-1} than the $\tilde{C}\,(000)\Sigma$-$\tilde{X}\,(000)\Pi$ band, a vibronic band whose carrier was considered to be the CCN radical was observed. It was overlapped by a $\Delta v = -1$ sequence band of the CN radical. Although the rotational structure was partially masked by strong lines of the CN radical, the rotational structure was seen to be the same as that of υ_1 progression. This vibronic band was tentatively assigned to $\tilde{C}\,(001)\Sigma$-$\tilde{X}\,(000)\Pi$. As a next member of the υ_3 progression, we observed the $\tilde{C}\,(002)\Sigma$-$\tilde{X}\,(000)\Pi$ band at 29,140 cm^{-1}.

From these results, the vibrational frequencies of the CCN radical in the $\tilde{C}\,^2\Sigma^+$ state were estimated as ω_1 = ~1,900 cm^{-1}, ω_2 = ~470 cm^{-1} and ω_3 = ~1,250 cm^{-1}. Based on this estimation, observation of combination bands of the $\tilde{C}\,(v_1v_2v_3)$-$\tilde{X}\,(000)\Pi$ vibronic transitions was attempted. Finally, sixteen vibronic bands of the CCN radical including combination bands were observed.

Merer and Travis observed hot bands of the $\tilde{C}$ - $\tilde{X}$ system of the CCN radical; $\tilde{C}\,(010)\Pi$-$\tilde{X}\,(010)\Delta_{3/2,5/2}$, $\tilde{C}\,(020)\Delta$-$\tilde{X}\,(020)\Phi_{5/2,7/2}$, and $\tilde{C}\,(110)\Pi$-$\tilde{X}\,(010)\mu\Sigma$, $\Delta_{3/2,5/2}$. The strongest hot band was $\tilde{C}\,(010)\Pi$-$\tilde{X}\,(010)\Delta_{3/2,5/2}$ in their observation in a flash photolysis cell. However, in the present study, the $\tilde{C}\,(010)\Pi$-$\tilde{X}\,(010)\Delta_{3/2}$ band was 1/50 times weaker than $\tilde{C}\,(000)\Sigma$-$\tilde{X}\,(000)\Pi_{1/2}$. This means that the vibrational temperature of the CCN radical produced by the PDN was very low, at least much colder than room temperature. All the relatively strong bands were ascribed to the cold bands in our assignment, that is, the lower vibronic states were commonly the vibronic ground state, $\tilde{X}\,(000)\Pi_{1/2}$. No vibronic transitions whose lower states were $\tilde{X}\,(000)\Pi_{3/2}$ were observed.

In order to identify the carrier of the observed spectra, a sample gas of CD_3CN/Ar or C_2H_2/Ar was used. For all the preliminary assigned bands

to $\tilde{C}(v_1v_2v_3)$-$\tilde{X}(000)\Pi_{1/2}$ of the CCN radical, CD_3CN/Ar sample yielded the same spectra while they were not observed by C_2H_2/Ar. It is demonstrated that the carrier of the spectra included nitrogen atoms but not a hydrogen atom. Since low J rotational transitions were observed as is shown in Fig. 3, rough estimation of the rotational constants could be made from the jet cooled LIF spectra. Effective rotational constants under the rough estimation were 0.4 cm^{-1}, which corresponded to the rotational constant of molecules with three heavy atoms. It is not plausible that molecules with two nitrogen atoms were efficiently produced by discharge of CH_3CN. A final and conclusive identification of the carrier were obtained based on the following spectroscopic analysis for the rotational structures and the vibrational structure.

4. Analysis

4-1. Rotational analysis

Analyses of rotational structures were made for all the observed vibronic bands, where the lower states were all $\tilde{X}(000)\Pi_{1/2}$. A set of the molecular constants of the CCN radical in the $\tilde{X}(000)\Pi$ state has been determined with high accuracy.[2,3,6] The molecular constants referred in the present analysis are shown in Table I. The electronic ground state is $^2\Pi$ with the Aso constant, -40.38 cm^{-1} [3,6]. The rotational energy structure is described based on the Hund's case (a) coupling scheme. The following effective Hamiltonian for linear molecules in the $^2\Pi$ state[21,22] was adopted,

$$H = H_{rot} + H_{SO} + H_{SR} + H_{LD}. \quad (1)$$

The terms represent molecular rotation, spin-orbit interaction, spin-rotation

Table I.

Molecular constants of the CCN radical in the $\tilde{X}\,\Pi_r$ state (in cm^{-1} unit).

	$(000)\Pi$	$(010)\Delta$[b]	$(020)\Phi$[b]
$A_{eff.}$	40.379 9[a]	35.9977	30.9357
B	0.398 228[c]	0.401 249	0.404 502
γ	-37.57×10^{-4} [a]	-90.0×10^{-4}	-118.7×10^{-4}
p	10.122×10^{-4} [c]	.....	.....
q	$2.379\,1\times10^{-4}$ [a]	.....	.....

[a] Reference 2.

[b] Reference 6.

[c] Reference 3.

interaction, and Λ-type doubling, respectively. For each term, molecular constants listed in Table I were used. Using the case (a) basis function, $|\Lambda S\Sigma J\Omega M_J\rangle$, two sets of 2×2 Hamiltonian matrices were solved to obtain the rotational energies and the rotational wavefunctions in the $\tilde{X}\,^2\Pi$ state.

Since the $\tilde{C}$ state is a $^2\Sigma^+$ electronic state, the rotational Hamiltonian includes the molecular rotation and the spin-rotation interaction.

$$H = H_{rot} + H_{SR} = BN^2 + \gamma N\cdot S \qquad (2)$$

The spin-rotation interaction constant, γ, of the $\tilde{C}\,^2\Sigma^+$ state was too small to resolve the spin doubling by our laser resolution of 0.12 cm^{-1}. Therefore γ in the $\tilde{C}\,^2\Sigma^+$ state was fixed to be zero. Merer and Travis had determined the ℓ-type doubling constant, q = 0.000094 cm^{-1} from the splittings observed in high J transitions in the $\tilde{C}\,(010)\Pi$-$\tilde{X}\,(010)\Delta_{,\mu}\Sigma$ band. On the other hand, since rotationally cooled spectrum was observed where the upper rotational quantum number did not exceed 6 ($N'<6$), no ℓ-type doubling was observed. The ℓ-type doubling term was not included in the rotational Hamiltonian (2) even for the excited bending states.

Since the $\tilde{C}$ state is $^2\Sigma^+$, the rotational levels should be assigned based on the case (b) basis function, $|NKSJM_J\rangle$. In actual calculation of the intensities of the rotational transitions, the case (a) basis functions were used even for the $\tilde{C}\,^2\Sigma^+$ state because common basis functions applicable to both the upper and lower states are required for calculation of the line strength. The $^2\Sigma^+$ state corresponds to the Ω = 1/2 state in case (a), and $J = N + 1/2$ and $N - 1/2$ are degenerate when γ = 0. Non-zero vibrational angular momentum, ℓ, limits the lowest value for the rotational angular momentum N for the bending excited states in the $\tilde{C}\,^2\Sigma^+$ state. For the vibrational state with $\ell = 1$, $\tilde{C}\,(v_1 1^1 v_3)\Pi$ state, the lowest rotational level is N

= 1. For the vibrational state with $\ell = 2$, $\tilde{C}\,(v_1 2^2 v_3)\Delta$ state, the lowest rotational level is $N = 2$.

By using the above Hamiltonian and basis functions, rotational constants and band origins of the upper vibronic states were determined by a least-square method. All the observed frequencies are listed in Appendix together with the differences from the calculated values. No significant deviation from the fitting were present as long as the low J transitions in all the observed vibronic states.

(a) $\tilde{C}\,(v_1 0 v_3)\Sigma$ - $\tilde{X}\,(000)\Pi$ bands

The $\tilde{C}\,^2\Sigma^+(v_1 0 v_3)$ state has a Σ vibronic symmetry. The $\tilde{C}\,^2\Sigma^+$-$\tilde{X}\,^2\Pi_r$ band system should have a perpendicular type transition moment and the rigorous selection rule is $\Delta\Lambda = \pm 1$. All the lower rotational levels were the Ω = 1/2 state of the $\tilde{X}\,(000)\Pi$ vibronic state. The vibronic transition of this type is constituted of four branches, P_1, $P_{21}+Q_1$, R_1+Q_{21} and R_{21} in terms of the case(a) basis functions.

The rotational structures of the $\tilde{C}\,(000)\Sigma$-$\tilde{X}\,(000)\Pi$, $\tilde{C}\,(100)\Sigma$-$\tilde{X}\,(000)\Pi$, $\tilde{C}\,(200)\Sigma$-$\tilde{X}\,(000)\Pi$, and $\tilde{C}\,(300)\Sigma$-$\tilde{X}\,(000)\Pi$ were analyzed as the υ_1 progression bands. Although the $\tilde{C}\,(001)\Sigma$-$\tilde{X}\,(000)\Pi$ and $\tilde{C}\,(002)\Sigma$-$\tilde{X}\,(000)\Pi$ bands were observed, the former was partially masked by the spectrum of the CN radical and the rotational analysis for this band was not tried. As for the combination bands, the $\tilde{C}\,(101)\Sigma$-$\tilde{X}\,(000)\Pi$ and the $\tilde{C}\,(201)\Sigma$-$\tilde{X}\,(000)\Pi$ bands were observed and analyzed. They were two orders of magnitude as weak as the $\tilde{C}\,(000)\Sigma$-$\tilde{X}\,(000)\Pi$ band.

The rotational constants of the $\tilde{C}\,(000)\Sigma$-$\tilde{X}\,(000)\Pi$ and $\tilde{C}\,(100)\Sigma$-$\tilde{X}\,(000)\Pi$ bands were reported as 0.4129 cm^{-1} and 0.4094 cm^{-1} respectively, by Merer and Travis[1] from ~80 rotational transitions for each vibronic band. Although no more than 20 low J rotational transitions were observed, the determined rotational constants agreed well with theirs within one standard

deviation of the fit.

In Fig.3(a), the observed spectrum of the $\tilde{C}\,(100)\Sigma$-$\tilde{X}\,(000)\Pi$ band was shown together with a simulation as an example of the Σ-Π vibronic bands. Good agreement was obtained assuming that T_{rot} = 3 K.

(b) $\tilde{C}\,(v_1 1 v_3)\Pi$ - $\tilde{X}\,(000)\Pi$ bands

The very weak band, which had been tentatively assigned as the $\tilde{C}\,(010)\Pi$-$\tilde{X}\,(000)\Pi$ band was observed at 470 cm^{-1} above the $\tilde{C}\,(000)\Pi$-$\tilde{X}\,(000)\Pi$ band. Simulation of the rotational structure based on the parallel type transition moment agreed well with the observed spectrum. The observed spectra and the simulation are shown in Fig.3(b). In the simulation, the rotational temperature was assumed to be 3 K and the laser linewidth to be 0.12 cm^{-1}. Intensities of the rotational lines were calculated from the rotational wavefunctions obtained by the least-square fitting procedure for the observed transition frequencies. Since it was assured that the observed spectra has a parallel type transition moment and the N' = 0 rotational level was missing in the upper state, this band was finally identified as $\tilde{C}\,(010)\Pi$-$\tilde{X}\,(000)\Pi$, which was vibronically induced as will be discussed later.

The $\tilde{C}\,(110)\Pi$-$\tilde{X}\,(000)\Pi$ and $\tilde{C}\,(210)\Pi$-$\tilde{X}\,(000)\Pi$ bands were observed with higher excitation energies by 480 cm^{-1} than that for $\tilde{C}\,(100)\Sigma$-$\tilde{X}\,(000)\Pi$ and $\tilde{C}\,(200)\Sigma$-$\tilde{X}\,(000)\Pi$, respectively. Similar analysis for these bands yielded confirmation of the vibronic assignments. Their rotational structure were similar to that of the $\tilde{C}\,(010)\Pi$-$\tilde{X}\,(000)\Pi$ band, where the lowest N' of the upper states were 1 from the rotational analysis. They also borrowed intensities of the electronic transition by the vibronic interaction.

(c) $\tilde{C}\,(v_1 2 v_3)\Sigma,\Delta$ - $\tilde{X}\,(000)\Pi$ bands

If the bending mode was excited by two quanta in the $\tilde{C}\,^2\Sigma^+$

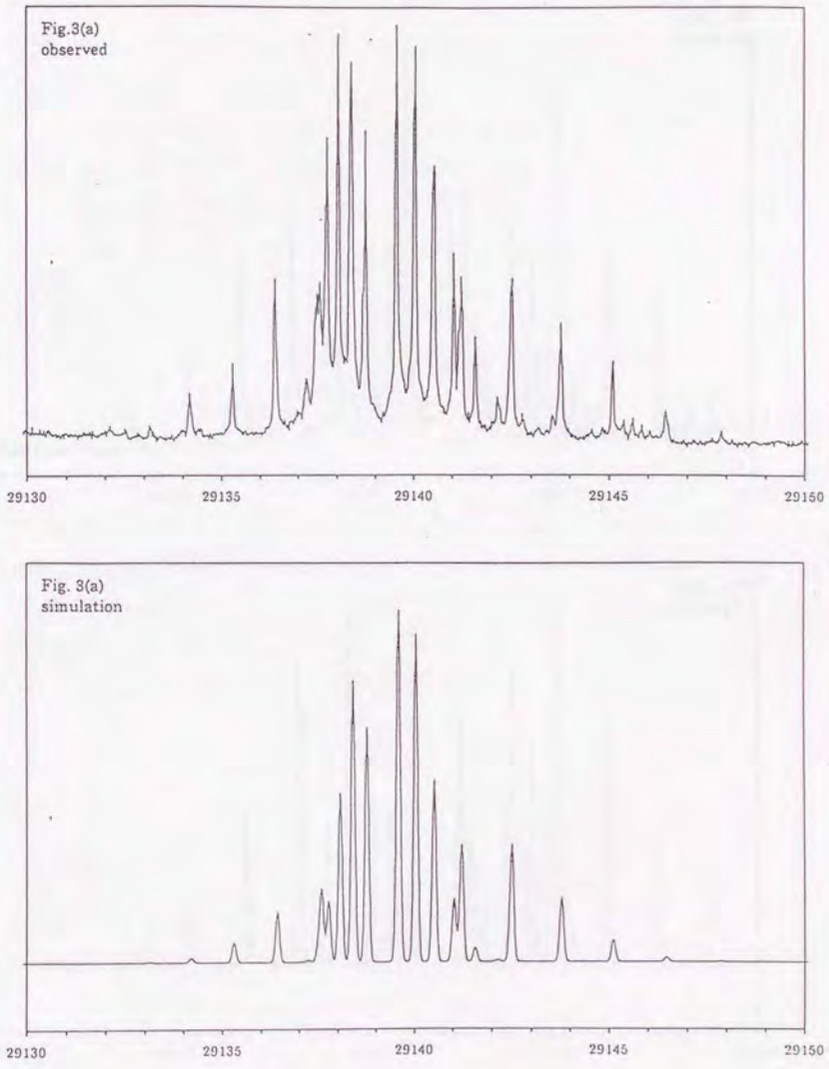

Figure 3 (a)

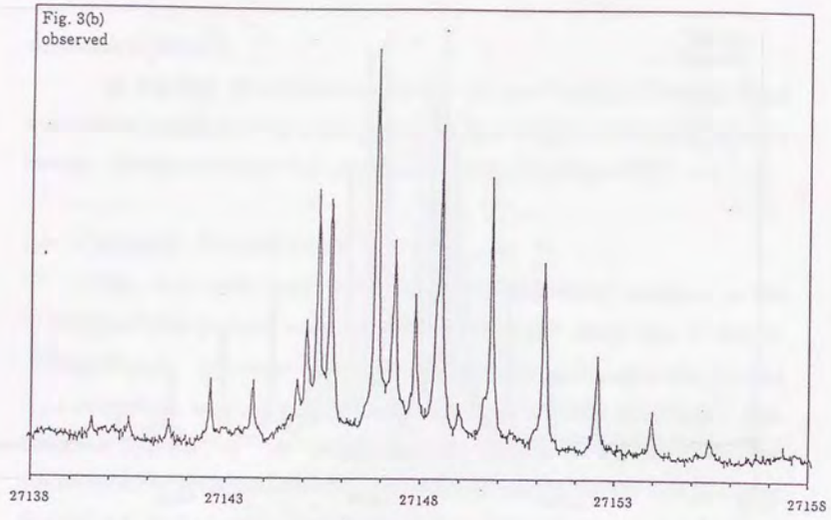

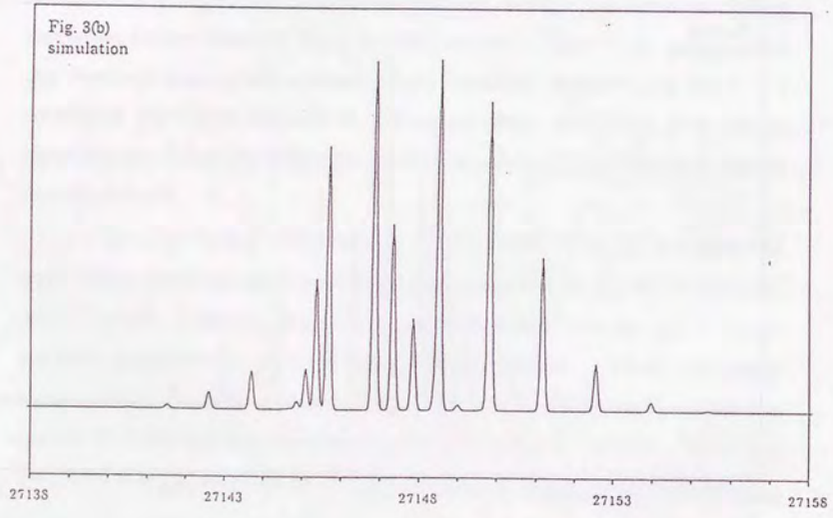

Figure 3 (b)

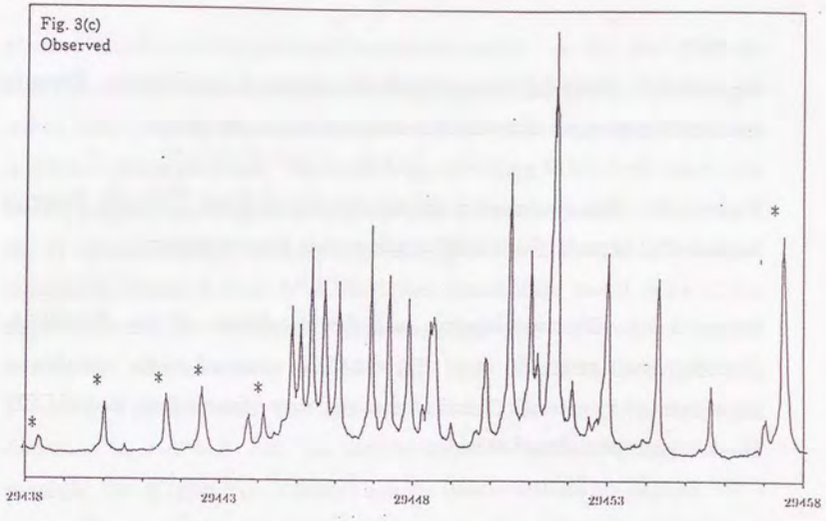

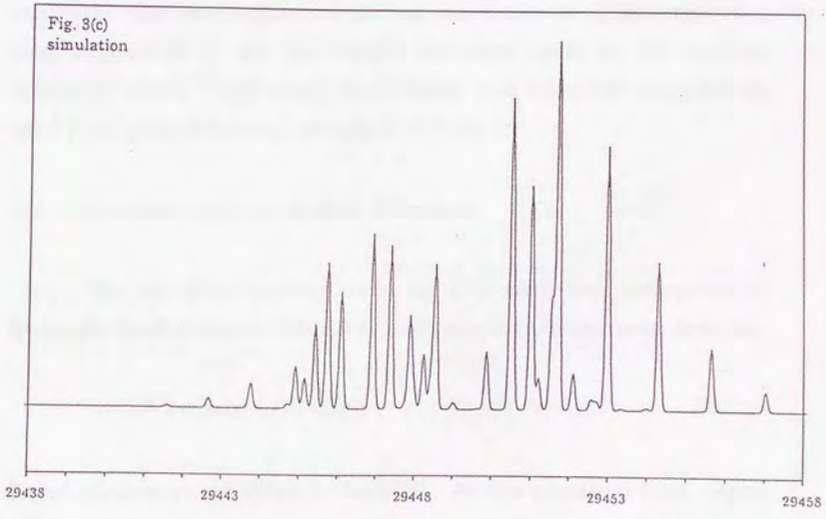

Figure 3 (c)

Figure 3 (a) Observed spectra and the simulation of the $\tilde{C}\,(100)\Sigma$- $\tilde{X}\,(000)\Pi$ band at 28,540 cm^{-1}. T_{rot} = 2.6K is assumed in the simulation.

Figure 3 (b) Observed spectra and the simulation of the $\tilde{C}\,(010)\Pi$- $\tilde{X}\,(000)\Pi$ band at 27,140 cm^{-1}. T_{rot} = 2.6K is assumed in the simulation.

Figure 3 (c) Observed spectra and the simulation of the $\tilde{C}\,(120)\Sigma,\Delta$- $\tilde{X}\,(000)\Pi$ band at 29,450 cm^{-1}. T_{rot} = 2.6K is assumed in the simulation. Lines marked by asterisk (*) have faster radiative lifetime than that of CCN. The carrier is considered to be C_2.

electronic state, resulting vibronic states are Σ and Δ. As this type of bands, $\tilde{C}\,(020)\Sigma,\Delta$- $\tilde{X}\,(000)\Pi$, $\tilde{C}\,(120)\Sigma,\Delta$- $\tilde{X}\,(000)\Pi$ and $\tilde{C}\,(220)\Sigma,\Delta$- $\tilde{X}\,(000)\Pi$, in which the Σ-Π bands were located at few cm^{-1} lower energy regions than the Δ-Π bands, were observed. Since no ℓ-type doubling in the Δ vibronic state were observed, the ℓ-type doubling constant, q, was set to zero, as well as for the Π vibronic states. From the rotational analysis for the Δ-Π vibronic transitions, whose lowest N' of the upper states were found to be 2, the rotational constants and band origins were derived. A perpendicular type transition moment was assumed for both $\tilde{C}\,(v_1 20)\Sigma$- $\tilde{X}\,(000)\Pi$ and $\tilde{C}\,(v_1 20)\Delta$- $\tilde{X}\,(000)\Pi$, and simulation based on the obtained rotational constants agreed well with the observed spectra as in Fig.3(c). As an example, the $\tilde{C}\,(120)\,\Sigma,\Delta$- $\tilde{X}\,(000)\Pi$ band is shown with its simulation.

The rotational structure of observed 16 vibronic bands in total were analyzed. The band origins and the rotational constants of the upper states were determined by the least-square procedure based on the analyses mentioned above. Vibrational band origins and rotational constants for the $\tilde{C}\,(v_1 v_2 v_3)$ vibronic states are tabled in Table II.

4-2. Vibrational analysis for the $\tilde{C}\,^2\Sigma^+$ state

The vibrational parameters in the $\tilde{C}\,^2\Sigma^+$ state were determined by fitting the band origins in Table II to a following simple expansion formula.

$$\nu = T_e + \sum \omega_i (v_i + d_i/2) + \sum \omega_{ij} (v_i + d_i/2)(v_j + d_j/2) + g_{22}\ell^2 \qquad (3).$$

Fitted parameters are listed in Table III. All the calculated band origins agreed within 0.8 cm^{-1}, and no significant perturbation was found in the vibrational structure of the $\tilde{C}\,^2\Sigma^+$ state. All the three vibrational frequencies (ω_1, ω_2, ω_3) could be determined for the $\tilde{C}\,^2\Sigma^+$ state for the first

Table II.

Rotational constants and band origins of the $\tilde{C}\,^2\Sigma^+$ state (in cm^{-1} unit). [a]

vibronic states	rotational constant	band origin
000 Σ	0.413 18(34)	26661.800 5(48)
010 Π	0.414 33(14)	27126.636 3(30)
020 Σ	0.415 24(50)	27590.133 4(72)
020 Δ	0.414 2(13)	27593.707(25)
100 Σ	0.409 45(37)	28520.898 0(71)
110 Π	0.406 68(53)	28974.49 6(11)
002 Σ	0.409 02(27)	29118.963 8(57)
120 Σ	0.413 25(43)	29426.278 3(73)
120 Δ	0.411 46(67)	29429.825 1(95)
101 Σ	0.406 4(12)	29735.267(18)
200 Σ	0.406 24(47)	30359.887 9(96)
210 Π	0.409 0(11)	30802.041(18)
220 Σ	0.405 72(80)	31241.795 1(99)
220 Δ	0.407 9(16)	31244.949(34)
201 Σ	0.387 1(19)	31552.617(28)
300 Σ	0.399 4(15)	32174.991(20)

[a]Numbers in parentheses are one standard deviation in unit of last significant digit.

Table III.

Vibrational parameters of the CCN radical in the $\tilde{C}\,^2\Sigma^+$ state (in cm^{-1} unit). [a]

T_e = 24627.01(20)

ω_1 = 1903.1(11), ω_2 = 469.88(38), ω_3 = 1256.6(40)

x_{11} = 10.85(20), x_{12} = 11.47(20), x_{13} = 20.57(76)

x_{22} = 0.0 (fixed), x_{23} = 0.0 (fixed), x_{33} = 5.9(12)

g_{22} = 0.86(11)

[a]Numbers in parentheses are one standard deviation in unit of last significant digit.

time. Among the anharmonic constants (x_{ij}), x_{23} was not determined because of shortage of data for such combination bands as the $\tilde{C}$ (011)Π-$\tilde{X}$ (000) Π. Although x_{22} was not determined within one standard deviation in fitting, the value was very small (< 1 cm^{-1}). They were set to zero in our analysis.

Merer and Travis[1] estimated ω_2 to be 465 cm^{-1} from the ℓ-type doubling constant determined in the $\tilde{C}$ (011)Π state by using Nielsen's formula.[15] The experimentally determined ω_2 is 469.88(38) cm^{-1}, and their estimation agrees well with the present value, which is directly determined. As will be discussed in a following section, ω_2 is an important data for the analysis of the Renner-Teller interaction. The determined value of ω_3, 1,256.6(40) cm^{-1}, is a reasonable one, because ω_3 of the $\tilde{A}^2\Delta$ state, 1,241.64 cm^{-1},[1] is very close to that of the $\tilde{C}^2\Sigma^+$ state, where both the $\tilde{C}^2\Sigma^+$ and $\tilde{A}^2\Delta$ states arise from the same electronic configuration.

5. Discussion

5-1. Rotational constants of the $\tilde{C}^2\Sigma^+$ state

In Fig.4, the rotational constants of the $\tilde{C}^2\Sigma^+$ state were plotted as a function of the vibrational term energies. It is reasonable that rotational constants decrease as the two stretching modes (υ_1 and υ_3) are excited, while they increase as excitation of the bending mode (υ_2). Constants of the $\tilde{C}$ (110)Π, $\tilde{C}$ (220)Σ, Δ, and $\tilde{C}$ (201)Σ states deviated to some extent from this simple tendency. The deviation is 4 % at most. This means that some perturbation affects not locally to the rotational levels but wholly to the vibrational bands, because rotational structures of all the sixteen observed band were fitted well without considering any perturbations. Attempt to find the possible vibrational states perturbing these states by considering

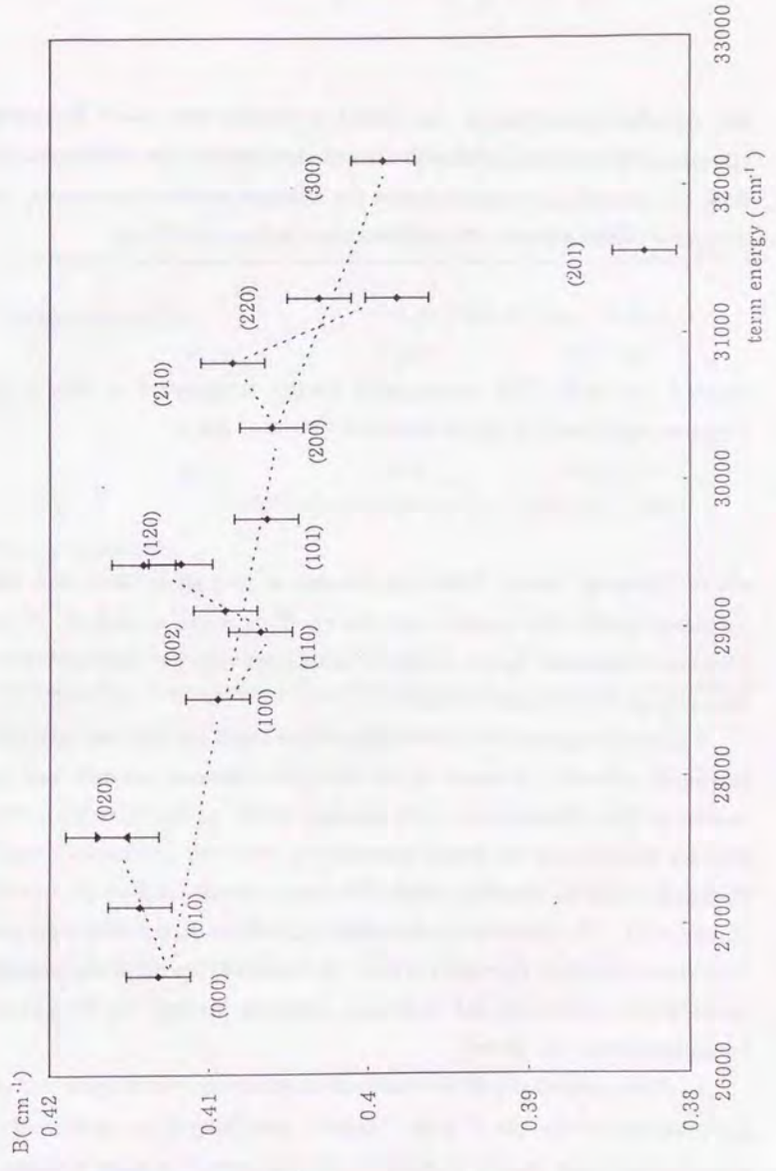

Figure 4 The rotational constant vs the vibronic term energy.

the Coriolis interaction or the Fermi resonance was made by using vibrational parameters of the $\tilde{C}$ state determined in the present study. Both two perturbations could change the effective rotational constants. A dominant matrix element of Coriolis interaction is,

$$< v_2', v_i' \mid p_2Q_i \text{ or } p_iQ_2 \mid v_2, v_i >, \qquad (4)$$

where i = 1 or 3. The second order energy proportional to $N(N+1)$, therefore the correction for the rotational constant (ΔB) is

$$\Delta B \propto |< v_2', v_i' \mid p_2Q_i \text{ or } p_iQ_2 \mid v_2, v_i >|^2/\Delta E, \qquad (5)$$

where ΔE is an energy difference between a perturbing state and the perturbed state. The selection rule for eq. (5) is $\Delta v_2 = \pm 1$ and $\Delta v_i = \pm 1$. There are no possible states which can be interact with the three perturbed states by eq. (5) with small enough ΔE.

Fermi resonance with stretching modes could decrease the effective rotational constant. Increase of the effective rotational constant can be caused by Fermi interaction with bending modes to the contrary. The primary contribution for Fermi resonance is the cubic anharmonic term, $k_{ijk}Q_iQ_jQ_k$, and the selection rule for this matrix element is $\Delta v_i = \pm 1$, $\Delta v_j = \pm 1$ and $\Delta v_k = \pm 1$. The plausible states satisfying such a selection rule were not found near the three perturbed states. In Table IV, the ΔE of the nearest states which can change the rotational constants through the Coriolis or Fermi interaction are shown.

Thus, irregularity of the rotational constants can not be explained by perturbations within the $\tilde{C}$ state. Another possibility to be considered is perturbations with nearby vibrational states belonging to other electronic states. The $\tilde{B}\,^2\Sigma^-$ state is located at 4,200 cm^{-1} below the $\tilde{C}$ state. However, it is difficult to specify the type of perturbation and the perturbing states.

Table IV.

Energy differences form the possible vibronic states as perturber.

possible perturber	perturbed state	energy difference
Coriolis interaction		
(021)	(110)	-150 cm^{-1}
(131)	(220)	+150 cm^{-1}
(112)	(220)	+150 cm^{-1}
(230)	(201)	+130 cm^{-1}
Fermi interaction		
(050)	(110)	+15 cm^{-1}
(023)	(220)	+15 cm^{-1}
(141)	(201)	-10 cm^{-1}

5-2. The vibronic structure of the $\tilde{X}\,^2\Pi$ state

In the present study, the band origins of the $\tilde{C}\,(010)\Pi$-$\tilde{X}\,(000)\Pi_{1/2}$ and $\tilde{C}\,(020)\Delta$-$\tilde{X}\,(000)\Pi_{1/2}$ transitions, whose upper states had been observed in the absorption spectra of the $\tilde{C}\,(010)\Pi$-$\tilde{X}\,(010)\Delta_{3/2,\,5/2}$ and $\tilde{C}\,(020)\Delta$-$\tilde{X}\,(020)\Phi_{5/2,\,7/2}$ by Merer and Travis[1], were determined. They reported the band origin of the $\tilde{C}\,(010)\Pi$-$\tilde{X}\,(010)\Delta_{3/2,\,5/2}$ as 26,947.37 cm^{-1} and the band heads of $\tilde{C}\,(020)\Delta$-$\tilde{X}\,(020)\Phi_{5/2}$ and $\tilde{C}\,(020)\Delta$-$\tilde{X}\,(020)\Phi_{7/2}$ as 27,033.6 cm^{-1} and 27,000.2 cm^{-1}, respectively. Simulation of the absorption spectrum of $\tilde{C}\,(020)\Delta$-$\tilde{X}\,(020)\Phi_{5/2,7/2}$ was made under the room temperature and the band origin to be 27,019.9 cm^{-1} was derived by comparing the simulated band heads with those reported by Merer and Travis.[1] The error in the estimation is considered to be 0.5 cm^{-1}. The molecular constants shown in Table I together with those reported by Kawaguchi *et al.*[6] were used. The intervals of $\tilde{X}\,(010)_{\mu}\Sigma$-$\tilde{X}\,(000)\Pi$ and $\tilde{X}\,(020)\Phi$-$\tilde{X}\,(000)\Pi$ were thus determined by combining these values with all the available data. The vibronic structure of the $\tilde{X}\,(0v_20)$ is shown in Fig. 5.

Brazier *et al.*[5] determined the Renner-Teller parameter, $\varepsilon = 0.410$, and the bending frequency $\omega_2 = 324.0$ cm^{-1} by applying the theory on the Renner-Teller effect, which were developed by Hougen[7] and Brown[10], to the vibronic structure of the υ_3 excited states $\tilde{X}\,(0v_21)$, as shown in Fig. 5. According the theory, the vibronic structure subjected to the Renner-Teller effect can be expressed as follows.[7,10,11]

$$(000)\Pi = T_0 - 1/4\varepsilon^2\omega_2, \quad (6)$$

$$(010)_{\mu}\Sigma = T_0 + \omega_2 - 1/4\varepsilon^2\omega_2 - 1/2(A_{true}^2+4\varepsilon^2\omega_2^2)^{1/2}, \quad (7)$$

$$(010)\Delta = T_0 + \omega_2 - 3/4\varepsilon^2\omega_2 + 2g_K, \quad (8)$$

and

$$(020)\Phi = T_0 + 2\omega_2 - 3/2\varepsilon^2\omega_2 + 3g_K, \quad (9)$$

The vibronic structure of the $X^2\Pi$ state

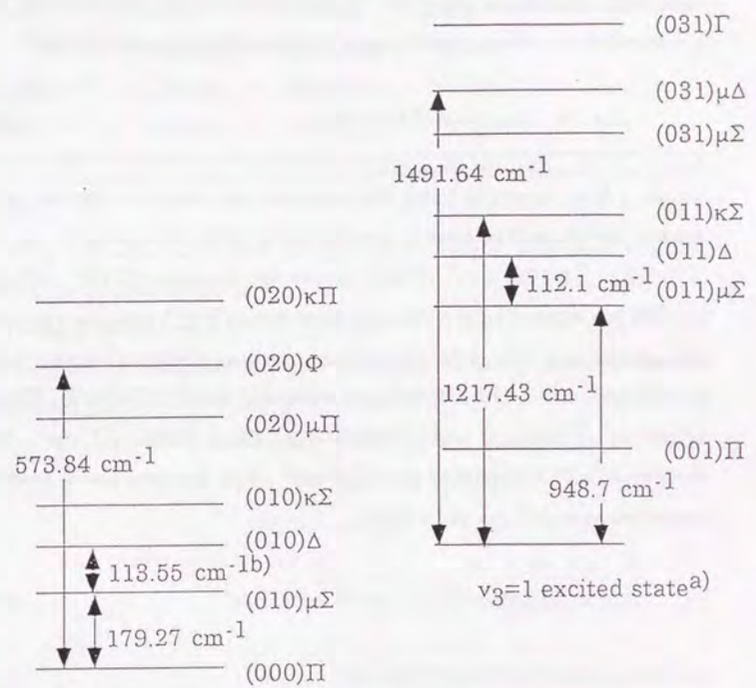

a) reference 6

b) reference 1

Figure 5 The vibronic structure of the $\tilde{X}\,^2\Pi_r$ state.

where A_{true} is the *true* spin-orbit interaction constant and g_K is a correction term for *K*-dependence introduced by Brown.[10] It is noted that eqs. (6)-(9) hold for the positions of the vibronic levels without the spin-orbit splittings, that is, they represent the center of the spin-orbit pair states. The effective spin-orbit interaction constant, $A_{eff.}$, for the K = v_2 + 1 state in the Π electronic state, which is called as a "unique state", is expressed as[10]

$$A_{eff.} = A_{true}\{1-\varepsilon^2 K(K+1)/8+K\eta\}, \quad (10)$$

where η is a correction term derived from the second order perturbation calculation of the first term in the Herzberg-Teller expansion.[10] $A_{eff.}$ of the $\tilde{X}(000)\Pi$, $\tilde{X}(010)\Delta$ and $\tilde{X}(020)\Phi$ states are the case of (10). When eqs. (6)-(10) are applied to the vibronic structure in Fig. 5 and $A_{eff.}$ reported by Kawaguchi *et al.*[6] for $\tilde{X}(0v_20)$, a fitting procedure yielded a negative value of g_K = -9.0(50) cm^{-1}. Other fitted parameters are listed in Table V. The band origins of $\tilde{X}(010)\Delta_{,,}\Sigma$ and $\tilde{X}(020)\Phi$ were fitted within 0.1 cm^{-1}. While, Brazier *et al.*[5] determined g_K = 2.5 cm^{-1}. The g_K term has a first order contribution on the $|\Lambda\, v_2\, \ell>$ basis,

$$<\Lambda\, v_2\, \ell\, |\, g_K(G_K+L_z)L_z\, |\, \Lambda\, v_2\, \ell> = g_K K\Lambda, \quad (11)$$

and the g_K constant is represented as

$$g_r = \sum_{\Lambda=\Delta,\Sigma} \frac{(-1)^r \left|\langle \Pi | H_{rr} | \Lambda' \rangle\right|^2}{(\Delta E)^2}, \quad (12)$$

where H_{HT} is the Herzberg-Teller interaction term and ΔE is the energy difference between the Π electronic state and an excited Σ or Δ electronic state. p is even or odd when the perturbing state is Σ or Δ, respectively.[10] As the g_K constant is explained by a second order perturbation with an

Table V.

Vibronic parameters in the $\tilde{X}\,^2\Pi$ state.[d]

	(a)	(b)	(c)
ω_2(/cm^{-1})	353(15)	319.9(11)	324.0
ε	0.489(24)	0.4305(43)	0.410
A_{true} (/cm^{-1})	41.09(11)	41.99(19)	41.76
g_K(/cm^{-1})	-9.0(52)	2.5 (fixed)	2.5

(a) ω_2, ε, A_{true}, and g_K are varied as parameters in the least-square fitting procedure.

(b) ω_2, ε, and A_{true} are varied as parameters in the least-square fitting procedure. g_K is fixed at 2.5 cm^{-1}.

(c) Values from reference 5.

[d]Numbers in parentheses are one standard deviation in unit of last significant digit.

excited electronic state, it is unreasonable that excitation of the υ_3 stretching mode causes large change for the g_K value. Similar vibronic parameters to those suggested by Brazier *et al.* could be obtained by fixing $g_K = 2.5$ cm^{-1}. In this case, the band origins were fitted within 1.3 cm^{-1}. The results are listed in Table V together with vibronic parameters by Brazier *et al.*. If contribution from the $\tilde{A}\,^2\Delta$ state is dominant in eq. (12), g_K has a negative value.[10] However, vibronic structures of $\tilde{X}(0v_20)$ and $\tilde{X}(0v_21)$ can be reproduced fairly well by assuming the positive (2.5 cm^{-1}) value of g_K. Hakuta and Uehara[4] suggested the interval between $\tilde{X}(010)_\kappa\Sigma$ and $\tilde{X}(010)_\mu\Sigma$ was 276 cm^{-1}, which corresponds to $(A_{true}{}^2+4(\varepsilon\omega_2)^2)^{1/2}$. The set of vibronic parameters with $g_K = -9.0$ cm^{-1} did not show good agreement with this value. While the other set with $g_K = 2.5$ cm^{-1} reproduced the locations of $\tilde{X}(010)\Delta$ and $\tilde{X}(010)_\mu\Sigma$ within 1 cm^{-1}.

5-3. The vibronic structure of the $\tilde{A}\,^2\Delta$ state

Kawaguchi *et al.*[6] determined the band origins of the $\tilde{A}(000)\Delta$-$\tilde{X}(000)\Pi$, $\tilde{A}(010)\Phi$-$\tilde{X}(010)\Delta$, $\tilde{A}(010)\Pi$-$\tilde{X}(010)_\mu\Sigma$ and $\tilde{A}(020)\Phi$-$\tilde{X}(020)\Gamma$ as 21,259.20 cm^{-1}, 21427.51 cm^{-1}, 21,527.67 cm^{-1} and 21,605.69 cm^{-1}, respectively. The vibronic structures of the $\tilde{X}\,^2\Pi$ state shown in Fig. 5 and data on the $\tilde{A}\,^2\Delta$-$\tilde{X}\,^2\Pi$ band yield the vibronic structure of the $\tilde{A}\,^2\Delta$ state as shown in Fig.6. According to the reference 23, the vibronic structures subjected by the Renner-Teller effect in the Δ electronic state are given in the following expressions. For the unique levels with $|K| > v_2$,

$$E_K = \omega_2(v_2+1) + (3/2)g_4(v_2+1)^2 + g_{22}K^2 + \Lambda|K|(g_K-2g_{22}). \qquad (13)$$

Therefore,

The vibronic structure of the $A^2\Delta$ state

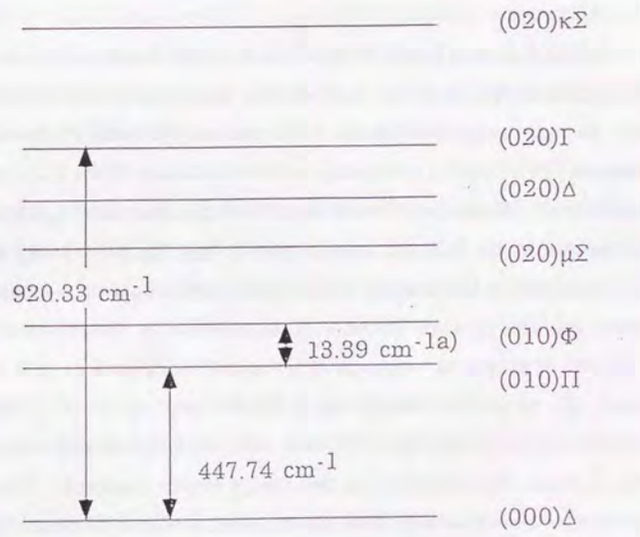

a)reference 1

Figure 6 The vibronic structure of the $\tilde{A}\,^2\Delta$ state.

$$\upsilon(\tilde{A}\,(010)\Pi\text{-}\tilde{A}\,(000)\Delta) = \omega_2 + (9/2)g_4 + 5g_{22} - 2g_K, \quad (14)$$

$$\upsilon(\tilde{A}\,(010)\Phi\text{-}\tilde{A}\,(010)\Pi) = 4g_K, \quad (15)$$

$$\upsilon(\tilde{A}\,(020)\Gamma\text{-}\tilde{A}\,(000)\Delta) = 2\omega_2 + 12g_4 + 3g_{22} + 6g_K, \quad (16)$$

Eqs. (17)-(19) were applied to the vibronic structure in Fig. 6, where $g_4 = -2g_{22}$[14] was assumed. Determined vibronic parameters for the $\tilde{A}\,^2\Delta$ state are, $\omega_2 = 457.1\ cm^{-1}$, $g_K = 3.35\ cm^{-1}$, and $g_{22} = 0.66\ cm^{-1}$.

5-4. Dissociation in the excited electronic states

Bondybey and English[16] reported that the absorption spectra of the CCN radical in the Ar matrix decreased by long-term irradiation of the UV light. Jacox[17] reported that the CNC radical had been produced by the reaction of CN + C in the matrix cage after dissociation of the CCN radical by UV radiation. Merer and Travis[1] suggested the dissociation energy of the CCN radical to be 3.61 eV, from a result that the absorption spectrum disappeared at $J = 41/2$ level in the $\tilde{C}\,(110)\Pi$ vibronic state. Against these previous reports, no such evidence of dissociation as disappearance of the LIF signals or prominent decrease of the radiative lifetime has not observed even at the excitation energy up to 32,000 cm^{-1} or 4 eV. Any faster intramolecular processes than 300 nsec, which is a typical radiative lifetime of the $\tilde{C}$ state, does not occur in the energy region observed. This means that the dissociation energy D is greater than 4 eV. However, it is noted that our experimental condition is different from previous observations. Dissociation in the Ar matrix does not necessarily correspond to that of isolated molecules. Merer and Travis observed the absorption spectra of relatively high J transitions under the room temperature. If the dissociation process they observed has large J-dependence, the evidence of the dissociation can not be found for the low J transitions observed even at a

higher excitation energy in the present study.

5-5. Vibronically induced bands.

In the present study, the weak bands with $\Delta\ell = 1$, $\tilde{C}\,(v_1,1,0)\Pi\text{-}\tilde{X}\,(0,0,0)\Pi$, were observed. They are forbidden by symmetry of the vibrational wavefunction ($\Delta\ell$ = even). The intrinsic electronic transition moment of the $\tilde{C}\,^2\Sigma^+\text{-}\tilde{X}\,^2\Pi$ transition is perpendicular to the molecular axis ($\Delta\Lambda = \pm1$). However, the rotational structures of these weak bands agreed well with a simulation assuming a parallel transition moment ($\Delta\Omega = 0$). This means that some vibronic interaction violates the selection rule and induces the vibronic transitions with $\Delta K = 0$. For these vibronically induced bands, there are following possible mechanisms (a) - (c).

(a) Herzberg-Teller interaction between the $\tilde{C}\,^2\Sigma^+$ state and the $\tilde{X}\,^2\Pi$ state

If the $\tilde{C}\,^2\Sigma^+$ state and $\tilde{X}\,^2\Pi$ state were mixed by the Herzberg-Teller interaction, non-zero electronic transition moment arises as follows.

$$|\ C'\ K=1> = |\ \Sigma,\ K=1> - \alpha|\ \Pi,\ K=1>, \quad (17)$$

$$|\ X'\ K=1> = \alpha\ |\ \Sigma,\ K=1> + |\ \Pi,\ K=1>, \quad (18)$$

$$\alpha = <\Sigma,\ K=1\ |\ H_{HT}\ |\ \Pi,\ K=1>, \quad (19)$$

where C' and X' represent resultant vibronic states corresponding to $\tilde{C}\,(v_1 10)\Pi$ and $\tilde{X}\,(000)\Pi$, respectively, and $|\Lambda,K>$ is the Born-Oppenheimer state to be mixed by the Herzberg-Teller interaction, H_{HT}. α is the matrix element of the Herzberg-Teller interaction between $\tilde{C}$ and $\tilde{X}$. The transition moment μ is thus expressed as,

$$<C'\ K=1\ |\ \mu\ |\ X'\ K=1>$$

$$= \alpha (<\Sigma, K=1 \mid \mu \mid \Sigma, K=1> - <\Pi, K=1 \mid \mu \mid \Pi, K=1>). \quad (20)$$

For a rough estimation, 0.594 Debye and 3.30 Debye were used for the permanent dipole moments of the $\tilde{X}\,^2\Pi$ and $\tilde{C}\,^2\Sigma^+$ states, respectively, reported in an *ab initio* calculation.[24] Intensity of the vibronically induced bands was roughly 1 % of other allowed electronic transitions.

$$|<C' \mid \mu \mid X'>|^2 : |<\Sigma \mid \mu \mid \Pi>|^2 = 1 : 100. \quad (21)$$

If the intrinsic electronic transition moment of 0.7 Debye estimated from the radiative lifetime of 300 nsec for the $\tilde{C}\,^2\Sigma^+$-$\tilde{X}\,^2\Pi$ transition is used, the matrix element of the Herzberg-Teller interaction, α, is estimated to be 800 cm^{-1}. In the Herzberg-Teller expansion, the Renner-Teller interaction term is the next higher order term than the Herzberg-Teller interaction. For the CCN radical in the $\tilde{X}\,^2\Pi$ state, the matrix element of the Renner-Teller effect was estimated to be $\varepsilon\omega_2 = 144$ cm^{-1}. The ratio between the Renner-Teller effect and the Hertzberg-Teller interaction is not considered to be unusual. In this estimation, the intensity borrowing is assumed to be caused totally by the Hertzberg-Teller interaction between the $\tilde{X}\,^2\Pi$ and $\tilde{C}\,^2\Sigma^+$ state. Although Brown *et al.*[25] explained the intensity of the vibronically induced bands of the NCO radical by the similar estimation satisfactorily, they noted other mechanism could induce the intensity borrowing.

(b) The Herzberg-Teller interaction between the $\tilde{C}\,^2\Sigma$ state and upper Π electronic states

The $\tilde{C}\,^2\Sigma$ state is the highest electronic state among the known electronic states of CCN. The next higher electronic configuration, $(3\sigma)^2(1\pi)^3(4\sigma)^2(2\pi)^2$, produces Π electronic states,

... $(3\sigma)^2(1\pi)^4(4\sigma)^2(2\pi)^1$ $\tilde{X}\,^2\Pi_r$

... $(3\sigma)^2(1\pi)^4(4\sigma)^1(2\pi)^2$ $\tilde{C}\,^2\Sigma^+$, $\tilde{B}\,^2\Sigma^-$, $\tilde{A}\,^2\Delta$, $a^4\Sigma^-$

... $(3\sigma)^2(1\pi)^3(4\sigma)^2(2\pi)^2$ $^2\Pi_r$, $^2\Pi_i$, $^2\Pi_r$, $^4\Pi_r$, $^2\Pi$, $^2\Phi_i$

These upper Π electronic states can interact with the $\tilde{C}\,(v_1 1 v_3)\Pi$ vibronic states through the Hertzberg-Teller interaction and the $\tilde{C}\,^2\Sigma^+$ state could borrow intensities of the electronic transition from the $\tilde{X}\,^2\Pi_r$ state.

(c) The dependence of the electric dipole moment on the nuclear motion

In general, the electric dipole moment of a molecule is a function of the nuclear coordinates, and we can expand it around the equilibrium molecular structure.

$$\mu(r, Q) = \mu_e(r) + \mu'(r)Q + \mu''(r)Q^2 + \ldots . \quad (22)$$

In this expression, Q is the bending coordinate and r is the coordinate of electrons. $\mu_e(r)$ represents the electronic dipole function at the linear molecular structure. Actually Q is the coordinate of the two dimensional harmonic oscillator, $Q = (Q_x, Q_y)$ and its symmetry is Π. For the Born-Oppenheimer state, the electronic transition moment between $\tilde{C}\,(010)\Pi$ and $\tilde{X}\,(000)\Pi$ is represented as follows,

$$\begin{aligned} &<\tilde{C}\,^2\Sigma^+ \mid <v_2'=1, \ell'=1(\text{odd}) \mid \mu(r, Q) \mid v_2''=0, \ell''=0(\text{even})> \mid \tilde{X}\,^2\Pi> \\ &= <\tilde{C}\,^2\Sigma^+ \mid \mu_e \mid \tilde{X}\,^2\Pi><\ell'=\text{odd} \mid \ell''=\text{even}> \\ &+ <\tilde{C}\,^2\Sigma^+ \mid \partial\mu/\partial Q \mid \tilde{X}\,^2\Pi><\ell'=\text{odd} \mid Q \mid \ell''=\text{even}> \\ &+ \text{higher order.} \end{aligned} \quad (23)$$

State with even/odd of ℓ does not mix by the first term in eq. (23). On the other hand, since the symmetry of $\partial\mu_x/\partial Q$ is Π, the second term survives. As a result, parallel type transition moments (μ_x) may be observed. The second term corresponds to the electronic transition moment when the molecular structure deviates from its equilibrium structure, that is, the bent structure. Since the electronic transition occurs adiabatically, contribution to the total transition probability from the instantaneous bent structure may not be necessarily zero. The operator $\partial\mu/\partial Q$ itself is known as the vibrational transition moment in vibrational spectroscopy. The matrix element of $\partial\mu/\partial Q$ in eq. (23) is, however, that between different electronic states. Although estimation of the matrix element $< \tilde{C}\,^2\Sigma^+ \mid \partial\mu/\partial Q \mid \tilde{X}\,^2\Pi >$ is difficult, this term can contribute to the parallel type transition of $\tilde{C}\,(v_1 10)\Pi - \tilde{X}\,(000)\Pi$.

The three mechanisms mentioned above can occur simultaneously, and all the contributions can give parallel type transitions. For more quantitative discussion, following information is necessary for each mechanism.

(a) It is necessary to know an expectation value of Λ, therefore, to know the degree of mixing between the $\tilde{C}\,^2\Sigma^+$ state and the $\tilde{X}\,^2\Pi$ state.

(b) If we know the location of the upper Π electronic states, estimation of the Herzberg-Teller Effect due to the second mechanism can be possible.

(c) *Ab initio* calculations for the $\tilde{C}\,^2\Sigma^+$ state and the $\tilde{X}\,^2\Pi$ state will be able to estimate the matrix element of $\partial\mu/\partial Q$.

6. Summary

The electronic transition of the CCN radical in the $\tilde{C}\,^2\Sigma^+$- $\tilde{X}\,^2\Pi$ band system has been studied. Rotational constants and vibrational parameters

of the $\tilde{C}\,^2\Sigma^+$ state have been determined. No significant perturbation was found in the $\tilde{C}\,^2\Sigma^+$ state. Observation of the $\Delta v_2 = 1$ bands led us to reproduce the vibronic structures of $\tilde{X}\,^2\Pi(0v_20)$ and $\tilde{A}\,^2\Delta(0v_20)$ enabling re-analysis of the Renner-Teller interaction for these states. These bands have been explained as the vibronically induced bands, and mechanism of the intensity borrowing has been discussed.

References

[1]A. J. Merer and D. N. Travis, Can. J. Phys. 43, 1795 (1965).

[2]M. Kakimoto and T. Kasuya, J. Mol. Spectrosco. 94, 380 (1982).

[3]Y. Ohshima and Y. Endo, J. Mol. Spectrosco. 172, 225 (1995).

[4]K. Hakuta and H. Uehara, J. Chem. Phys. 78, 6484 (1983).

[5]C. R. Brazier, L. C. O'Brien, and P. F. Bernath, J. Chem. Phys. 86, 3078 (1987).

[6]K. Kawaguchi, T. Suzuki, S. Saito, and E. Hirota, J. Mol. Spectrosco. 106, 320 (1984).

[7]J. T. Hougen, J. Chem. Phys. 36, 519 (1962).

[8] J. A. Pople and H. C. Longuett-Higgins, Mol. Phys. 1, 382 (1958).

[9] A. Carrington, A. R. Fabris, B. J. Howard, and N. J. Lucus, Mol. Phys. 20, 1961 (1971).

[10]J. M. Brown, J. Mol. Spectrosco. 68, 412 (1977).

[11]J. F. M. Aarts, Mol. Phys. 35, 1785 (1978).

[12]Ch. Jungen and A. J. Merer, Mol. Phys. 40, 1 (1980).

[13]D. Gauyacq and Ch. Jungen, Mol. Phys. 41, 383 (1980).

[14]J. M. Brown and F. Jørgensen, Mol. Phys. 47, 1065 (1982).

[15]H. H. Nielsen and W. H. Shaffer, J. Chem. Phys. 11, 140 (1943).

[16]V. E. Bondybey and J. H. English, J. Mol. Spectrosco. 70, 236 (1978).

[17]M. E. Jacox, J. Mol. Spectrosco. 71, 369 (1978).

[18]Y. Ohshima and Y. Endo, J. Mol. Spectrosco. 153, 627 (1992).

[19]Y. Endo, H. Kohguchi, and Y. Ohshima, Faraday Discuss. 97, 341 (1994).

[20]S. Gerstenkorn, J. Verges, and J. Chevillard, "*Atlas du Dpectre d'Absorption de la Molecule d'Iode*," CNRS, Paris, 1982.

[21]I. C. Bowater, J. M. Brown, and A. Carrington, Proc. R. Soc. Lond. A. 333, 265 (1973).

[22]J. M. Brown, M. Kaise, C. M. L. Kerr, and D. J. Milton, Mol. Phys. 36, 553 (1978).

[23]J. M. Brown and F. Jørgensen, Adv. Chem. Phys. 52, 117 (1983).

[24]K. Yamashita and K. Morokuma, Chem. Phys. Lett. 140, 345 (1987).

[25]P. S. H. Bolman and J. M. Brown, Chem. Phys. Lett. 21, 213 (1973).

Appendix. Observed frequencies of the $\tilde{C}\,^2\Sigma^+$-$\tilde{X}\,^2\Pi$ band system of the CCN radical

$\tilde{C}\,(000)\Sigma$-$\tilde{X}\,(000)\Pi$

N'	J"	obs.	obs.-calc.
0	3/2	26680.407	0.002
1	5/2	26679.278	0.019
2	7/2	26678.149	-0.002
3	9/2	26677.098	0.015
0	1/2	26681.588	-0.001
1	3/2	26681.243	0.010
2	5/2	26680.920	0.004
3	7/2	26680.633	-0.004
1	1/2	26682.407	-0.007
2	3/2	26682.900	0.016
3	5/2	26683.374	-0.017
4	7/2	26683.922	-0.014
5	9/2	26684.525	0.005
2	1/2	26684.043	-0.025
3	3/2	26685.361	-0.005
4	5/2	26686.689	-0.012
5	7/2	26688.090	0.016

Appendix. Observed frequencies of the $\tilde{C}\,^2\Sigma^+$-$\tilde{X}\,^2\Pi$ band system of the CCN radical (continued)

$\tilde{C}\,(100)\Sigma$-$\tilde{X}\,(000)\Pi$

N'	J"	obs.	obs.-calc.
0	3/2	28539.484	-0.018
1	5/2	28538.348	-0.001
2	7/2	28537.231	0.004
3	9/2	28536.128	-0.007
4	11/2	28535.073	-0.001
0	1/2	28540.672	-0.015
1	3/2	28540.329	0.005
2	5/2	28539.996	0.005
3	7/2	28539.704	0.015
1	1/2	28541.499	-0.005
2	3/2	28541.963	0.004
3	5/2	28542.485	0.041
4	7/2	28542.987	0.027
5	9/2	28543.514	0.009
4	5/2	28545.714	-0.010
5	7/2	28547.044	-0.016
6	9/2	28548.412	-0.013

Appendix. Observed frequencies of the $\tilde{C}\,^2\Sigma^+$- $\tilde{X}\,^2\Pi$ band system of the CCN radical (continued)

$\tilde{C}$ (002)Σ- $\tilde{X}$ (000)Π

N'	J"	obs.	obs.-calc.
0	3/2	29137.550*	-0.018
1	5/2	29136.392	-0.022
2	7/2	29135.294	0.004
3	9/2	29134.179	-0.017
4	11/2	29133.161	0.030
0	1/2	29138.744	-0.009
1	3/2	29138.393	0.004
2	5/2	29138.048	-0.007
3	7/2	29137.752	0.002
4	9/2	29137.550*	0.075
5	11/2	29137.223	-0.006
1	1/2	29139.567	-0.002
2	3/2	29140.033	0.012
3	5/2	29140.523	0.018
4	7/2	29141.043	0.026
5	9/2	29141.584	0.026
2	1/2	29141.224	0.017
3	3/2	29142.490	0.011
4	5/2	29143.757	-0.024
5	7/2	29145.083	-0.030
6	9/2	29146.456	-0.017
7	11/2	29147.865	0.001

Appendix. Observed frequencies of the $\tilde{C}\,^2\Sigma^+$- $\tilde{X}\,^2\Pi$ band system of the CCN radical (continued)

$\tilde{C}$ (101)Σ- $\tilde{X}$ (000)Π

N'	J"	obs.	obs.-calc.
0	3/2	29753.895	0.024
1	5/2	29752.679	-0.034
2	7/2	29751.433	-0.145
0	1/2	29755.086	0.030
1	3/2	29754.706	0.019
2	5/2	29754.358	0.015
1	1/2	29755.878	0.010
2	3/2	29756.352	0.042
3	5/2	29756.800	0.023
4	7/2	29757.293	0.025
5	9/2	29757.817	0.033
2	1/2	29757.505	0.010
3	3/2	29758.745	-0.007
4	5/2	29760.021	-0.012
5	7/2	29761.307	-0.031

Appendix. Observed frequencies of the $\tilde{C}\,^2\Sigma^+$-$\tilde{X}\,^2\Pi$ band system of the CCN radical (continued)

$\tilde{C}\,(200)\Sigma$-$\tilde{X}\,(000)\Pi$

N'	J"	obs.	obs.-calc.
0	3/2	30378.597*	0.105
1	5/2	30377.343	0.010
2	7/2	30376.175	-0.022
3	9/2	30375.101	0.014
4	11/2	30374.045	0.045
0	1/2	30379.664	-0.013
1	3/2	30379.279	-0.029
2	5/2	30378.931	-0.032
3	7/2	30378.597*	-0.044
1	1/2	30380.480	-0.008
2	3/2	30380.927	-0.003
3	5/2	30381.411	0.016
4	7/2	30381.907	0.022
5	9/2	30382.402	0.003
6	11/2	30382.949	0.012
2	1/2	30382.106	-0.008
3	3/2	30383.383	0.014
4	5/2	30384.632	-0.017
5	7/2	30385.935	-0.018
6	9/2	30387.267	-0.014
7	11/2	30388.587	-0.045

Appendix. Observed frequencies of the $\tilde{C}\,^2\Sigma^+$-$\tilde{X}\,^2\Pi$ band system of the CCN radical (continued)

$\tilde{C}\,(201)\Sigma$-$\tilde{X}\,(000)\Pi$

N'	J"	obs.	obs.-calc.
0	3/2	31571.202	-0.018
1	5/2	31570.036	0.013
2	7/2	31568.785	-0.026
3	9/2	31567.608	0.023
0	1/2	31572.464	0.059
1	3/2	31571.977	-0.020
2	5/2	31571.504	-0.072
1	1/2	31573.260	0.082
2	3/2	31573.506	-0.037
3	5/2	31573.928	0.034
4	7/2	31574.328	0.098
5	9/2	31574.677*	0.125
2	1/2	31574.677*	-0.051
3	3/2	31575.784	-0.084
4	5/2	31576.939	-0.055
5	7/2	31577.986	-0.120

Appendix. Observed frequencies of the $\tilde{C}\,^2\Sigma^+$- $\tilde{X}\,^2\Pi$ band system of the CCN radical (continued)

$\tilde{C}\,(300)\Sigma$- $\tilde{X}\,(000)\Pi$

N'	J"	obs.	obs.-calc.
0	3/2	32193.675*	-0.081
1	5/2	32192.428	0.006
2	7/2	32191.164	-0.095
3	9/2	32190.097	-0.010
1	3/2	32194.447	0.051
2	5/2	32193.978	-0.046
3	7/2	32193.675*	0.014
4	9/2	32193.400	0.091
1	1/2	32195.634	0.057
2	3/2	32195.973	-0.018
3	5/2	32196.420	0.004
4	7/2	32196.918	0.068
5	9/2	32197.287	-0.009
6	11/2	32197.753	0.002
2	1/2	32197.187	0.011
3	3/2	32198.368	-0.022
4	5/2	32199.605	-0.009
5	7/2	32200.838	-0.012

Appendix. Observed frequencies of the $\tilde{C}\,^2\Sigma^+$- $\tilde{X}\,^2\Pi$ band system of the CCN radical (continued)

$\tilde{C}\,(010)\Pi$ - $\tilde{X}\,(000)\Pi$

N'	J"	obs.	obs.-calc.
1	5/2	27143.688	0.000
2	7/2	27142.586	-0.000
3	9/2	27141.518	-0.007
4	11/2	27140.489	-0.014
5	13/2	27139.532	0.011
1	3/2	27145.665	0.007
2	5/2	27145.355	0.011
3	7/2	27145.057	-0.015
4	9/2	27144.831	-0.008
1	1/2	27146.846	0.007
2	3/2	27147.312	-0.003
3	5/2	27147.842	0.011
4	7/2	27148.499*	0.012
5	9/2	27148.986	0.004
2	1/2	27148.499*	0.002
3	3/2	27149.794	-0.007
4	5/2	27151.150	0.004
5	7/2	27152.528	-0.002
6	9/2	27153.945	-0.010
7	11/2	27155.429	0.001

Appendix. Observed frequencies of the $\tilde{C}\,^2\Sigma^+$- $\tilde{X}\,^2\Pi$ band system of the CCN radical (continued)

$\tilde{C}\,(110)\Pi$ - $\tilde{X}\,(000)\Pi$

N'	J"	obs.	obs.-calc.
1	5/2	28993.511	0.001
2	7/2	28993.177	0.012
3	9/2	28992.869	0.023
4	11/2	28992.606	0.054
1	3/2	28991.508	-0.025
2	5/2	28990.358	-0.042
3	7/2	28989.312	-0.018
1	1/2	28994.682	-0.009
2	3/2	28995.098	-0.038
3	5/2	28995.631	0.026
2	1/2	28996.341	0.024
3	3/2	28997.558	-0.017
4	5/2	28998.804	-0.054
5	7/2	29000.127	-0.039
6	9/2	29001.507	-0.009
7	11/2	29002.858	0.006

Appendix. Observed frequencies of the $\tilde{C}\,^2\Sigma^+$- $\tilde{X}\,^2\Pi$ band system of the CCN radical (continued)

$\tilde{C}\,(210)\Pi$ - $\tilde{X}\,(000)\Pi$

N'	J"	obs.	obs.-calc.
1	5/2	30818.957**	-0.130
2	7/2	30818.013	0.049
3	9/2	30816.839	-0.033
1	3/2	30821.087	0.030
2	5/2	30820.740	0.017
3	7/2	30820.423	0.005
1	1/2	30822.252	0.013
2	3/2	30822.703	0.009
3	5/2	30823.158	-0.020
4	7/2	30823.686	-0.005
5	9/2	30824.236	0.003
2	1/2	30823.902	0.027
3	3/2	30825.144	-0.003
4	5/2	30826.513	0.065
5	7/2	30827.784	0.004
6	9/2	30829.114	-0.027

Appendix. Observed frequencies of the $\tilde{C}\,^2\Sigma^+$- $\tilde{X}\,^2\Pi$ band system of the CCN radical (continued)

$\tilde{C}$ (020)Σ- $\tilde{X}$ (000)Π

N'	J"	obs.	obs.-calc.
0	3/2	27608.749	0.011
1	5/2	27607.607	0.011
2	7/2	27606.496	-0.001
3	9/2	27605.438	-0.002
0	1/2	27609.920	-0.002
1	3/2	27609.556	-0.015
2	5/2	27609.250	-0.012
3	7/2	27608.979	-0.016
1	1/2	27610.739	-0.012
2	3/2	27611.224	-0.004
3	5/2	27611.764	0.016
4	7/2	27612.354*	0.044
5	9/2	27612.922	0.008
2	1/2	27612.354*	-0.006
3	3/2	27613.748	0.025
4	5/2	27615.049	-0.026
5	7/2	27616.445	-0.024

Appendix. Observed frequencies of the $\tilde{C}\,^2\Sigma^+$- $\tilde{X}\,^2\Pi$ band system of the CCN radical (continued)

$\tilde{C}$ (020)Δ- $\tilde{X}$ (000)Π

N'	J"	obs.	obs.-calc.
2	3/2	27614.373	-0.010
3	5/2	27614.896	-0.000
4	7/2	27615.544*	0.094
5	9/2	27616.031	-0.012
3	3/2	27615.544*	-0.023
4	5/2	27616.849	-0.021
5	7/2	27618.207	-0.006
6	9/2	27619.600	0.003
7	11/2	27620.996	-0.024

Appendix. Observed frequencies of the $\tilde{C}\,^2\Sigma^+$- $\tilde{X}\,^2\Pi$ band system of the CCN radical (continued)

$\tilde{C}\,(120)\Sigma$- $\tilde{X}\,(000)\Pi$

N'	J"	obs.	obs.-calc.
0	3/2	29444.867	-0.022
1	5/2	29443.732	-0.005
2	7/2	29442.536**	-0.094
3	9/2	29441.616**	0.055
4	11/2	29440.527	-0.003
0	1/2	29446.082	0.015
1	3/2	29445.709	-0.003
2	5/2	29445.371	-0.024
3	7/2	29445.086	-0.029
1	1/2	29446.913	0.021
2	3/2	29447.379	0.017
3	5/2	29447.883	0.014
4	7/2	29448.508*	0.092
5	9/2	29448.979	-0.021
6	11/2	29449.636	0.014
2	1/2	29448.508*	-0.039
3	3/2	29449.873	0.029
4	5/2	29451.176	-0.003
5	7/2	29452.522	-0.032

Appendix. Observed frequencies of the $\tilde{C}\,^2\Sigma^+$- $\tilde{X}\,^2\Pi$ band system of the CCN radical (continued)

$\tilde{C}\,(120)\Delta$- $\tilde{X}\,(000)\Pi$

N'	J"	obs.	obs.-calc.
2	5/2	29448.508*	-0.012
3	7/2	29448.246	0.017
2	3/2	29450.479	-0.008
3	5/2	29451.005	0.022
4	7/2	29451.640*	0.125
5	9/2	29452.079	-0.002
2	1/2	29451.640*	-0.031
3	3/2	29452.978	0.020
4	5/2	29454.286	0.007
5	7/2	29455.629	-0.007
6	9/2	29457.019	-0.006

Appendix. Observed frequencies of the $\tilde{C}\,^2\Sigma^+$- $\tilde{X}\,^2\Pi$ band system of the CCN radical (continued)

$\tilde{C}\,(220)\Sigma$- $\tilde{X}\,(000)\Pi$

N'	J"	obs.	obs.-calc.
0	3/2	31260.532*	0.133
1	5/2	31259.266	0.027
2	7/2	31258.063	-0.039
3	9/2	31257.005	0.017
0	1/2	31261.616	0.032
1	3/2	31261.214	0.000
2	5/2	31260.847	-0.020
3	7/2	31260.532*	-0.010
1	1/2	31262.400	0.007
2	3/2	31262.830	-0.003
3	5/2	31263.269	-0.027
4	7/2	31263.775	-0.007
5	9/2	31264.313	0.022

Appendix. Observed frequencies of the $\tilde{C}\,^2\Sigma^+$- $\tilde{X}\,^2\Pi$ band system of the CCN radical (continued)

$\tilde{C}\,(220)\Delta$- $\tilde{X}\,(000)\Pi$

N'	J"	obs.	obs.-calc.
2	1/2	31266.711	-0.066
3	3/2	31268.086	0.043
4	5/2	31269.398	0.062
5	7/2	31270.674	0.017
6	9/2	31271.959	-0.046
2	3/2	31265.564	-0.028
3	5/2	31266.086	0.018

The frequency marked by * indicates a blended line.

The frequency marked by ** indicates a contaminated line with by-products.

Chapter V

Laser induced fluorescence spectra and quantum beats in the fluorescence of the $\tilde{A}\,^2\Pi_i$-$\tilde{X}\,^2\Pi_i$ transition of the HCCS radical

Abstract

Laser induced fluorescence (LIF) spectra of the $\tilde{A}\,^2\Pi_i$-$\tilde{X}\,^2\Pi_i$ transition of the HCCS radical have been observed in a supersonic jet by using a pulsed-discharge nozzle. The spectral range of 3,000 cm^{-1} from the origin band(0_0^0 $^2\Pi_{1/2}$-$^2\Pi_{1/2}$ at 24,000 cm^{-1}) was scanned and 30 vibronic bands were observed. Assignment of Ω' and Ω'' to each vibronic band was possible from the rotational structure. It has been suggested that the previous assignments for hot bands of the CCS bending mode (υ_4) are questionable. Zero-field quantum beat phenomena have been observed for the fluorescence decay. A simple beat observed in the region near the origin has gradually turned to a quasi biexponential temporal behavior as the excitation energy of the laser was increased. A qualitative discussion on the quantum beats shows that the observed quantum beats are due to the internal conversion between the $\tilde{A}\,^2\Pi_i$ state and the highly excited vibrational states in the $\tilde{X}\,^2\Pi_i$ state.

1. Introduction

The first spectroscopic observation of the HCCS radical was made by Krishnamachari and Ramsay.[1] They observed an absorption spectrum of this radical in the 411 nm region by the flash photolysis of thiophene (C_4H_4S). They also observed a corresponding spectrum of an isotopomer, DCCS. From the rotational constants and isotope shifts, they identified the carriers to be HCCS/DCCS and determined the origin (0_0^0). In 1985, Coquart observed high resolution spectra of the same electronic transition by dispersing the emission from a discharge of thiophene.[2] He assigned 40 vibronic bands including hot bands to vibronic transitions other than those concerned to the CH stretching mode. He concluded that the nature of the electronic transition was $\tilde{A}\,^2\Pi_i$-$\tilde{X}\,^2\Pi_i$ from the rotational structures referring to similarities to those of the NCS radical. Intervals of 210 cm^{-1} in the observed spectra were ascribed to the differences between $^2\Pi_{1/2}$-$^2\Pi_{1/2}$ and $^2\Pi_{3/2}$-$^2\Pi_{3/2}$ of the same vibronic transition. Rotational structures were analyzed for relatively strong nine bands. He used transition frequencies of high J transitions in the rotational analysis because the spectra were taken under room temperature or higher. There remained ambiguity of ± 1 in assignments of the J-numbers, because the band origins were not determined due to congestion of the Q branches. Vertilek *et al.* observed pure rotational transitions in the vibronic ground state of this radical in the millimeter wave region.[3] They measured rotational transitions frequencies both in the $\Omega = 1/2$ and $\Omega = 3/2$ states with high accuracy. They determined the spin-orbit constant, Aso, in the $\tilde{X}\,^2\Pi_i$ state to be -185 cm^{-1}.

One of the most crucial techniques for spectroscopy of free radicals is a method of producing free radical. Discharging is one of the most frequently used methods in the microwave and infrared spectroscopy of free radicals in the ground state. A pulsed-discharging method has

demonstrated its high efficiency of production in the microwave spectroscopy.[4] While in the optical spectroscopy of free radicals, a photolysis method is widely used for production. Different from a photolysis, a pulsed-discharging has no selectivity for production and it can produce many kinds of unstable species. A pulsed-discharge nozzle (PDN) can cause not only cleavage of precursors but also elongation or enlargement to produce larger polyatomic free radicals in the complex reaction of discharging. In this study, larger radicals (HCCS) than its precursors (C_2H_2 and CS_2) have been produced by a PDN.

We can sometimes obtain information on the molecular dynamics in the electronic excited states from their temporal behaviors of the fluorescence decay. Non-exponential decay and quantum beats of the fluorescence signal are such examples. For large molecules, there have been many studies on quantum beats and/or non-exponential decay in a zero-field, which can be ascribed to such processes as intramolecular vibrational energy redistribution (IVR)[5-8], intersystem crossing (ISC)[9-11], and internal conversion (IC)[12] in electronic excited states. While, zero-field quantum beats of only a few small molecules have been observed.[12,13,14] Because density of vibrational states for molecules with n vibrational modes has dependence of ε^{n-1} at a given term energy ε,[14,15] the number of vibrational modes of relatively small molecules is unfavorable for large density of states enough to cause quantum beats. The temporal behavior changing from a single exponential decay to quantum beats, and finally to a biexponential decay, was established theoretically.[16-18] Such gradual change was observed in the fluorescence decay from the S_1 state of α-dicarbonyles as a function of the density of states.[9]

In the present study, rotationally cooled LIF spectra of the $\tilde{A}\,^2\Pi_i$-$\tilde{X}\,^2\Pi_i$ system of HCCS have been observed. The radicals have been produced in a supersonic jet by a PDN. The temporal behavior of the fluorescence whose shape was not a single exponential decay, has been

observed.

2. Experimental

A tunable dye laser (Spectra Physics, PDL-3), pumped by a Q-switched Nd^+ YAG laser (Spectra Physics, GCR-3) was used in the present study. Radiation in the violet was obtained by doubling the output of the dye laser with a KDP crystal. The laser linewidth was ~ 0.12cm^{-1} (FWHM) and the duration of the laser pulse was less than 10 ns.

A pulsed-discharge nozzle (PDN) was used for production of the HCCS radical in a supersonic jet. Details on application of the PDN to LIF studies of free radicals will be described elsewhere.[19] A mixture of 1% acetylene (C_2H_2) and 0.5% carbon disulfide (CS_2) diluted in Ar was used with a stagnation pressure at 4 atm, and was expanded into a vacuum chamber through the PDN. A pulsed high voltage of 1.5kv with a duration of 20 μsec was applied two electrodes of the PDN. The vacuum chamber was kept at 1×10^{-4} Torr by a 14" diffusion pump at a flow rate of 3,000 ℓ/sec. Under this condition, the rotational temperature of the HCCS radical was reduced to 5 K in a supersonic jet stream.

Molecules were excited at 40 mm downstream from the PDN. Delay of the Q-switch from the pulse for discharging was set to 80 μsec. The fluorescence after passing through an adequate sharp-cut filter was detected by a photomultiplier tube (PMT, Hamamatsu photonics R928) and the output of the PMT was amplified by a pre-amplifier. The total fluorescence was taken by a boxcar integrator (SRS, SR250) with a gate width of 300 ns, and accumulated by a personal computer. For observation of the temporal behavior of the fluorescence, a digital oscilloscope (Tektronics TDS 320) whose maximum sampling rate was 500 MHz/s, was used. The response time (rise time) of the PMT was 2.2 nsec and the band

width of the pre-amplifier was 260 MHz at a gain of 10. The highest frequency of quantum beats observable in the present study was ~100 MHz, and the lowest one was ~ 5 MHz. The former was limited by the system response time and the latter was limited by the radiative lifetime of the $\tilde{A}\,^2\Pi_i$ state of the HCCS radical, 240 nsec.

3. Results

The frequency range of 3,000 cm^{-1} was scanned from the 0_0^0 band at 24,000 cm^{-1}. A part of the whole scan is shown in Fig. 1. In addition to the vibronic bands assigned by Coquart, the weak unassigned or unreported bands were observed together with spectra of by-products of discharging. Rotational temperature was cooled and two types of the rotational structures were observed. The difference is ascribed to the quantum numbers of Ω (the projection of total angular momentum onto the molecular axis, $\Omega=\Lambda+\Sigma+\ell$ in case (a) basis functions) as will be discussed later. Hereafter, the spin sublevels of a vibronic bands are denoted as (Ω',Ω"), where Ω' and Ω" are upper and lower Ω respectively.

Quantum beats in fluorescence decay were observed. Though there were no apparent beats on a single exponential decay in the 0_0^0 bands ((Ω',Ω")=(1/2,1/2) at 24,090 cm^{-1} and (Ω',Ω")=(3/2,3/2) at 24,300 cm^{-1}), modulated fluorescence decays began to be observed in the band at 24,660 cm^{-1}. Other vibronic bands observed at higher excitation energy than 24,660 cm^{-1} showed rather prominent modulations. The oscillating components in the fluorescence increased in number gradually with excitation energies. In each vibronic band, no significant dependence of quantum beats on the rotational transitions was not ascertained. Dependence of quantum beats on the magnetic field and polarization of

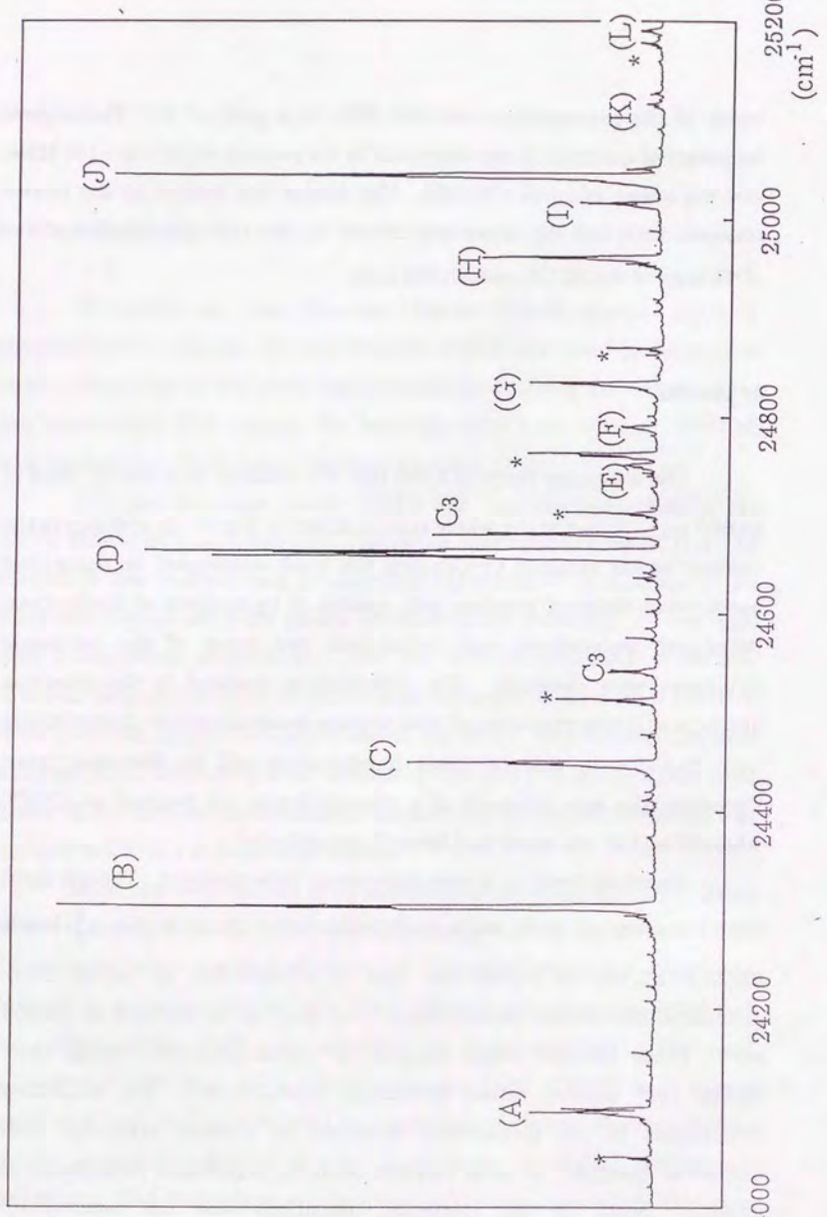

Figure 1

Figure 1. Laser induced fluorescence spectra of $\tilde{A}\,^2\Pi_i$-$\tilde{X}\,^2\Pi_i$ of HCCS by discharging of C_2H_2+CS_2/Ar with a pulsed-discharge nozzle. (A)-(L) indicates the vibronic bands of the HCCS radical. An asterisk (*) indicates a vibronic band whose carrier was not identified. The bands of the $\tilde{A}\,^1\Pi_u$-$\tilde{X}\,^1\Sigma_g^+$ of the C_3 radical were also observed. Assignment of the HCCS radicals are ; (A) 0_0^0 (Ω',Ω")=(1/2,1/2), (B) 0_0^0 (Ω',Ω")=(3/2,3/2), (C) and (D) formerly assigned as 4_1^1 bands, see the text, (E) 5_0^2 (Ω',Ω")=(1/2,1/2), (F) unassigned (Ω',Ω")=(1/2,1/2), (G) 3_0^1 (Ω',Ω")=(1/2,1/2), (H) 5_0^2 (Ω',Ω")=(3/2,3/2), (I) unassigned (Ω',Ω")=(3/2,3/2), (J) 3_0^1 (Ω',Ω")=(3/2,3/2), (K) and (L) unassigned (Ω',Ω")=(1/2,1/2).

fluorescence were not observed in this study.

4. Discussion

4-1. Jet cooled LIF spectra of the $\tilde{A}\,^2\Pi_i$-$\tilde{X}\,^2\Pi_i$ system.

Since the PDN produced the rotationally cooled HCCS radical, the rotational structures of relatively low J transitions with isolated Q-branches were observed. Both the $\tilde{A}\,^2\Pi_i$ and $\tilde{X}\,^2\Pi_i$ states were considered to be well described by the case (a) coupling scheme, because their spin-orbit interaction constants (Aso) were a few hundred cm^{-1}, while the rotational constants (B) ~ 0.2 cm^{-1}. The line strength in the Q-branch for the perpendicular type transition (ΔJ=0, $\Delta\Omega$=0) in the case (a) wavefunction are given by the following simple formula.

$$S(J',\Omega' \leftarrow J'',\Omega'') \propto \Omega^2/J(J+1), \qquad (1)$$

where $J' = J''$ ($=J$) and $\Omega' = \Omega''$ ($=\Omega$). According to eq. (1), the ratio of the line strength of the Q-branch between the (Ω', Ω'')=(3/2,3/2) and (1/2,1/2) bands is evaluated as,

$$S(\text{Q-branch}, \Omega'=\Omega''=3/2) : S(\text{Q-branch}, \Omega'=\Omega''=1/2) = 9 : 1. \qquad (2)$$

Although the laser linewidth of 0.12 cm^{-1} could not resolve each rotational line in the Q branch stack, the Q branch stack was well isolated from R and P branches in each observed band. The ratio of 9 : 1 was large enough to distinguish apparently a vibronic band with (Ω',Ω'')=(3/2,3/2) and that with (Ω',Ω'')=(1/2,1/2). In Fig.2, examples of the observed bands with (Ω',Ω'')=(3/2,3/2) and (Ω',Ω'')=(1/2,1/2) are shown. Relative intensity of the Q branch stack in each rotational structure is characteristic for the (Ω',Ω'').

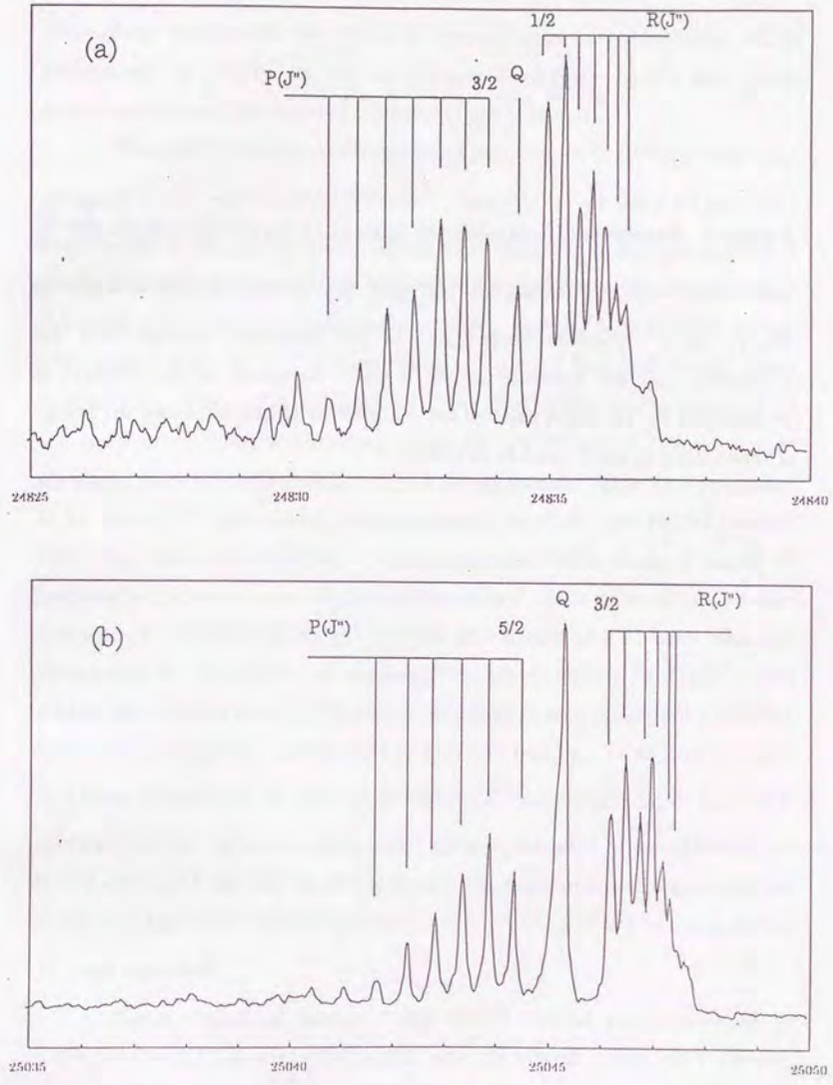

Figure 2

Figure 2. Examples of jet cooled LIF spectra of the HCCS radical. (a) 3_0^1 with (Ω',Ω")=(1/2,1/2) at 24,830 cm^{-1} and (b) 3_0^1 with (Ω',Ω")=(3/2,3/2) at 25,450 cm^{-1}. Absolute frequencies of the excitation energy were not calibrated and are accurate within 5 cm^{-1}. Linearity of the abscissa is within 0.01 %. Note the relative intensity of the Q-branches and the lowest J' transitions in the P- and R- branches.

Vibrational assignment for the $\tilde{A}$-$\tilde{X}$ system were not completed, while assignment of (Ω',Ω") for all the observed vibronic bands are easily determinable from the relative intensity of the Q-branch.

The relatively strong vibronic band observed at 24,660 cm^{-1} had been assigned as 4_1^1 with (Ω',Ω")=(5/2,5/2),[2] which is a hot band of the HCC bending mode. An LIF spectrum of this band observed in a supersonic jet is shown in Fig. 3. The interval of the lowest J transitions of the P branch and R branch was 1.96 cm^{-1}. If this band was that with (Ω',Ω")=(5/2,5/2) as had been assigned so far, this interval would correspond to R(5/2)-P(7/2), which is $7(B''+B')$. The rotational constant of the $\tilde{X}\,^2\Pi_i$ state was determined by the milli-meter wave spectroscopy to be B'' = 0.196 cm^{-1}.[3] From this B'' constant, the rotational constant of the upper vibronic state was evaluated to be B' = 0.098 cm^{-1}, which is unreasonably small for the HCCS radical. Observed rotational structure was inconsistent with such a small B' constant considering errors in the measurement. If the interval of 1.96 cm^{-1} corresponds to R(3/2)-P(7/2), the derived B' constant is 0.21 cm^{-1}, which is reasonable for the observed rotational structure shown in Fig.3. This means the vibronic band at 24,660 cm^{-1} is not that with (Ω',Ω")=(5/2,5/2) but with (Ω', Ω")=(3/2,3/2). Similarly the vibronic band at 24,450 cm^{-1}, which had been assigned to 4_1^1 with (Ω',Ω")=(3/2,3/2), was confirmed to that with (Ω',Ω")=(1/2,1/2). It is consistent with this assignment that the Q branch in the 24,450 cm^{-1} band was relatively weak. The assignment of the pair of the bands at 24,660 cm^{-1} and 24,450 cm^{-1} to the hot band of the bending mode, 4_1^1, was excluded.

Three stretching modes of the HCCS radical are considered to correspond to CH stretch, CC stretch, and CS stretch. The PDN usually makes a vibrational temperature of the products cold except for diatomic molecules. Unless these three vibrational modes have especially low vibrational frequencies in the $\tilde{X}\,^2\Pi_i$ state, it is not plausible that any of hot

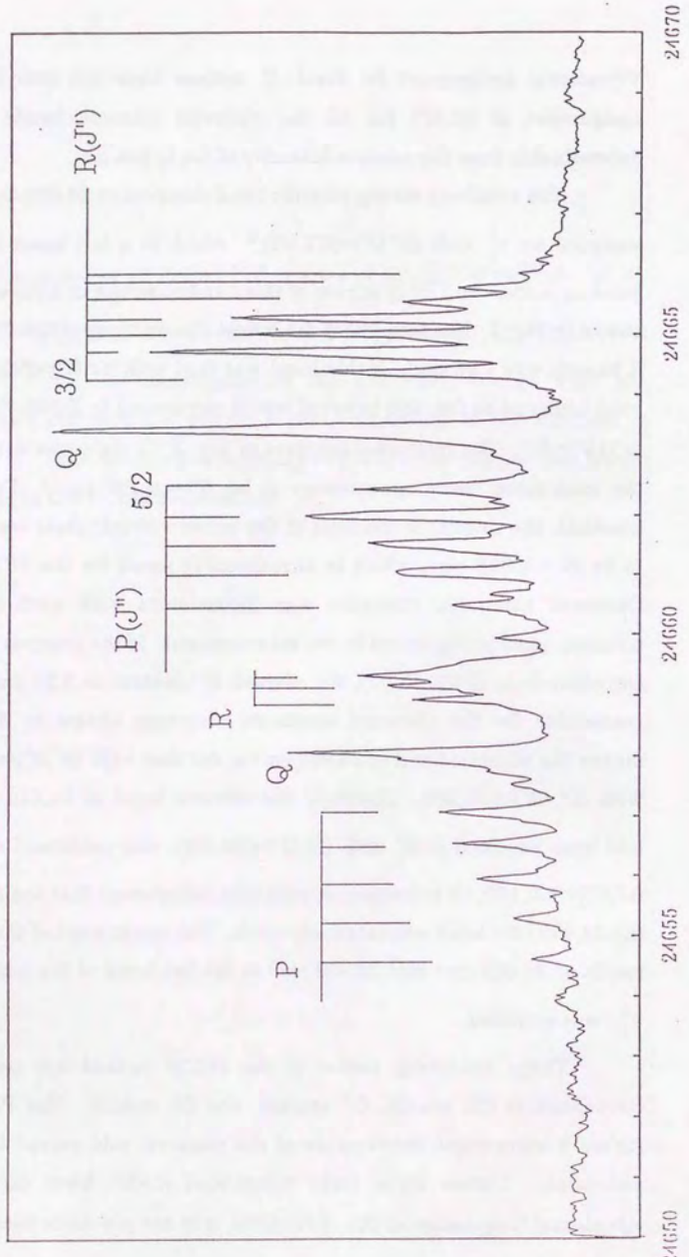

Figure 3

Figure 3. An LIF spectrum of the 24,660 cm^{-1} band. Two vibronic bands are seen within 15 cm^{-1}. The upper band has previously been assigned to 4_1^1 with $(\Omega',\Omega'')=(5/2,5/2)$. Referring to Figure 2, rotational structures of both bands suggest that both of them are bands with $(\Omega',\Omega'')=(3/2,3/2)$.

bands of stretching modes are observed with strong intensity. Since the 24,660 cm^{-1} band was located at no higher than 360 cm^{-1} from the 0_0^0 band, if this band is assigned to a cold band, the HCCS radical has a stretching mode with a low frequency of 360 cm^{-1} in the $\tilde{A}\,^2\Pi_i$. The υ_3 progression was observed up to 3_0^3, where υ_3 mode was corresponded to the CS stretch.[1] Remainder stretching modes are CC and CH stretch. It is not reasonable for these two modes to have as small vibrational frequency as 360 cm^{-1}. Much wider and detailed observation of the $\tilde{A}\,^2\Pi_i$-$\tilde{X}\,^2\Pi_i$ system is necessary to determine vibrational fundamentals of the $\tilde{A}\,^2\Pi_i$ and $\tilde{X}\,^2\Pi_i$ states of the HCCS radical.

Both the $\tilde{A}$ and $\tilde{X}$ states have the symmetry of $^2\Pi_i$, the Ω =3/2 states being located below the Ω =1/2 states. The difference of the band origins of the $(\Omega',\Omega'')=(3/2,3/2)$ and $(\Omega',\Omega'')=(1/2,1/2)$ bands belonging to the same vibronic transition is given by

$$\upsilon((\Omega',\Omega'')=(3/2,3/2)) - \upsilon((\Omega',\Omega'')=(1/2,1/2)) = |Aso(\tilde{X})| - |Aso(\tilde{A})|, \quad (3)$$

where $Aso(\tilde{X})$ and $Aso(\tilde{A})$ are the spin-orbit interaction constant of the $\tilde{X}$ and $\tilde{A}$ states, respectively. $Aso(\tilde{X})$ was reported as -185 cm^{-1} from the pure rotational spectra.[3] In the $\tilde{A}\,^2\Pi_i$-$\tilde{X}\,^2\Pi_i$ electronic transition, the intervals between the $(\Omega',\Omega'')=(3/2,3/2)$ bands and the corresponding $(\Omega',\Omega'')=(1/2,1/2)$ bands were all ~210 cm^{-1}. The relation (3) is inconsistent with the observed intervals of 210 cm^{-1} when $Aso(\tilde{X})$ is -185 cm^{-1}. The spin-orbit interaction constant of 3pπ orbital in a sulfur atom is 380 cm^{-1} and the *Aso* constant in the $\tilde{X}\,^2\Pi_i$ state of the NCS radical, which is isoelectronic to HCCS, is -320 cm^{-1}.[20] From the comparison with the NCS radical, the $Aso(\tilde{X})$ of HCCS may have a higher value than the reported value. Vrtilek *et al.* and Tang[21]

suggested a possibility of rotational perturbation for the levels with Ω =1/2 in the vibronic ground state. Two bending modes of this radical can cause the Renner-Teller effect, which can make the bending excited states ($_\mu\Sigma$, $\Delta_{3/2,5/2}$ states) closer to the Ω=1/2 state of the vibronic ground state. If thus lowered bending excited states perturb the rotational structure of the Ω=1/2 state, the derive $Aso(\tilde{X})$ constant is different from the true interval between the Ω=3/2 and Ω=1/2 states of the vibronic ground state.

4-2. Quantum beats of the fluorescence decay in the $\tilde{A}\,^2\Pi_i$-$\tilde{X}\,^2\Pi_i$ transition of the HCCS radical.

In measurement of the temporal behavior of the fluorescence, quantum beats were observed. Observed quantum beats in different vibronic bands are compared in Fig. 4. Fig. 4(a) is the temporal decay of the P(5/2) rotational line in the 0_0^0 band with $(\Omega',\Omega'')=(3/2,3/2)$ at 24,300 cm^{-1}. Fig. 4(b) and 4(c) were observed in the bands with higher excitation energies by 1,400 cm^{-1} and 2,200 cm^{-1} from the origin band, respectively. Especially in Fig. 4(c), a long tail of radiative decay was observed.

Quantum beat is ascribed to the quantum mechanical interference effect of the superposition state composed of neighboring molecular eigenstates. The superposition state is prepared by coherent excitation of plural eigenstates during a short pulse. The pulse width of the laser was less than 10 nsec and it could prepare a superposition state composed of the molecular eigenstates within 100 MHz at least.

As is well known, temporal behaviors of fluorescence can be classified by the numbers of interfering states within a coherence width of a pulsed excitation. In the following expressions, it is supposed that a zero-order rovibronic state $|s>$ in an electronic excited state is mixed with zero-order interacting states $\{|l>\}$ to produce molecular eigenstates $\{|j>\}$. A

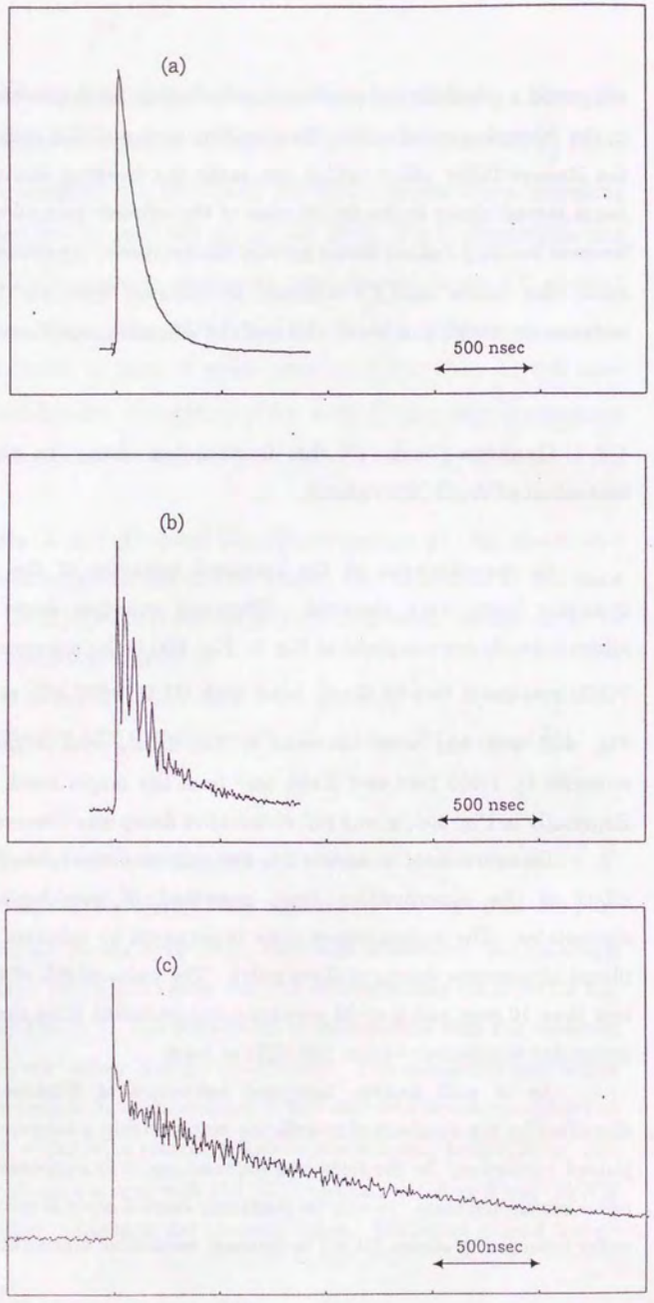

Figure 4

Figure 4. Temporal behaviors of the fluorescence of (a) P(5/2) in the 0_0^0 band with (Ω',Ω'')=(3/2,3/2) at 24,300 cm-1 and (b) P(7/2) in the 25,700 cm-1 band with (Ω',Ω'')=(3/2,3/2) and (c) P(11/2) in the 26,530 cm-1 band tentatively assigned to 3_0^3 with (Ω',Ω'')=(3/2,3/2).

lower rovibronic state $|g>$ (an electronic ground state) is supposed to have nonzero electronic transition probability with $|s>$.

When there is only one eigenstate within the coherence width of a pulsed laser, temporal behavior of fluorescence, $I(t)$, is described as a single exponential decay.

$$I(t) \propto \exp(-\gamma t). \tag{4}$$

In eq. (4) the time constant, $1/\gamma$, is determined by a transition moment between a upper and lower states. This is called as "small molecular limit". If more than two eigenstates are excited coherently, total fluorescence from them are represented as

$$I(t) \propto \sum_{j,j'}^{N} \exp(\frac{-\gamma_j}{\hbar} t) \cos(\omega_j - \omega_{j'}) t \tag{5}$$

where, j indicates the j-th molecular eigenstate with a term energy of $\hbar\omega_j$. N is the number of molecular eigenstates excited coherently by a laser pulse. For $N < \sim 10$, quantum beats could be observed due to oscillating term, $\cos(\omega_j - \omega_{j'})t$, in eq. (5). This stage is called as "sparse intermediate case". For more N, oscillating term in eq. (5) is averaged and apparently two exponential decays with different decay constants are observed. This situation is called as "dense intermediate case".

$$I(t) \propto A\exp(-\alpha t) + B\exp(-\beta t). \tag{6}$$

Suppose that $\alpha >> \beta$. The first short decay in eq. (6), $A\exp(-\alpha t)$, is related to dephasing of the superposition state prepared at $t = 0$. The second slow decay in eq. (6), $B\exp(-\beta t)$, is the average of radiative decays of N molecular eigenstates. Intramolecular relaxation processes such as

intramolecular vibrational energy redistribution (IVR) or internal conversion (IC) cause the dephasing of the superposition state. α is given as,[16]

$$\alpha = 2\pi W^2 \rho, \tag{7}$$

where W is a matrix element of intramolecular processes between zero-order states of $|s>$ and $\{|l>\}$. ρ is a density of molecular eigenstates $\{|j>\}$ at the energy of $|s>$. For example, if $\{|l>\}$ have a different spin multiplicity from that of $|s>$ and ISC mixes $|s>$ with $\{|l>\}$, resultant eigenstates $\{|j>\}$ have diluted transition moment for fluoresce to $|g>$. Suppose W_{ISC} is equal for N $\{|l>\}$ states for simplicity, radiative lifetime is N times as long as that is expected without considering the intramolecular process.

$$\beta = \gamma_s/N, \tag{8}$$

where γ_s is an inverse of Einstein's A coefficient calculated from $<s|\mu|g>$ (electric transition moment) and υ_{sg} (transition frequency of $|s> \rightarrow |g>$). Anomalously longer radiative lifetime than expected is well known as the Douglas effect.[22] Douglas suggested that IC with highly vibrational excite states of the electronic ground state can play the same role as ISC. In the present study, fluorescence were modulated in most of the observed vibronic bands. Although quantum beats were not observed in the 0_0^0 band, they were clearly observed in the vibronic bands with higher excitation energies. Totally different quantum beats were observed for different rotational transitions in a vibronic band. No apparent dependence of the beats on the J numbers were observed. However, the quantum beats of the rotational transitions with common upper J states showed same behaviors. In Fig. 5, temporal decays of P(9/2) and R(5/2) of the unassigned band with

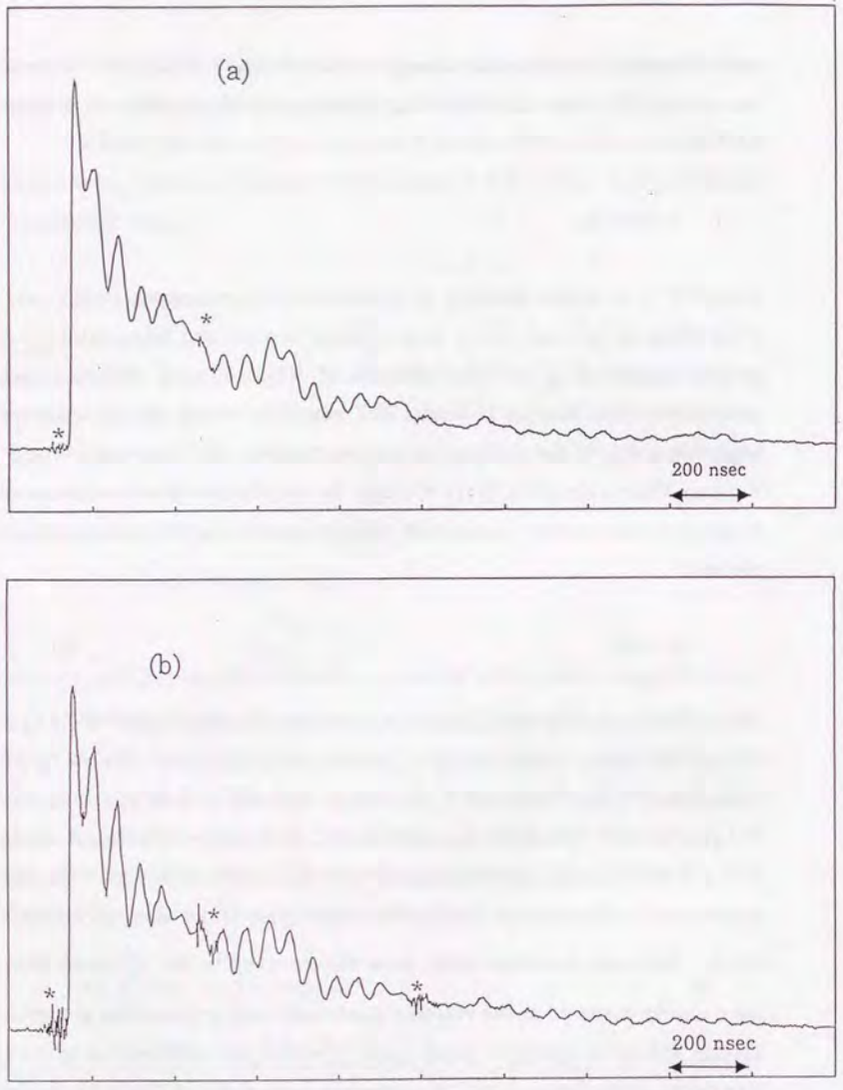

Figure 5. Quantum beats observed (a) P(9/2) and (b) R(5/2) in the band at 25,700 cm^{-1}. Noises at asterisks (*) are due to electronics.

$(\Omega',\Omega'')=(1/2,1/2)$ at 25,700 cm^{-1} are compared. They are transitions involving $J'= 7/2$ as the upper rotational state.

The HCCS radical has a magnetic moment due to its nonzero spin angular momentum and nonzero electronic angular momentum both in the $\tilde{A}\,^2\Pi_i$ and $\tilde{X}\,^2\Pi_i$ states. This means a possibility of the Zeeman quantum beats. Although a magnetic field as strong as 1.8 Gauss, which is 5 times stronger than the terrestrial magnetic field, was applied, the quantum beats were not affected. A polarizer was set in front of the PMT along a parallel or perpendicular direction to the polarization of the excitation laser. The extinction ratio of the polarizing sheet was 10^{-4}. The quantum beats were not changed by the direction of polarization. Since the Zeeman quantum beats depend both on strength of applied magnetic field and on polarization of excitation and detection,[23,24] these observation results exclude that the nature of the observed quantum beat is the Zeeman quantum beat induced by the terrestrial magnetic field.

A rotational level of the HCCS radical in the $\tilde{A}\,^2\Pi_i$ state is split into four levels due to a spin doubling, Λ-type doubling, and proton hyperfine interaction. Their intervals are roughly considered to be 1 ~ several hundred MHz and the coherence width of the laser is wide enough to cover the splitting. However, it is readily understood that the observed quantum beat arises from coherent excitation of not only four eigenstates split from single rotational level because of following observed results. (1) Although changes of the Λ-type doubling or the hyperfine structure with different vibrational states are considered to be a few %, observed quantum beats had apparent dependence on the term energy of the upper vibronic states. Especially, no quantum beats were observed in the 0_0^0 band. (2) More than 6 ($=_4C_2$) components of oscillators were observed in the fluorescence decay. (3) Observed quantum beats did not show such J-dependence as the hyperfine splittings, which are decreased proportional to $1/(J+1)$. (4)

Elongation of a radiative lifetime shown in Fig. 4(c) could not be caused by the coherent excitation of the hyperfine split levels. The Douglas effect is ascribed to such intramolecular process as mix with other non radiative Born-Oppenheimer states.

Elongation of the radiative lifetime suggests a possibility of the intersystem crossing (ISC) in the $\tilde{A}\,^2\Pi_i$ state. In the cases of larger molecules, biexponential decays with a long tail were observed and they were ascribed to S_1-T_1 interaction.[9,11,25] A possible state perturbing HCCS in the $\tilde{A}\,^2\Pi_i$ state by ISC would be a quartet state. From a consideration of the molecular orbitals of HCCS, no quartet electronic state arises from the following configurations which produce the $\tilde{A}\,^2\Pi_i$ and $\tilde{X}\,^2\Pi_i$ states, respectively.

$(1\pi)^4(2\pi)^3$..... $\tilde{X}\,^2\Pi_i$,

$(1\pi)^3(2\pi)^4$..... $\tilde{A}\,^2\Pi_i$.

A plausible electronic configuration to produce the lowest quartet state is,

$(1\pi)^4(2\pi)^2(\sigma^*)$....$^4\Sigma^-$, $^2\Delta$,

or $(1\pi)^4(2\pi)^2(3\pi^*)$....$^2\Phi$, $^4\Pi$, $^2\Pi$.

The orbital energy of the σ^* or $3\pi^*$ therefore the location of the $^4\Sigma^-$ or $^4\Pi$ state have not been known. If this quartet state mixes with the $\tilde{A}$ state by ISC to cause the quantum beats, it is required that the density of states of the quartet state should be at least larger than a few states per 100 MHz (coherence width of the laser) at the energy region of the $\tilde{A}$ state. Density of vibrational states is largely dependent on the vibrational term energy. The energy differences to be compared are (2π)-(1π) and (σ^*)-(2π) or $(3\pi^*)$-(2π). The former corresponds to the $\tilde{A}\,^2\Pi_i$-$\tilde{X}\,^2\Pi_i$ transition energy of 3 eV.

The latter corresponds to the term energy of the $^4\Sigma^-$ or $^4\Pi$ state. Although the $^4\Sigma^-$ state should be the lowest energy term in the electronic configuration of $(1\pi)^3(2\pi)^3(\sigma^*)$ or $(1\pi)^3(2\pi)^3(3\pi^*)$, it is questionable that the $^4\Sigma^-$ state lies at the so low energy region as to have sufficient density of states near the origin of the $\tilde{A}$ state.

The most probable intramolecular process causing the observed quantum beats the internal conversion (IC) between a $\tilde{A}$ vibronic state and highly excited vibrational states of the $\tilde{X}$ state. If molecular eigenstates within the coherence width of the excitation laser pulse are composed of a $\tilde{A}$ vibronic state and highly excited vibrational states of $\tilde{X}$ in the zero-order basis, each of them has a divided transition moment of fluorescence and their averaged radiative lifetime is longer than the expected value without the vibronic mixing. The observed temporal behavior of fluorescence shown in Fig. 4(c) can be well explained by the model of IC. If this is the case, the fast exponential decay in Fig. 4(c) shows the dephasing of the superposition state by IC as is represented in eqs. (6) and (7), while the second slow decay has the radiative lifetime of molecular eigenstates, corresponding to eqs. (6) and (8).

Rough estimation of $\rho(\varepsilon)$, which is the destiny of states of the $\tilde{X}$ state at the term energy of ε, also supports the possibility of IC in the $\tilde{A}$ state. No vibrational parameters of the HCCS radical in the $\tilde{X}$ state are available, alternative values of other molecules was used for an estimation of $\rho(\varepsilon)$. Results of the estimation by a direct counting method are shown in Fig. 6. In Table I, alternative vibrational parameters used in the estimation are listed. ω_i and x_{ii} are used for each mode, therefore, a decoupled Morse potential is assumed for each vibrational mode. Around the $\tilde{A}$ state, $\rho(\varepsilon)$ = one state per 10 MHz at ε = 24,000 cm^{-1} and $\rho(\varepsilon)$ = a few states per 10 MHz at ε = 28,000 cm^{-1}, were calculated. Considering errors in this estimation based on assumed vibrational parameters, these results agrees fairly well

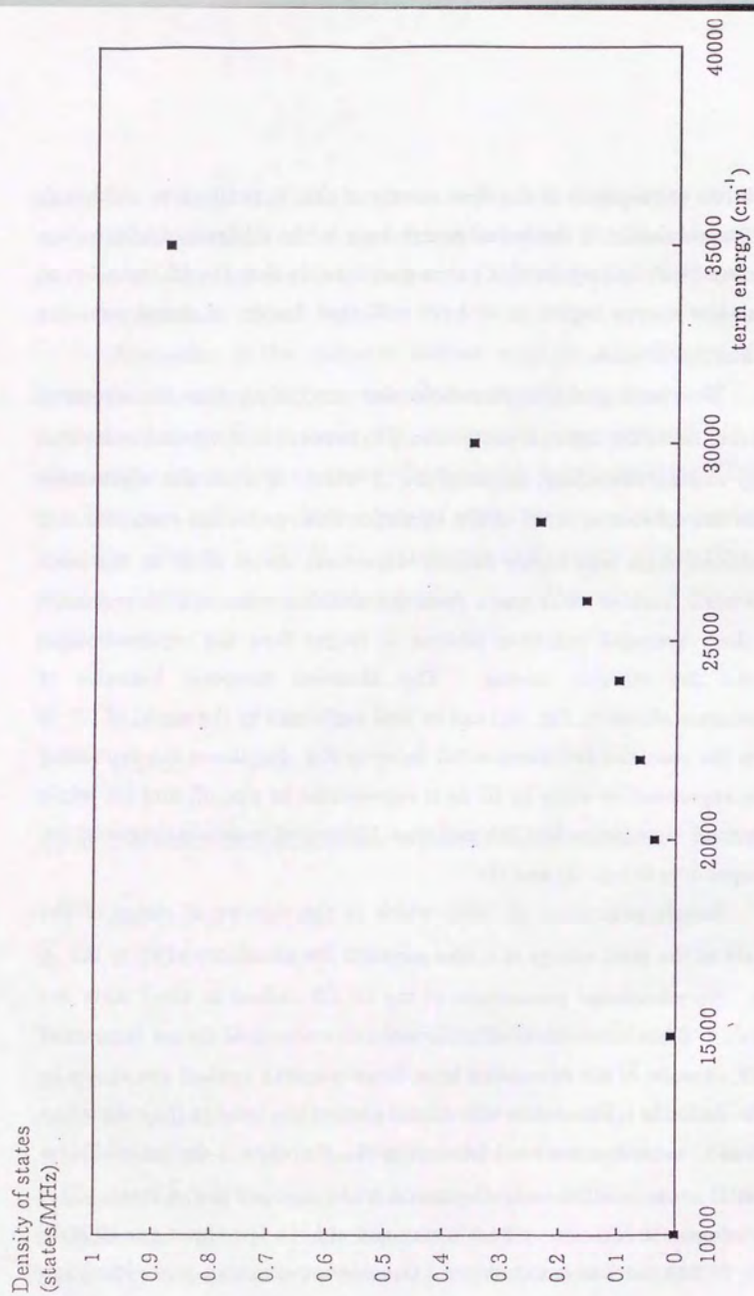

Figure 6

Figure 6. Estimated density of states of HCCS radical in the $\tilde{X}$ state. This is evaluated by a direct counting method based on the vibrational parameters listed in Table I.

with the observation.

Internal conversion is a kind of vibronic interaction with other Born-Oppenheimer states with the same spin multiplicity. The matrix element is related to an adiabatic term, $\partial/\partial Q$, and represented as

$$\langle\varphi(A)(r,Q)|\frac{\partial}{\partial Q_k}|\varphi(X)(r,Q)\rangle\langle\chi_k(A)|\frac{\partial}{\partial Q_k}|\chi_k(X)\rangle\prod_{i\neq k}\langle\chi_i(A)|\chi_i(X)\rangle, \qquad (9)$$

where $\varphi(r,Q)$ and χ_i are an electronic part and a vibrational part for i mode of the Born-Oppenheimer states, respectively. $\chi_i(A)$ is a vibrational state in the $\tilde{A}$ state near the origin band, and $\chi_i(X)$ is a highly vibrational excited state in the $\tilde{X}$ state. The expression (9) shows a dependence of the internal conversion on the vibrational modes (accepting mode (k)/promoting mode (i)). The υ_4 mode (out-of-plane bending) of formaldehyde (H_2CO) is known as the promoting mode of IC in the $\tilde{A}\,^1A_2$ state.[26] Statistical analysis of quantum beats in the $\tilde{A}\,^2\Pi_i$-$\tilde{X}\,^2\Pi_i$ transition of HCCS will give us the rate of IC and $\rho(\varepsilon)$ as functions of ε over 3,000 cm^{-1}, in which quantum beats change drastically. Quantum beats may have information on vibrational assignments in the $\tilde{A}$ state as well as the intramolecular process in the electronic excited state.

5. Conclusion

Jet cooled LIF spectra of the $\tilde{A}\,^2\Pi_i$-$\tilde{X}\,^2\Pi_i$ system of the HCCS radical have been observed by using a pulsed-discharge-nozzle. Assignments of (Ω',Ω'') were easily performed. Previously reported assignment for 24,660 cm^{-1} band was questionable from the observed rotational structure. From the qualitative analysis of observed quantum beats, the $\tilde{A}\,^2\Pi_i$ state is

considered to interact with highly excited vibrational states in the $\tilde{X}\,^2\Pi_i$ state by internal conversion. Estimation of $\rho(\varepsilon)$ supports the internal conversion in the $\tilde{A}\,^2\Pi_i$ state.

Table I Vibrational parameters used in estimation of $\rho(\varepsilon)$ (in cm^{-1}).

vibrational mode		
υ_1 (CH str.)	ω_1 =3311[a]	x_{11} = 60.6[b]
υ_2 (CC str.)	ω_2 =1388[c]	x_{22} = 18.2 [d]
υ_3 (CS str.)	ω_3 =859[e]	x_{33} = 6.2 [f]
υ_4 (HCC bend.)	ω_4 =713[g]	x_{44} = 0.5[h]
υ_5 (CCS bend.)	ω_5 =387[i]	x_{55} = 0.5[h]

[a] υ_{CH} of HCN. [b] Derived from the D(H-CN).

[c] υ_{CC} of H_2CCO. [d] Derived from the D(H_2C-CO).

[e] υ_{CS} of OCS. [f] Derived from D(OC-S).

[g] υ_{HCC} of HCN.

[h] fixed.

[i] υ_{CCS} of NCS.

[a]-[g], [i] G. Herzberg, *Electronic spectra of polyatomic molecules* (Van Nostrand, New York, 1966).

References

[1] S. L. N. G. Krishnamachari and D. A. Ramsay, Faraday Discuss. Chem. Soc. 71, 205 (1981).

[2] B. Coquart, Can. J. Phys. 63, 1362 (1985).

[3] J. M. Vrtilek, C. A. Gottlieb, E. W. Gottlieb, W. Wang, and P. Thaddeus, Astrophys. J. 398, L73 (1992).

[4] Y. Ohshima and Y. Endo, J. Mol. Spectrosco. 153, 627 (1992).

[5] P. M. Felker and A. H. Zewail, J. Chem. Phys. 82, 2961 (1985).

[6] P. M. Felker and A. H. Zewail, J. Chem. Phys. 82, 2975 (1985).

[7] P. M. Felker and A. H. Zewail, J. Chem. Phys. 82, 2994 (1985).

[8] P. M. Felker, W. R. Lambert, and A. H. Zewail, J. Chem. Phys. 82, 3003 (1985).

[9] J. Chaiken, M. Gurnick, and J. D. McDonald, J. Chem. Phys. 74, 106 (1981).

[10] H. Bitto, P. R. Willmott, and J. R. Huber, J. Chem. Phys. 95, 4765 (1991).

[11] J. Kommandeur, W. A. Majewski, W. L. Meerts, and D. W. Pratt, Ann. Rev. Phys. Chem. 38, 433 (1987).

[12] M. Ivanco, J. Hager, W. Sharfin, and S. T. Wallace, J. Chem. Phys. 78, 6531 (1983).

[13] E. Abramson, C. Kittrel. J. L. Kinsey, and R. W. Field, J. Chem. Phys. 76, 2293 (1982).

[14] P. C. Haarhoff, Mol. Phys. 6, 337 (1963).

[15] P. C. Haarhoff, Mol. Phys. 7, 101 (1963).

[16] M. Bixon and J. Jortner, J. Chem. Phys. 50, 4061 (1969).

[17] K. F. Freed and A. Nitzan, J. Chem. Phys. 73, 4765 (1980).

[18] F. Lahmani, A. Tramer, and C. Tric, J. Chem. Phys. 60, 4431 (1974).

[19] H. Kohguchi, Y. Ohshima, and Y. Endo, in preparation.

[20] F. J. Northup and T. J. Sears, J. Chem. Phys. 91, 762 (1989).

[21] Jian Tang, private communication.

[22]A. E. Douglas, J. Chem. Phys. 45, 1007 (1966).
[23]H. Watanabe and S. Tsuchiya, J. Chem. Phys. 82, 5310 (1985).
[24]P. J. Brucat and R. N. Zare, J. Chem. Phys. 78, 100 (1983).
[25]P. U. de Haag and W. L. Meerts, Chem. Phys. 156, 197 (1991).
[26]R. G. Miller and E. K. C. Lee, , J. Chem. Phys. 68, 4448 (1978).

Acknowledgment

I wish to thank Prof. Yasuki Endo for his helpful advice and valuable suggestions. I wish also to express my gratitude to Prof. Yasuhiro Ohshima for his helpful discussions and encouragement throughout the present study. I am grateful also to all members of Prof. Endo's laboratory in the University of Tokyo for their supports throughout the present study.